Quantization Effects on Beamforming in Dense Phased Arrays

by

Cornelis Rossouw Wilke

Thesis presented in partial fulfilment of the requirements for the degree of Master of Engineering (Electronic) in the Faculty of Engineering at Stellenbosch University

Department of Electrical and Electronic Engineering,
University of Stellenbosch,
Private Bag X1, Matieland 7602, South Africa.

Supervisors:

Dr. J. Gilmore Prof. D.B. Davidson

March 2018

Declaration

By submitting this thesis electronically, I declare that the entirety of the work contained therein is my own, original work, that I am the sole author thereof (save to the extent explicitly otherwise stated), that reproduction and publication thereof by Stellenbosch University will not infringe any third party rights and that I have not previously in its entirety or in part submitted it for obtaining any qualification.

Date: March 2018

Abstract

Quantization Effects on Beamforming in Dense Phased Arrays

C.R. Wilke

Department of Electrical and Electronic Engineering,
University of Stellenbosch,
Private Bag X1, Matieland 7602, South Africa.

Thesis: MEng (Electronic)

March 2018

Reflector-based radio telescopes have traditionally been the instrument of choice in Radio Astronomy since around the 1960's. However, in particular for frequencies below around 1 GHz, a new generation of aperture array radio telescopes are being developed internationally.

These aperture arrays consist of phased antenna arrays that are electronically steered by making use of analogue and digital beamforming techniques. The implementation cost of an analogue beamformer is dominated by its complexity of which its phase resolution has a significant contribution. On large-scale systems such as the Square Kilometre Array, it is of substantial interest to investigate the possibility of reducing subsystem cost, which additionally serves as the motivation of this thesis.

Reducing the phase resolution of an analogue beamformer can have an impact on its implementation cost, but also its performance in an array. Important beamforming performance metrics for Radio Astronomy are identified as the main beam pointing accuracy and the side lobe level. A methodology is developed by which these performance metrics can be evaluated as a function of the array parameters and phase resolution of the beamformer.

Initially, the performance is determined using array factor based beamforming on a *forced excitation* model, with phase weights quantised according to a certain phase resolution. The performance is, therefore, determined purely as a function of the array configuration without the effects of mutual coupling. In this way, the impact of phase quantization is directly observed that would otherwise be obscured by the contribution of mutual coupling.

As a conclusion, a demonstrative study is performed on a *free excitation* planar model, which implies that mutual coupling is incorporated. To obtain coupling parameters, a Dense Dipole Array (DDA) prototype tile is built and measured. The performance metrics were then evaluated, although to a lesser extent compared to the forced excitation model, due to limitations in the practical measurements of the DDA. Where applicable, the results were successfully explained from insight obtained in the forced excitation model, which further confirmed the use of the proposed methodology presented in this thesis.

The performance metrics were evaluated by simulation based on array sizes that accommodate the available processing power and, for the free excitation models, the angular resolution in the practical measurements. Therefore, the thesis serves as a demonstration of a proposed methodology. The results, however, did provide valuable insight on quantization effects that will be applicable in larger arrays.

Uittreksel

Kwantiseerings Effekte op Bundelvorming in Digte Gefaseerde Samestellings

C.R. Wilke

Departement Elektriese en Elektroniese Ingenieurswese,
Universiteit van Stellenbosch,
Privaatsak X1, Matieland 7602, Suid Afrika.

Tesis: MIng (Elektronies)

Maart 2018

Vanaf omtrent die 1960's was skottel-gebaseerde radio teleskope normaalweg die instrument van keuse wanneer dit kom by Radio Astronomie. Vandag word daar egter reg oor die wereld 'n nuwe generasie van gefaseerde antenna samestelling radio teleskope ontwikkel.

Hierdie samestellings word elektronies gestuur deur gebruik te maak van digitale en analoog bundelvorming tegnieke. Die implementering koste van 'n analoog bundelvormer word oorheers deur sy kompleksiteit, waarvan sy fase-resolusie 'n groot bydra het. Op groot-skaal sisteme soos die Vierkante-Kilometer Samestelling is dit van belang om die moontlikheid van 'n reduksie in subsisteem koste te ondersoek.

Deur die fase-resolusie van 'n analoog bundelvormer te verlaag kan 'n impak op sy implementering koste gemaak word, maar ook sy optrede. Belangrike optree-aspekte van ' bundelvormer in Radio Astronomie is geïdentifiseer as die hoof lob wys-akkuraatheid en die sy lob vlak. 'n Metode is ontwikkel waarmee die optree-aspekte van 'n samestelling bepaal kan word in terme van sy fisiese eienskappe en die fase-resolusie van die bundelvormer.

Die optrede is aanvanklik bepaal deur gebruik te maak van skikking faktor gebaseerde bundelvorming op 'n *geforseerde-opwekking* model, met fase gewigte gekwantiseer volgens 'n bepaalde fase-resolusie. Die optrede is daarvoor bepaal slegs as 'n funksie van die samestelling se eienskappe, sonder die effekte van wedersydse koppeling. Op hierdie manier word die effekte van fase-kwantifiseering direk vasgestel wat andersins verduister sou wees deur die bydra van wedersydse koppeling.

'n Finale studie is gedoen gebaseer op 'n *vrye-opwekking* model, wat impliseer dat wedersydse koppeling in ag geneem word. Om koppeling parameters te verkry is 'n Digte Dipool Samestelling (DDS) prototipe teël gebou en gemeet. Die optree-aspekte is toe bestudeer, hoewel tot 'n mindere mate in vergelyking met die geforseerde opwekking model, asgevolg van beperkings in die praktiese metings van die DDS. Waar van toepassing, was die resultate verduidelik deur gebruik te maak van die insig wat verkry is in die geforseerde-opwekking model. Dit het ook verder die metodiek wat in hierdie tesis aangebied word bevestig.

Die optree-aspekte is bestudeer deur simulasies te gebruik wat gebaseer is op samestelling groottes wat beide die beskikbare rekenaarkrag en die hoek resolusie van die praktiese metings wat in die geforseerde-opwekking model gbruik is, akkommodeer. Die resultate het wel waardevolle insig in die effekte van fase-kwantiseering voorsien wat van toepassing sal wees op groter samestellings.

Acknowledgements

I would like to express my sincere gratitude to the following people and organisations ...

- My study leader, Dr Jacki Gilmore: for your guidance, invaluable support and providing me with the opportunities that you have.
- My co-supervisor, Prof. David B. Davidson: for your overall guidance and providing my funding.
- David Prinsloo: for your guidance and support during my visit to ASTRON.
- Wessel Croukamp: for your excellent workmanship and guidance during the construction of the Dense Dipole Array.
- Anneke Bester: for your support during the measurement process of the Dense Dipole Array.
- Jan Geralt bij de Vaat: for making my visit to ASTRON possible and providing insight in this project.
- Prof. Stefan Wijnholds: for suggesting the investigation of a one-bit beamformer.
- The technical team at ASTRON for manufacturing the PCB tiles under very short notice.
- Dr Danie Ludick: for providing support at some very crucial times.

Dedications

I dedicate this thesis to my parents, Hannes and Elmari Wilke

Contents

List of Figures

List of Tables

Nomenclature

Constants

c =	299792458 m/s
π =	3.14159265359
e =	2.71828182845

Acronyms

ADC Analogue to Digital Converter
ALMA Atacama Large Millimetre Array
ASKAP Australian Square Kilometre Array Pathfinder
BFC Beamformer Chip
CAD Computer Aided Design
CMBR Cosmic Microwave Background Radiation
DC Direct Current
DDA Dense Dipole Array
EEP Embedded Element Pattern
EMBRACE Electronic Multi Beam Radio Astronomy ConcEpt
EMC Electromagnetic Coupling
FoV Field of View
FFT Fast Fourier Transform
FSL First Side Lobe
HPBW Half-Power Beamwidth
IC Integrated Circuit
LOFAR Low-Frequency Aperture Array
LNA Low-Noise Amplifier
MeerKAT Meer-Karoo Array Telescope
MFAA Mid-Frequency Aperture Array
ORA Octagonal Ring Antenna
PCB Printed Circuit Board
RC Resistor-Capacitor

RFI Radio Frequency Interference
SKA Square Kilometre Array
SLL Side Lobe Level
SQNR Signal to Quantization Noise Ratio
VLA Very Large Array

Chapter 1

Introduction

1.1 Radio Astronomy

The existence of extraterrestrial radio sources has been predicted by many physicists and astronomers dating back to the late 19^{th} century. The first official discovery of radio waves coming from extraterrestrial sources, however, was only discovered in 1932 when Karl Jansky, an employee at Bell Telephone Laboratories, was busy conducting an experiment on transatlantic interference. Soon after he published his findings in a paper titled *Electrical Disturbances Apparently of Extraterrestrial Origin* [4]. He wanted to investigate his findings in further detail, but this would not be the case as he was assigned to other projects. Progress was further hampered by the start of WWII when funding in this field was largely allocated for radar development. Therefore, it wasn't until after the war that significant progress and discoveries were made.

To date, significant discoveries in radio astronomy have been made. The discovery of hydrogen and the subsequent mapping thereof enabled astronomers and scientists to determine that galaxies have spiral structures. The radio detection of hydrogen is attributed to the fact that a hydrogen atom radiates energy at 1420.406 MHz when an electron changes its direction of spin relative to the proton.

The discovery of pulsars by Dame Jocelyn Bell-Burnell in 1967 was another significant breakthrough. A pulsar is a rapidly rotating dense neutron star which can be used as a calibration and synchronisation tool for radio astronomy systems [5]. They can also be used for navigation in spacecraft [6].

Radio astronomy also led to the detection of Cosmic Microwave Background Radiation (CMBR), which is a remnant of the big bang.

Radio signals from cosmic sources are typically very weak and, therefore, very sensitive equipment is required to capture them. One of these pieces of equipment is the antenna. To increase the sensitivity of an antenna, an increase in physical collecting area is required. Additionally, when using reflector type antennas, large diameters are required to resolve low-frequency radio sources.

This gave rise to large reflector radio telescopes such as the 76m Lovell radio telescope at Jodrell Bank and the 100m Green Bank Telescope. Constructing steerable reflector antennas of this size is mechanically challenging and with the demand for higher resolution telescopes, an alternative is required.

Radio interferometry enables the use of multiple smaller antennas to synthesize a single larger antenna. Examples of interferometry systems are the Very Large Array (VLA) [7] and Atacama Large Millimeter Array (ALMA) [8], each consisting of multiple steerable dish antennas. A two-element interferometer with element spacing D, also called the baseline, effectively synthesizes the angular resolution of a single dish antenna with diameter D[9].

At low frequencies, an array of fixed omni direction antennas can be used to act as a radio telescope. Beam steering is achieved with specialised hardware and software in a process termed beamforming. The Low-Frequency Array (LOFAR) is an example of such a system [10].

1.2 The Square Kilometre Array (SKA)

In the mid-1990's it was realized by radio astronomers that the radio telescopes of the future would require a one to two orders of magnitude increase in sensitivity to existing telescopes of the time. From this realization, the concept of a square-kilometre collecting area was conceived and, therefore, called the Square Kilometre Array [11; 12].

The current frequency specifications state that an operational band of between 50 MHz and 25 GHz will be required for the science cases involved. Additionally, the field of view (FoV) for frequencies roughly between 0.3 and 1 GHz should have at least two orders of magnitude increase compared to existing telescopes [13]. The reason for this can be explained by the science cases allocated to this frequency band, and that they require simultaneous observations of different parts of the sky. The multi-beam capabilities provided by aperture arrays could solve this problem as will be discussed in the next Section.

The construction of the SKA is divided into two phases where precursors are already being developed for each phase. Phase one will consist of high-frequency reflector antenna arrays and a low-frequency antenna array, located in South Africa and Australia respectively. The Meer-Karoo Array Telescope (MeerKAT) pathfinder consisting of 64 Offset Gregorian antennas, fitted with wide-band Single Pixel Feeds, will be constructed in the Karoo region in South Africa [14]. The Australian SKA Pathfinder (ASKAP) consisting of 36 reflector antennas, will be built in the Murchinson region of Australia and will eventually consist of 96 Focal Plane Array reflector antennas [15]. The low-frequency sparse aperture array, also planned for the same region, will consist of 250 arrays with 180 m diameters. It will operate between 70 - 450 MHz

[14]. Phase two of the SKA will consist of the Mid-Frequency Aperture Array (MFAA) and an extension of the existing reflector antenna arrays [12].

1.3 Mid-Frequency Aperture Array (MFAA)

The MFAA is specified to have an operational frequency band of roughly 0.4 - 1.4 GHz. To explain this selected frequency band, it is necessary to investigate an important figure of merit for the SKA, which is survey speed, expressed as[16]:

$$\text{Survey Speed} = (\text{Sensitivity})^2\text{FoV}, \tag{1.1}$$

where sensitivity is defined as a function of system noise temperature (T_{sys}) and effective area A_{eff} as :

$$\text{Sensitivity} = \frac{A_{\text{eff}}}{T_{\text{sys}}}. \tag{1.2}$$

An increase in sensitivity and FoV will optimise the survey speed, but according to Equation 1.2 would require that T_{sys} be minimized while increasing A_{eff} which are both a function of frequency. This leads to different design concepts for each frequency band of the SKA [16].

For frequencies below around 400 MHz, T_{sys} is dominated by sky noise which leads to sparse arrays being the preferred technology choice. When considering frequencies above around 400 MHz, the receiver noise becomes a dominant contributor to T_{sys}. It is explained in [17] that when the element spacing across a frequency band is an order of $\lambda_{\text{min}}/2$, then no increase in effective aperture area is observed at lower frequencies. This implies that a near constant sensitivity can be retained by optimising the receiver noise temperature, which leads to dense aperture arrays being the technology of choice.

This gives rise to a number of dense aperture array topologies that are being investigated for the mid-frequency component (450 - 1450 MHz). These are the Vivaldi array [18], Octagonal Ring Antenna (ORA) [19] and recently, the Dense Dipole Array (DDA)[20]. The EMBRACE system is a SKA precursor in which a Vivaldi array is implemented.

An array is beam-steered by employing special algorithms that can be done multiple times to create multiple beams, effectively "filling" the sky with beams. The FoV is, therefore, only limited by the available processing power which dictates the number of beams that can be formed. The FoV of a single beam (FoV_{b}) is defined in terms of the half-power beamwidth (HPBW) as [17]:

$$FoV_{\text{b}} = \frac{\pi}{4}\left(\text{HPBW}\right)^2. \tag{1.3}$$

The total FoV of an aperture array can then be expressed as:

$$FoV = N_{\mathrm{b}} FoV_{\mathrm{b}}, \tag{1.4}$$

where N_{b} indicates the number of beams.

Multiple scientific experiments can be conducted by using multiple beams, which enables the observation of the science cases involved in this frequency band. These are given by [16] as:

- The Transient Radio Sky - Fast Radio Bursts
- Hydrogen Intensity Mapping - Dark Energy
- Pulsars
- Search for Extraterrestrial Intelligence

When completed, the MFAA will consist of 1024 array stations, each with around 30 000 dual polarized elements [21]. Considering these figures, it is evident that a significant amount of processing power and back-end electronics will be required. Finding ways of reducing the processing power and electronic demands is of great interest. This will also serve as the motivation for the work that will be presented in this thesis.

1.4 Overview

The main aim of this project was to establish evaluation models with which the beamforming performance of low phase resolution beamformers can be determined.

A theoretical framework is established in Chapter 2 to define the expressions that will be used throughout the thesis. This is accompanied by a literature study to provide background on the concepts and components that are under investigation. Chapter 2 ends with a case-study that will provide insight and motivation for analysing low-phase resolution beamformers.

To efficiently determine the effects of phase quantization in beamforming, important beamforming performance metrics for Radio Astronomy were identified and established. They were then evaluated as a function of two array parameters - the inter-element spacing as a function of wavelength and the phase resolution available to the beamformer. In this way, the performance metrics are evaluated in a wide-band manner, as a function of the array configuration and phase resolution of the beamformer. This makes it particularly relevant when considering radio astronomy phased antenna array systems.

The evaluation models are initially based on an array of isotropic elements without mutual coupling and are, therefore, a *forced excitation* model. The array factor expression is used to calculate beam patterns so that the beamforming performance of the array is determined purely as a function of the

array configuration and phase resolution of the beamformer. It is done in this way to directly determine the effects of phase quantization on the beam pattern, that might otherwise be obscured by the effects of mutual coupling. The total beamforming performance of an array is, however, a function of mutual coupling and is an important aspect to consider. In summary, the total performance is determined by:

- The array factor based beamforming performance as a function of the array configuration and phase resolution of the beamformer
- The scan limitations as set out by the embedded element pattern which is representative of the mutual coupling effects in the array [22].

Chapter 3 aims to establish the effects of phase quantization on the beam pattern of an array without the effects of mutual coupling, using the forced excitation simulation model described above.

Mutual coupling is accounted for in Chapter 4 using the *pattern multiplication theorem* which states that the total radiation pattern of an array is the product of the array factor and the average active element pattern. This is done using *free exciation* based simulation models.

The thesis ends with a conclusion on the findings of the project. Recommendations and future work are additionally discussed.

Chapter 2

Theoretical Framework and Literature Study

2.1 Introduction

This Chapter provides and discusses the theory and concepts that will be used throughout this thesis. Classical array theory will be introduced in Section 2.4, and the basic expressions for a linear, and planar array that will be used throughout the thesis will be established.

The basic components of an aperture array radio telescope will be discussed to provide insight on the basic signal chain and at which point beamforming is applied in both hardware and software. This will be followed by a general discussion of the array configurations that are considered for the MFAA.

The Chapter will conclude with a cost case study with the purpose of motivating the investigation into the use of low-phase resolution beamformers in aperture array radio telescopes.

2.2 Aperture Arrays for Radio Astronomy

As discussed in [23], the application of antenna arrays has a very wide variety stretching across radar, telecommunications and recently, radio astronomy. They have the ability to form shaped beams with low side lobes, have good power efficiency and provide a significant gain in a process called beamforming. Additionally, and understandably the most significant feature is its beam scanning ability, referred to as beam steering. Depending on the placement of the individual antenna elements, steering can be done in almost any spherical direction where the full scan range is governed by the radiation pattern of an element embedded in the array.

A large field of view can be achieved by making use of its multi-beam capability, where the number of beams is limited by the receiver chains in the system. Beam steering will be discussed in more detail in Section 2.4.

While arrays provide many advantages, it also comes with certain design challenges. When antennas are spaced in close proximity, mutual coupling is introduced which can either reduce the performance of the array or in some cases, can actually improve some performance aspects array. The Dense Dipole Array that will be used as a reference antenna array in later sections is a good example of this [20]. A more detailed discussion of mutual coupling is provided in Section 2.4.

Depending on the application, arrays can be linear planar or conformal [24]. In radio astronomy, aperture arrays usually are planar structures and a focus will, therefore, be placed on planar arrays. Furthermore, all reasoning will be based on the advantages and challenges that arrays provide in radio astronomy. Some of these have already been discussed, however, a summary is provided by the list below.

2.2.1 Advantages

- Large planar structures which are mechanically simple and easy to mass-produce.
- Has electronic beam steering capability which is much faster compared to mechanical steering of reflectors antennas.
- Large field of view capabilities and, therefore, a subsequent increased survey speed (Equation 1.1).
- With Equation 1.2 in mind, the sensitivity can systematically be increased by upgrading the aperture size and system noise temperature at a later stage. A reflector antenna has a fixed aperture size and will require a whole new reflector for an increase in aperture size.

2.2.2 Disadvantages

- Complicated and expensive electronic design.
- Have narrower bandwidth capabilities than reflector antennas.

Aperture arrays as applied in radio astronomy consist of a significant number of back-end systems that make it a complete system. When a faint cosmic signal arrives at the aperture, it needs to be amplified before any further processing can be done. This is achieved with a Low Noise Amplifier (LNA). The amplified signal is then passed to an analogue beamformer, or beamforming chip (BFC), that filters the signal coming from a predefined direction. This process will be discussed in Section 2.4. Analogue to digital conversion (ADC) is then performed and the digital signal is sent to a computing platform that performs frequency filtering and further beamforming. Finally, the signal is

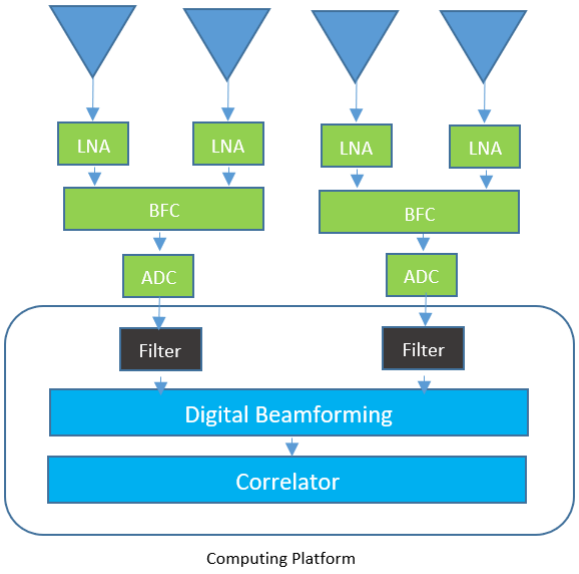

Figure 2.1: Radio telescope aperture array components

sent to a correlator after which the data is distributed to different science platforms. A block diagram of this process is shown in Figure 2.1.

Planar and linear arrays will be investigated in this thesis. An example of the coordinate system and layout that will be used for planar and linear arrays are shown Figures 2.2 and 2.3. As seen, the linear array is simply a sub-array of the planar array.

2.3 Array Configurations: Dense and Sparse

Antenna arrays as stated earlier can take on different configurations, each with their own advantages and disadvantages. The spacing between the elements are classified either as sparse or dense where, dense implies that the antennas are spaced at less than $\lambda/2$, and sparse implies more than $\lambda/2$. It is therefore also clear that the element spacing of a wide-band system can vary between sparse and dense depending on the operating frequency, however, most systems are designed to be consistently dense or sparse across its bandwidth [17].

Sparse arrays have the obvious advantage of requiring fewer elements to fill the same effective aperture as that of a dense array. This significantly reduces the cost of an antenna system as the cost is dominated by the receiver chains [17], which is of great interest when considering the scale of systems such as the SKA. However, this is not the only factor considered when selecting a topology for a radio telescope.

This thesis focuses on antennas for radio astronomy and therefore the SKA will be used as an example to clarify the major differences and trade-offs. As

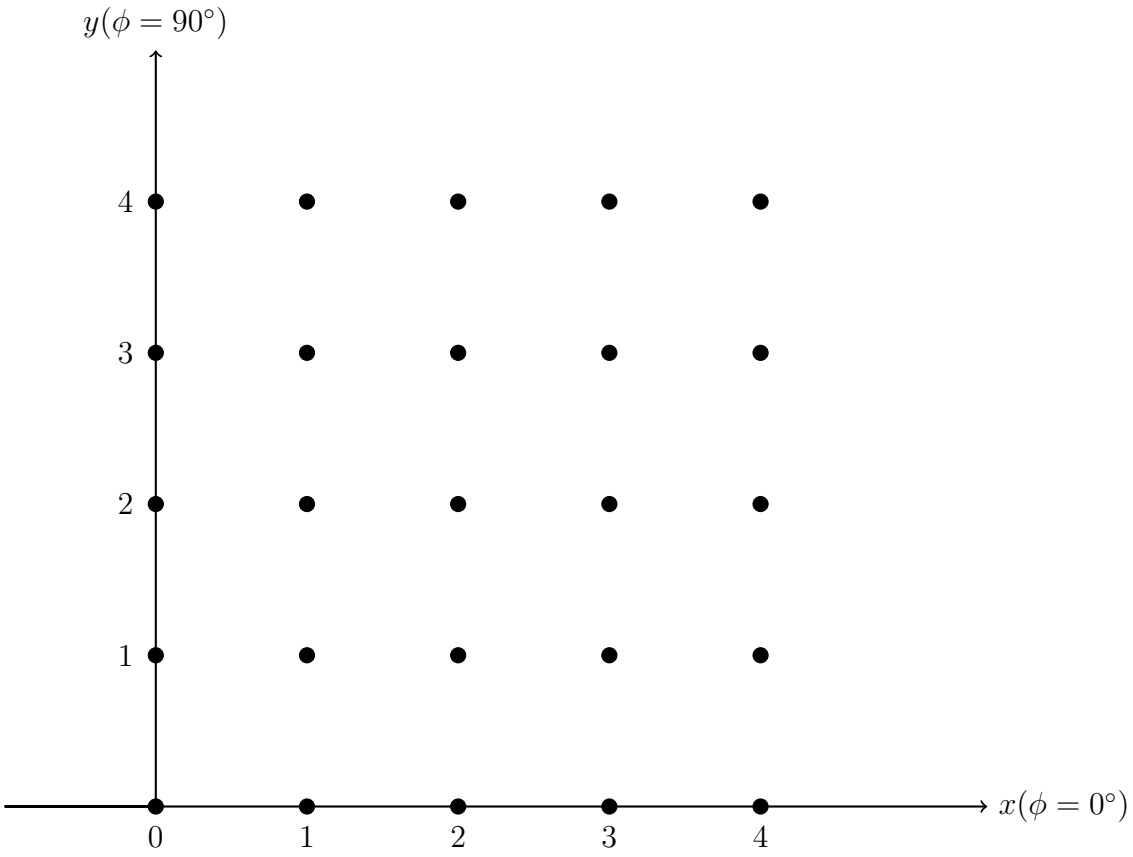

Figure 2.2: Planar array reference layout

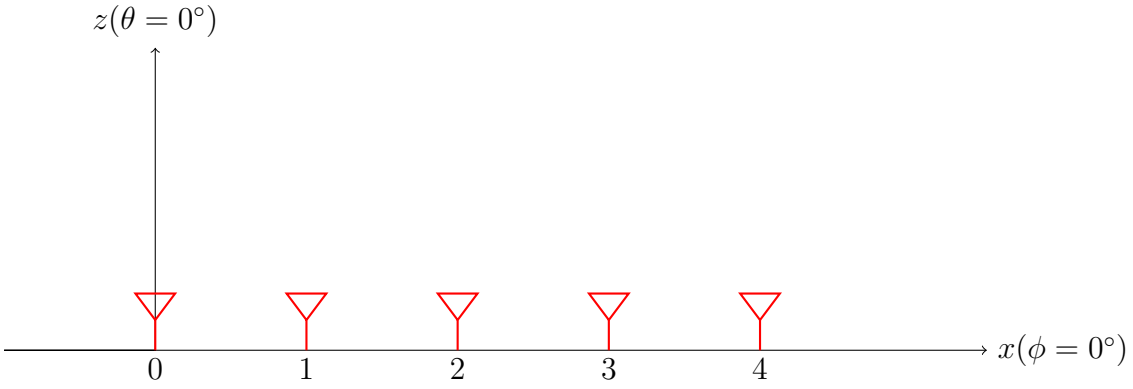

Figure 2.3: Linear array reference layout

described in Chapter 1, the SKA consists three different frequency components, each with their own antenna technology under consideration. It was discussed that aperture arrays are the technology of choice for the two lower frequency components of the SKA, however, it is currently not clear whether it will be sparse or dense. This Section serves as a discussion of each topology and the design challenges of each

The effective area of array changes with topology, with dense and sparse effective area expressed by [17] as:

$$A_{\text{eff,sparse}} = N\frac{\lambda^2}{2}, \tag{2.1}$$

$$A_{\text{eff,dense}} = A_{\text{phys}} = N\frac{\lambda_{\text{min}}^2}{4}, \tag{2.2}$$

where N is the number of elements in the array. From this, it is clear that the effective area of a sparse system is a function of the whole operational frequency band, whereas, for a dense system, it is limited to the shortest in-band wavelength. If N is fixed and a frequency range of 1.3:3 is considered, then the sparse array will provide 20 times the effective area at the lowest operating frequency when compared to a dense array [17].

Sensitivity is the crux of the SKA as described in Chapter 1 and is, therefore, a crucial parameter to consider as well. The sensitivity of each system can be expressed using the effective area as defined above, together with Equation 1.2:

$$S_{\text{sparse}} = \frac{N\lambda^2}{2T_{\text{sys}}}, \tag{2.3}$$

$$S_{\text{dense}} = \frac{N\lambda_{\text{min}}^2}{4T_{\text{sys}}}, \tag{2.4}$$

A dense system consists of more elements to fill the same aperture as a sparse array and therefore it requires more receiver chains. Beamforming is usually employed to reduce the number of digital inputs, but for now, it is assumed that each antenna has its own receiver chain. Furthermore, the expression for T_{sys} is:

$$T_{\text{sys}} = T_{\text{r}} + T_{\text{sky}}, \tag{2.5}$$

where T_{r} is the receiver noise temperature and T_{sky} is the sky noise temperature. It was discussed in Chapter 1 that at frequencies below around 400 MHz, T_{sys} is dominated by T_{sky}. Therefore, it would make sense to use sparse arrays instead of dense arrays, as it was shown that a sparse array would have a more effective area at the low end of a common frequency band. Furthermore, it was discussed that at frequencies above around 400 MHz, T_{sys} is dominated by T_{r}. Again, for a common frequency band the effective area of a dense array

is fixed to its physical aperture and as such it makes sense to use dense arrays for the higher frequencies because it will provide the largest A_{eff}.

The most significant problem with sparse arrays is the fact that there will always be a grating lobe within the visible region as discussed in Section 2.4. This causes the array to receive power from unintended directions, causing directional ambiguity. There are a number of ways to mitigate this occurrence - by placing and rotating the antennas in a specific way, it is possible to suppress the side lobes and grating lobes [25]. In the sparse regular case, however, strong, regular grating lobes are present. By knowing the directional properties of each of these, it is possible to appropriately process these lobes during an observation[25]. Although requiring extra processing, sparse regular systems do hold some advantages over a sparse random system.

Deploying a sparse system, be it in an irregular or semi-random layout, complicates the construction and increases the processing power requirements. Furthermore, Each antenna needs to be back-rotated to preserve its polarization direction. LOFAR is an example of a system in which this method is employed [10].

Dense antenna arrays provide more direct control over its beam pattern [25]. It is shown in Section 2.4 that grating lobes will not form in the visible region and can, therefore, be deployed in a grid-like manner. This lowers the implementation and processing cost in comparison to a sparse array. However, it was also explained that to fill the same aperture at a specific frequency in a dense manner, will require more antennas and, therefore, receiver chains, compared to a sparse implementation.

In summary, when considering an antenna system that is required to operate over a significant frequency band, it is necessary to consider the advantages and disadvantages of each topology as was discussed in this Section. However, if there is freedom available to select a topology for each narrow-band in a certain bandwidth, then it is relatively clear which antenna topology to use for each band.

2.4 Array Theory

2.4.1 The Array Factor

It was explained that the total radiation pattern of an array is dependent on the array geometry and type of element used. It is because of this that the total radiation pattern can be expressed as a product of two factors, one being the radiation pattern of an element in the array, and the other taking into account the geometry and excitation of the array. The latter is called the array factor (AF) and is defined for a regular linear array with N elements as [26]:

$$AF_{\text{linear}} = \sum_{n=0}^{N-1} A_{\text{n}} e^{jn(\psi-\beta)}, \tag{2.6}$$

where A_{n} is the amplitude excitation coefficient of element n, and β is the excitation phase which for a broadside array is defined as:

$$\beta = kd \sin\theta_0, \tag{2.7}$$

where k is the wavenumber, defined as $2\pi/\lambda$, and d is the inter-element spacing. The angle θ_0 is defined as the desired scan direction and is defined off-broadside. The β term indicates the phase shift between adjacent elements. By controlling β it is possible to control the direction in which the AF will form a maximum, leading to a concept called beam steering, which will be discussed in the next Section.

The array factor of a N×M planar array is simply a dimensional extension to the linear AF [26]:

$$AF_{\text{planar}} = \sum_{n=0}^{N-1} \sum_{m=0}^{M-1} A_{mn} e^{j(\psi-\beta)}, \tag{2.8}$$

where ψ for a planar array is defined as:

$$\psi = kd\left(m \sin\theta \cos\phi + n \sin\theta \sin\phi\right), \tag{2.9}$$

and β is defined as:

$$\psi = kd\left(m \sin\theta_0 \cos\phi_0 + n \sin\theta_0 \sin\phi_0\right). \tag{2.10}$$

2.4.2 Beam Steering

The main beam of an array is steered by controlling or delaying the signals of each element by the correct amount so that when the signals are combined, they add coherently for a certain arrival direction. In the frequency domain, this is the equivalent of adding a phase shift to each element.

The first step in deriving the required time delay, or phase shift, is to define the spatial relationship between the arrival direction of interest, and the array itself. Most phased antenna arrays used in radio astronomy only have variation in width and length and are therefore called planar arrays. The element positions for a regular N×M array with element separation d in the x and y directions, are expressed in vector notation as

$$\mathbf{p}_{\text{mn}} = md\hat{\mathbf{x}} + nd\hat{\mathbf{y}}, \tag{2.11}$$

where m and n are the element indices.

The source of the incoming signal is assumed to be far away implying that the wavefront of the signal can be approximated to be planar [26]. The incoming radial direction of the wave is defined in rectangular coordinates by vector $\mathbf{r}_{\text{src}}$ as:

$$\mathbf{r}_{\text{src}} = \begin{bmatrix} \sin\theta_0 \cos\phi_0 \hat{\mathbf{x}} \\ \sin\theta_0 \sin\phi_0 \hat{\mathbf{y}} \\ \cos\theta_0 \hat{\mathbf{z}} \end{bmatrix}. \tag{2.12}$$

A signal incident from (θ_0, ϕ_0), will arrive at each element at different time instances which can further be expressed as a function of a time delay (τ_{nm}), defined as:

$$\tau_{\text{nm}} = \frac{\mathbf{p}_n \cdot \mathbf{r}_{src}}{c} = \frac{1}{c}\left(md\sin\theta_0\cos\phi_0 + nd\sin\theta_0\sin\phi_0\right). \tag{2.13}$$

In the frequency domain, this corresponds to a relative phase shift (β) defined as:

$$\beta = k\mathbf{p}_n \cdot \mathbf{r}_{src} = k\left(md\sin\theta_0\cos\phi_0 + nd\sin\theta_0\sin\phi_0\right), \tag{2.14}$$

where k is the spatial frequency of the signal, also called the wave number and is expressed as $2\pi/\lambda$.

By applying β progressively to each element in the array, it will coherently combine any signal arriving along (θ_0, ϕ_0). The β term can therefore be seen as a phase weight that is used to steer the main beam of the array and can be expressed as part of a separate weighting term (w_{mn}), in the AF as:

$$AF_{\text{planar}} = \sum_{n=0}^{N-1}\sum_{m=0}^{M-1} w_{\text{mn}} e^{j\psi}, \tag{2.15}$$

where w_{mn} is defined as:

$$w_{mn} = A_{\text{mn}} e^{-j\beta}. \tag{2.16}$$

For a linear array, Equation 2.15 reduces to:

$$AF_{\text{linear}} = \sum_{n=0}^{N-1} w_n e^{jn\psi}, \tag{2.17}$$

where w_n is defined as:

$$w_n = A_{\text{n}} e^{-j\beta}. \tag{2.18}$$

To illustrate, an array factor pattern of a linear array steered to $\theta = 20°$ is shown in Figure 2.4.

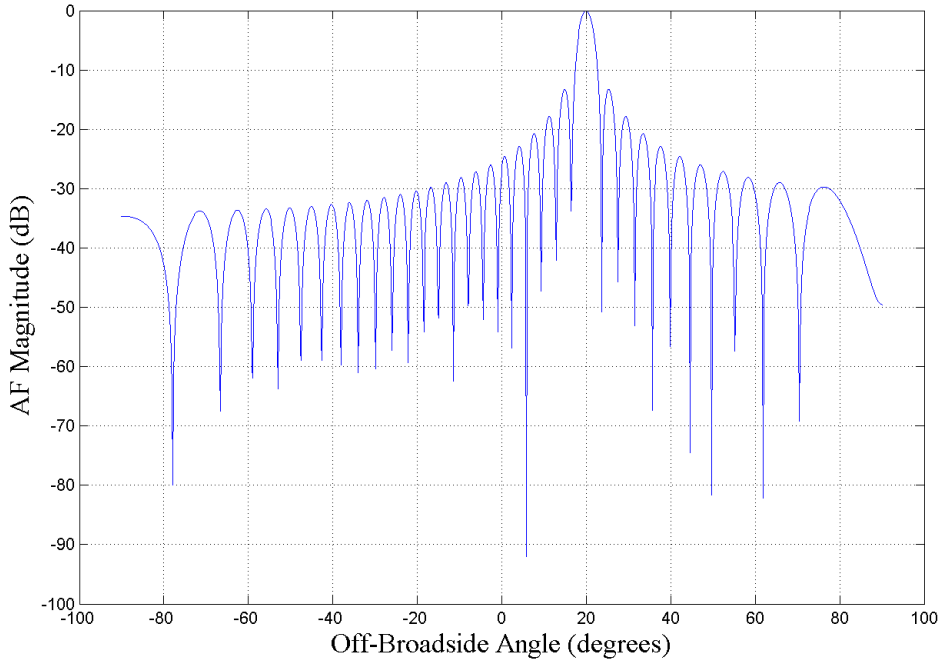

Figure 2.4: Normalized AF plot of an array steered to $\theta = 20°$

2.4.3 Grating Lobes

Th beam pattern is periodic and the AF will form maxima when:

$$\psi + \beta = \pm 2p\pi, p = 0, \pm 1, \pm 2 \ldots, \tag{2.19}$$

where $p = 0$ signifies the position of the main lobe and values of $p \neq 0$ are associated with grating lobes which are additional main lobes forming in the visible region [27].

The visible region is defined as the angular space in which the array can coherently combine signals. Outside the visible region, signals decay at an exponential rate, and as a result very little power is received.

To explain the extents of the visible region, the linear AF is rewritten in terms of k_x space as:

$$AF_{\text{linear}} = \sum_{n=0}^{N-1} w_{\text{n}} e^{jnk_x d}, \tag{2.20}$$

where $k_x = k \sin\theta$. The region where k_x space corresponds to real values of θ is defined where $|k_x| \leq k$. Furthermore, the alias-free region defined as $|k_x| \leq \pi/d$, is the region in k_x space where the main beam direction can be uniquely defined. If $d < \pi/k$ then the alias-free region extends beyond the visible region and it is, therefore, possible to steer the main beam to imaginary

space. Alternatively, if $d > \pi/k$ then the alias-free region is only a section of the visible region and, therefore, it is possible to have a grating lobe in the visible region.

With this observation made, it is possible to restrict the element spacing to values that limit the alias-free region to the extents of the visible region, and further. This is done by recalling Equation 2.19 for $p = 1$, which signifies the first grating lobe:

$$kd\left(\sin\theta - \sin\theta_0\right) = 2\pi, \tag{2.21}$$

and restricting to real space as:

$$d < \frac{\lambda}{1 + |\sin\theta_0|}. \tag{2.22}$$

With scan angles restricted to the visible region, a grating lobe will form in the visible region when $d > \lambda/2$. Therefore, for a broadside linear array, the visible region is defined for $-90° < \theta < 90°$ and d must be smaller than $\lambda/2$ to avoid grating lobes for the full scan range in the visible region.

2.4.4 Beam Properties of an Array

In this subsection the beam properties of a uniformly excited regular broadside array will be discussed. The theory discussed is adapted from [26].

The far field radiation pattern of an array is dependent on angular direction and is expressed as the radiation intensity $U(\theta, \phi)$ by:

$$U(\theta, \phi) = \frac{1}{2\eta}\left[|E_\theta(\theta, \phi)|^2 + |E_\phi(\theta, \phi)|^2\right], \tag{2.23}$$

where E_θ and E_ϕ represents the far-field electric components and η is the intrinsic impedance of the medium. The radiated power P_{rad} can be calculated by integrating the radiation intensity over a 4π solid angle as:

$$\int_0^{2\pi}\int_0^{\pi} U(\theta, \phi)\sin\theta d\theta d\phi. \tag{2.24}$$

The directive properties, or directivity $(D(\theta, \phi))$ of an array can be calculated as:

$$D(\theta, \phi) = \frac{4\pi U(\theta, \phi)}{P_{\text{rad}}}. \tag{2.25}$$

The gain of an array $G(\theta, \phi)$ is a measure of amount of input power that is actually radiated:

$$G(\theta, \phi) = e_a D(\theta, \phi), \tag{2.26}$$

where e_a is the an efficiency factor defined as:

$$e_a = \frac{P_{\text{rad}}}{P_{\text{in}}}. \tag{2.27}$$

2.4.5 Mutual Coupling and Radiation Pattern Effects

This subsection serves as a discussion on the effects of mutual coupling in arrays and is based on derivations done in [22].

When antennas are spaced close together they interact by inducing currents on each other as a result of electromotive force (emf). This can be explained by the laws of Ampére and Faraday. When a time-varying current flows on an antenna, it induces a time-varying magnetic field as explained by Ampére's law which is defined in differential form as:

$$\nabla \times H = J, \tag{2.28}$$

where H is the magnetic field induced by current density J. The magnetic field then induces a time-varying current on another element in close proximity as a result of emf (ϵ) described by Faraday's law as:

$$\epsilon = -\frac{d\Phi}{dt}, \tag{2.29}$$

where Φ is magnetic flux. This also shows that no mutual coupling will be observed when a DC current is applied to the antenna.

This process is then repeated from the second element to the first element, inducing a time-varying current on the first antenna, which effectively changes its impedance.

In an array, the impact of feed network coupling can be excluded by assuming that all the ports in the network are impedance matched. The equivalent circuit for this assumption is shown in Figure 2.5, where each element can be modelled with a source voltage V_n^s, having impedance Z_n^s. The effects of mutual coupling are then included in i_n and v_n.

To demonstrate the impedance effects of mutual coupling, consider two dipoles in close proximity, denoted antenna 1 and antenna 2. The terminal voltage at antenna 1 in an isolated environment would be:

$$V_1 = Z_{11} I_1, \tag{2.30}$$

however, due to antenna 2 being in close proximity to antenna 1, currents are induced by the radiation of antenna 1. In turn, the induced current on antenna 2 re-radiates and induces current on antenna 1, changing the terminal voltage as follows:

$$V_1 = Z_{11} I_1 + Z_{12} I_2. \tag{2.31}$$

The same holds for the terminals of antenna 2, due to reciprocity:

$$V_2 = Z_{22}I_2 + Z_{21}I_1. \tag{2.32}$$

This formulation can be extended to an array of N antennas by treating the array as an N-port network in matrix form as:

$$\begin{bmatrix} V_1 \\ V_2 \\ \vdots \\ V_N \end{bmatrix} = \begin{bmatrix} Z_{11} & Z_{12} & \dots & Z_{1N} \\ Z_{21} & Z_{22} & \dots & Z_{2N} \\ \vdots & \vdots & \dots & \vdots \\ Z_{N1} & Z_{N2} & \dots & Z_{NN} \end{bmatrix} \begin{bmatrix} I_1 \\ I_2 \\ \vdots \\ I_N \end{bmatrix},$$

which, when multiplied out, yields the following:

$$\begin{aligned} V_1 &= Z_{11}I_1 + Z_{12}I_2 + \cdots + Z_{1N}I_N \\ V_2 &= Z_{21}I_1 + Z_{22}I_2 + \cdots + Z_{2N}I_N \\ &\vdots \\ V_N &= Z_{N1}I_1 + Z_{N2}I_2 + \cdots + Z_{NN}I_N. \end{aligned} \tag{2.33}$$

From this, the input impedance of an antenna element n in the presence of other antenna elements can be expressed as:

$$Z_n = \frac{V_n}{I_n} = Z_{n1}\frac{I_1}{I_n} + Z_{n2}\frac{I_2}{I_n} + \cdots + Z_{nM}\frac{I_M}{I_n}. \tag{2.34}$$

However, this is a general formulation and does not take into account the excitation state of unused antenna elements, be it excited, non-excited or terminated in a matched load.

Consider the two antenna element case where the unused element 2 is terminated in a load impedance Z_2^l, as shown in Figure 2.6. This changes Equation 2.32 to:

$$V_2 = -Z_2^l I_2. \tag{2.35}$$

Substituting this value into Equation 2.32, yields:

$$Z_2^l I_2 = Z_{22}I_2 + Z_{21}I_1. \tag{2.36}$$

Solving for I_2, substituting back into Equation 2.31 and dividing by I_1 yields an expression for the input impedance of antenna 1 (Z_1) in terms of the mutual impedance and self-impedance of both antennas, as well as the load impedance at the unused antenna 2 as:

$$Z_1 = Z_{11} - \frac{(Z_{12})^2}{Z_{22} + Z_2^l}. \tag{2.37}$$

The same formulation holds for antenna 2, due to reciprocity.

These derivations result in an equivalent circuit for element n as shown in Figure 2.5

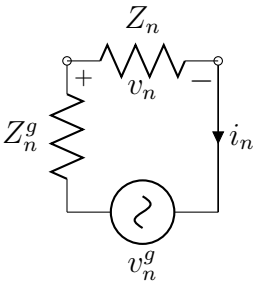

Figure 2.5: Equivalent circuit of an element in an array

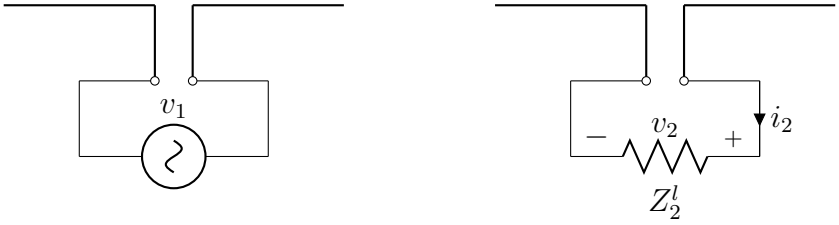

Figure 2.6: One element excited with second element terminated

In principle it is non-trivial to measure the Z-parameters of a network; however, they can be calculated from S-parameters which can be measured with a vector network analyser. This can be done using the following S- to Z-parameter conversion:

$$[Z] = \left[\sqrt{Z_0}\right] ([I] - [S])^{-1} ([I] + [S]) \left[\sqrt{Z_0}\right], \tag{2.38}$$

where $\left[\sqrt{Z_0}\right]$ is a diagonal matrix of the characteristic impedance Z_0.

Later in this thesis, an array study will be performed based on isotropic elements without mutual coupling. This would imply that direct control is available over the currents at the terminal. This is also called a *forced excitation* approach. While not very realistic, the reason for this method will be explained in detail.

The radiation pattern of an array is affected by mutual coupling and therefore, for an accurate model representation, it is necessary to include these effects when evaluating the performance of an array. This is called a *free excitation* approach.

Two approaches can be followed to incorporate mutual coupling in array analyses: using the embedded element patterns (EEP) which is called the *active element approach*, or compensating for it in the array excitations together with an isolated element pattern which is called the *isolated element approach*.

The EEP approach can be incorporated using the *pattern multiplication theorem* which states that the total radiation pattern of a finite array can be calculated as the product of the array factor and the EEP:

$$F(\theta,\phi) = \sum_{n=0}^{N-1} f_{en}(\theta,\phi) w_n e^{j\psi}, \tag{2.39}$$

where $f_{en}(\theta,\phi)$ is the EEP of an element n and can be measured by exciting only the nth element while all others are terminated in matched loads.

Measuring each EEP could be a tedious process in a large array. This is, fortunately, not the only solution and a different approach can be taken. In a sufficiently large regular array, all the elements experience the same coupling except for those close to the edges. A normalized central EEP is, therefore, a good approximation of the average EEP resulting in the following expression for $F(\theta,\phi)$:

$$F(\theta,\phi) = f_{ec}(\theta,\phi) \sum_{n=0}^{N-1} w_{\mathrm{n}} e^{jn\psi}, \tag{2.40}$$

where $f_{ec}(\theta,\phi)$ is a central embedded element pattern.

In the *isolated element pattern approach*, the weighting function w_n is redefined to include coupling effects. This can be done using the method described in [28]. Using this method, the coupling matrix $\mathbf{C}$ is first calculated as:

$$\mathbf{C} = (Z_0\mathbf{I} + \mathbf{Z})^{-1}, \tag{2.41}$$

where Z_0 is the characteristic impedance of the system and $\mathbf{Z}$ is the impedance matrix. The weighting coefficient (w_n) in the AF is then replaced with i_n, defined as:

$$i_{\mathrm{n}} = \sum_{m=0}^{N-1} C_{\mathrm{mn}} w_{\mathrm{m}} e^{jn\psi}, \tag{2.42}$$

where C_{mn} is an entry from the coupling matrix $\mathbf{C}$.

Finally, the radiation pattern of an array $F(\theta,\phi)$ can then be calculated using i_{n} and an isolated element pattern $f_{\mathrm{i}}(\theta,\phi)$ as:

$$F(\theta,\phi) = f_{\mathrm{i}}(\theta,\phi) \sum_{n=0}^{N-1} i_{\mathrm{n}} e^{jn\psi}. \tag{2.43}$$

This can also easily be extended to a planar array.

Obtaining accurate coupling measurements of an array can be difficult. Additionally, with the isolated patterns of each element in the array being prone to manufacturing tolerances, it is generally better to use the *active element approach* when the array is large enough such that the central EEP is a good approximation of all the EEP's in the array. This will be demonstrated in Chapter 4.

The scan performance of an array can drastically be affected by mutual coupling in the form of *scan blindness*. This is when the mutual coupling significantly reduces the transmitted or received power for certain scan angles. This can be shown when expressing the power received or transmitted at element n, for a certain scan direction as:

$$P_{\mathrm{n}} = P_{\mathrm{inc}} \left[1 - |\Gamma_{\mathrm{c}}(\theta_0, \phi_0)|^2\right], \tag{2.44}$$

where P_{inc} is the power incident at element n and Γ_{c} is the active reflection coefficient of a central element. The active element pattern can be expressed based on this as:

$$f_{ec}(\theta_0, \phi_0) = f_{\mathrm{i}}(\theta_0, \phi_0) \left[1 - |\Gamma_{\mathrm{c}}(\theta_0, \phi_0)|^2\right], \tag{2.45}$$

from which it can be seen that nulls can appear in $F(\theta, \phi)$ when $\Gamma_{\mathrm{c}} = 1$ for certain scan angles.

2.5 Beamforming Techniques

Uniform excitation will be implemented through-out this project, however, it is still important to discuss at least one non-uniform weighting technique to demonstrate how the relative side lobe level can be lowered and what the effects are on the beam pattern.

Beamformers can be classified as deterministic, adaptive or optimum. Adaptive and optimum beamformers are based on knowledge or assumptions of the incoming signal, whereas a deterministic beamformer is used to optimize the beam pattern of an array [26].

The beamforming algorithm that will be investigated is spectral.

2.5.1 Spectral Weighting: Sinusoidal

Spectral weighting is based on the fact that the beam pattern of a continuous aperture can be related to its weighting function using the Fourier transform [26]. This is done by expressing the current or voltage distribution across the array as samples of the weighting function. To illustrate this technique, sinusoidal weighing functions will be considered.

The cosine weighting function for an array with an odd number of elements steered to broadside can be calculated as[26]:

$$|w_n| = \sin\left(\frac{\pi}{2N}\right)\cos\left(\frac{\pi}{N}\left(\mathrm{n} - \frac{N-1}{2}\right)\right). \tag{2.46}$$

The advantages of uniform weighting, giving a narrower beam, can be combined with the cosine weighting to give a combined weighting function, called the raised cosine function defined as:

$$|w_n| = i(p)\left(p + (1-p)\cos\left(\frac{\pi}{N}\left(n - \frac{N-1}{2}\right)\right)\right), \tag{2.47}$$

with i(p) a constant defined as

$$i(p) = \frac{p}{N} + \frac{1-p}{2}\sin\left(\frac{\pi}{2N}\right) \tag{2.48}$$

The variable p has a range of [0,1], where $p = 0$ results in a cosine weighting function as described Equation 2.47, and $p = 1$ results in a uniform weighting function. The advantages of both can be mixed by selecting the value of p appropriately.

2.6 Beamforming: Analogue and Digital

Up to now the mathematics and theory involved in beamforming have been discussed. The next step is to investigate the practical implementation thereof.

When a signal arrives at an antenna, it passes through an LNA as was shown in Figure 2.1. Thereafter the question is raised of passing the signal directly to a digital chain for further processing or performing analogue processing first. In most cases, the answer lies in the system budget.

An all-digital system where each antenna is connected to a set of digital electronics gives almost full control over the array in terms of beamforming and signal processing. However, this would require an A/D converter at each antenna, which further requires a local oscillator that can introduce EMC. Additionally, it significantly increases the amount of processing power required.

The alternative is to pass the signal to an analogue beamformer first which can reduce the amount of processing power by beamforming multiple antennas simultaneously. Some of the advantages and disadvantages of each are summarised in Table 2.1.

Subject	Digital	Analogue
Clock distribution	Clock required at each element	No clock required
EMC due to electronics	Strong coupling due to digital signals	Minor coupling
Signal transport effects (gain and phase variation)	None	Variation, requiring extra signal conditioning
Electrical power requirements	High	Low

Table 2.1: Summary of digital and analogue beamformed tiles [3]

In some cases, analogue and digital beamforming are used together to form what is called a hybrid system. The EMBRACE system architecture as shown in Figure 2.7, is an example and will be discussed.

Four antenna elements are separately passed through an LNA and then combined on a single beamforming chip that produces two independent analogue beam signals. These signals are then passed to a digital back-end for further processing. The digital backend is responsible for A/D conversion, frequency sub-band filtering and finally, further beamforming. The latter processing step is to form what is called pencil beams within the analogue beams. This is clearly visible in Figure 2.7.

2.6.1 Analogue Beamforming

Analogue beamforming can practically be realised in two different ways. Using true time delays or equivalent phase delays. True time delays are implemented using physical delay lines in the form of printed microstrips. It is inherently wide-bandwidth, but it can be complicated to implement and requires significant space depending on its resolution.

Approximated phase delays, alternatively, can be implemented on a single integrated circuit the size of a fingernail using RC networks [2]. It does not hold the same wide-bandwidth advantage compared to true time-delays because they are frequency dependent; however, this problem can be solved by processing multiple frequency sub-bands to make up the full operational frequency band. To describe this method, the beamformer chip used by the EMBRACE system as described in [2] will be used as an example.

As described earlier, four antenna elements are combined on a single beamformer chip, where beamforming is achieved by applying the appropriate phase shift to each signal. This is achieved in [2] by using a polyphase resistor-capacitor (RC) network that has 8 phase steps spread evenly between 0° and 360°. With an RC filter only being able to generate a phase shift of 90°, initial

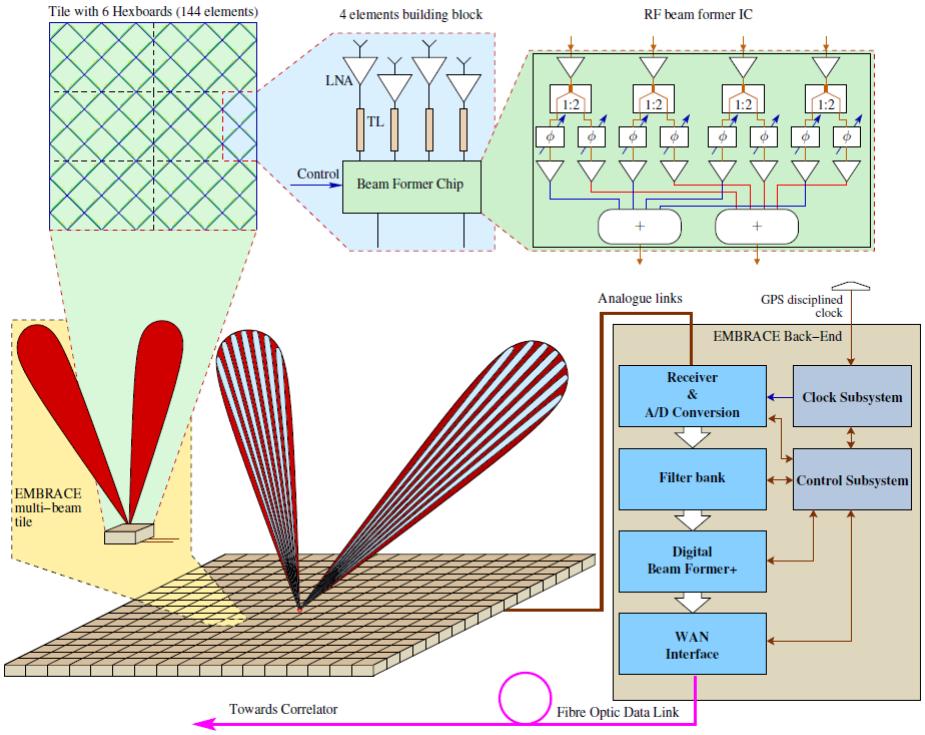

Figure 2.7: EMBRACE station architecture [1]

phase vectors are constructed consisting of 0°, 90°, 180° and 270° phase shifts. Additional phase shifts of 45°, 135°, 225° and 315° are constructed by vector addition of the first four phase shifts as illustrated by the vector diagram shown in Figure 2.8.
Note that magnitude errors are introduced as a result of the vector summation. This is under the assumption that both first stage input vectors are equal in magnitude. The resultant vector is fundamentally larger by a factor of $\sqrt{2}$. The practical implementation of a polyphase network holds further bandwidth and amplitude implications that need to be corrected.

An equivalent block diagram of the system is given in Figure 2.9.

2.6.2 Digital Beamforming

When the analogue data streams from the tile arrive at the digital back-end, they are digitised first, followed by filtering into sub-bands using a polyphase filter bank. An FFT operation is performed on each band to convert the digital samples to spectral samples. Further and final beamforming is then performed digitally by multiplying each spectral sample with a complex weight, effectively filtering them in magnitude and phase.

Time-delay beamforming can be emulated by buffering the digital data streams and summing them with other samples to create a "digital" beam. The

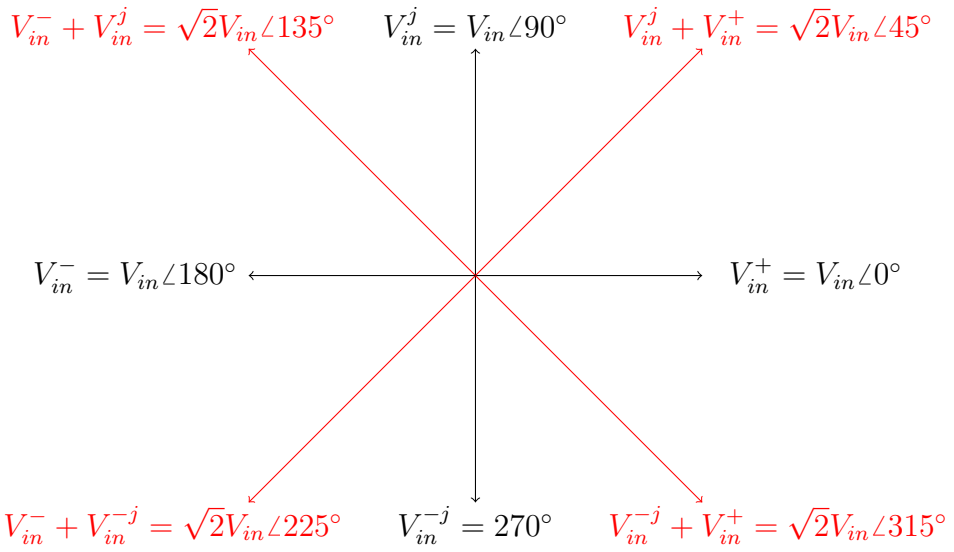

Figure 2.8: EMBRACE beamformer chip polyphase network vector diagram [2]

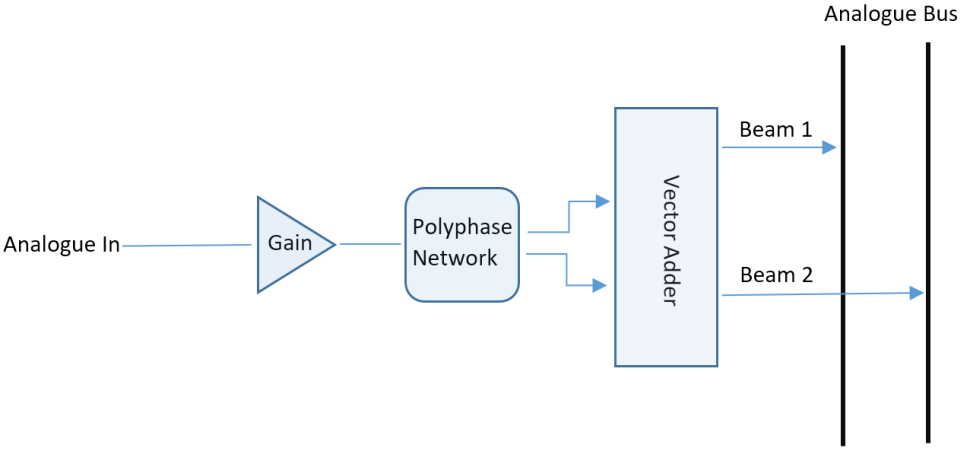

Figure 2.9: EMBRACE analogue beamformer block diagram [2]

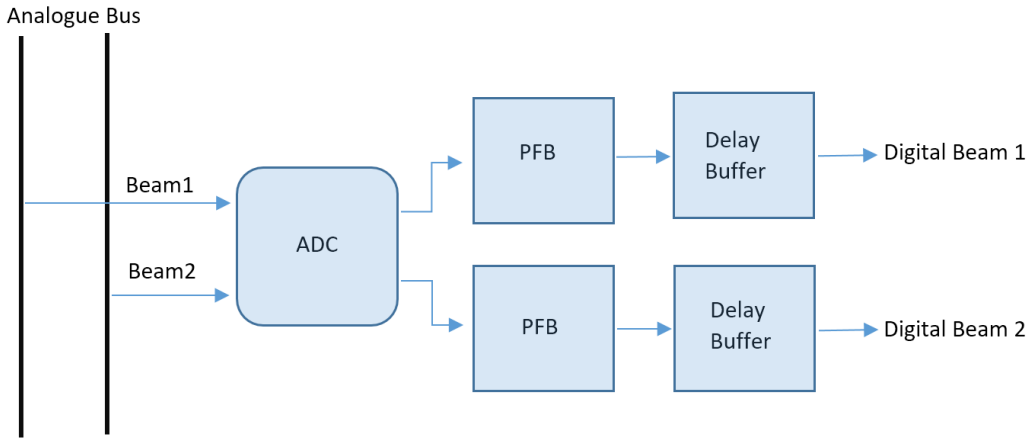

Figure 2.10: Digital beamformer block diagram [2]

latter beamforming process is illustrated in the block diagram in Figure 2.10. Repeating this process gives the ability to form multiple beams concurrently.

2.7 Beamforming: A Cost Case Study

The concept of quantized beamforming was briefly introduced in Section 2.6 where the practical implementation of beamforming was discussed. It was explained that any realistic beamformer is limited to a certain number of phase steps, which ideally would be infinite providing ideal performance in terms of scan accuracy and side lobe level. However, having a large number of phase steps, or high phase resolution, increases the complexity of the beamforming hardware. In the context of an analogue beamformer, this would translate to an increase in the amount of physical space as more printed delay lines or RC-networks are implemented to provide the extra time delay options.

Relating this to an increase in cost can be done by using the large scale integrated circuit (IC) package production cost estimation reported in [29] as:

$$\text{single IC package cost} = \frac{\text{process cost} + N_w C_w}{N_{IC}} + \text{test equipment cost}, \quad (2.49)$$

where N_w is the number of wafers required to produce all the ICs, C_w is the cost of a single wafer and N_{IC} is the number of ICs to be produced. The process and test equipment cost cannot be directly related to the complexity of the integrated circuit; however, it can be related to the number of wafers required as an increase in complexity can lead to a larger circuit area requirement, which directly influences the required wafer area.

On a small scale, an increase in cost might not be significant; however, when considering large-scale systems such as the SKA where millions of antennas are

planned to be implemented [21], a small increase in component cost can result in a significant increase in overall system cost.

Finding ways of decreasing overall system cost is generally of high interest, and it is, therefore, worthwhile to investigate the basic performance characteristics of certain system hardware, which for this project will be the beamforming hardware.

Consider the following example; as stated in Chapter 1, 1024 array stations are being planned for MFAA [21]. If these were to be filled with Vivaldi tiles, there would be a total of 30.4 million antennas. Using the beamforming chip (BFC) as described in [2], where four antennas are combined on a single chip, will result in a total number of chips (N_c) calculated as:

$$N_c = 30.4 \times 10^6/4 = 7.6 \times 10^6. \tag{2.50}$$

If the cost of a singe chip is denoted C_c, then the total system cost as a function of N_c can be expressed as:

$$C_{tot} = N_c C_c. \tag{2.51}$$

If a fractional reduction (P) in chip cost is achieved, then the total system cost saving can be expressed as:

$$\text{savings} = N_c C_c P = 7.5 \times 10^6 \times C_c P. \tag{2.52}$$

For example, if a fractional cost reduction of 10 percent is achieved ($P = 0.1$), then the total cost saving scales with $760 \times 10^3 \times C_c$. If C_c = EUR 1, then a total saving of EUR 760,000 is achieved, which is a significant amount for a single component regarding the MFAA preliminary budget as reported in [21].

It is therefore evident that it is worthwhile to investigate ways in which beamforming hardware complexity can be reduced.

2.8 Conclusion

This Chapter gave an overview of antenna arrays as deployed in radio astronomy. Dense and sparse configurations were presented, and their advantages and disadvantages were discussed in detail using mathematical descriptions of their properties.

The individual components and their role in the signal chain of a radio telescope were discussed. More detail was provided on the beamforming aspect, which is the focus of this thesis.

Classical array theory was presented with the aim of establishing the basic operation of a beamformer and the expressions used to described it.

A cost case study was successfully performed to motivate the investigation into reducing beamformer complexity with the intent of lowering the unit cost

of a beamformer as applied in large radio astronomy systems such as the MFAA.

Chapter 3

Quantized Beamforming: Forced Excitation Analyses

3.1 Introduction

In this Chapter, the effects of phase quantization in a beamformer will be investigated using array factor based beamforming without mutual coupling. The beamforming models used are therefore classified as *forced excitation* models implying direct control over the voltages and currents at the terminals of the antenna elements [22]. Using this method, the beamforming performance is determined purely as a function of the array configuration. Mutual coupling can be added by using the *pattern multiplication theorem*, as will be shown in Chapter 4.

For radio astronomy, a set of important beamforming performance metrics are identified as [9]:

- Main Beam Pointing Accuracy,
- Side Lobe Level (SLL).

A high pointing accuracy is of interest to ensure that the intended source is actually observed during an observation.

Low side lobe levels are desired to minimize the effects of nearby terrestrial RFI sources. Furthermore, high side lobe levels can cause directional ambiguity during an observation.

In Section 3.2 an introductory study based on a simple beamforming model will be used to demonstrate the importance of phase accuracy by determining the scan limitations that arise as result of phase errors specific to the model.

Sections 3.3 and 3.4 will serve as the core of this Chapter where an extensive study will be conducted to determine the effects of phase quantization on the performance metrics as listed above.

It is important to note this Chapter serves as a demonstration of the methodology used to evaluate the performance metrics based on a forced excitation model. The result does, however, provide valuable insight that can be applied to larger arrays.

The Chapter ends with a conclusion on the findings of this methodology and its relevance in beamforming for radio astronomy.

3.2 Linear Array Phase Quantization Effects: Simple Beamforming

This Section will focus on the phase quantization effects in a simple beamforming model. An analytical derivation will be done from which the scan accuracy and scan range in the visible region can be calculated. The results will be used to illustrate that extreme limitations can be observed in the scan range and scan accuracy when quantization is not done carefully.

In an ideal beamformer, β as expressed in Equation 2.14, can take on any typical value; however, in a practical beamformer, β is limited to a particular set of values due to a predefined phase resolution. The ideal and quantized phase (β_Q) terms should be distinguishable for the rest of this study and are therefore defined separately as:

$$\beta_{\mathrm{I}} = \beta = kd \sin\theta_0, \tag{3.1}$$

$$\beta_{\mathrm{Q}} = \beta_{\mathrm{I}} + \beta_{\mathrm{error}}, \tag{3.2}$$

where β_q is expressed as a function of the ideal phase term β_{I} and an inherent phase error, denoted β_{error}.

The process of deriving the model for this investigation is based on work done by the author of this thesis in [30].

As described in Section 2.4.1, the array factor will form maxima according to Equation 2.19 where values of $n \neq 0$ corresponds to grating lobes and $n = 0$ signifies the main lobe. The focus of this thesis is on dense broadside aperture arrays having hemispherical coverage, and therefore the scan range in the ϕ-plane is limited to $-90° < \theta_0 < 90°$, which implies that no grating lobes are expected in the visible region. This statement effectively restricts Equation 2.19 to $n = 0$. Equation 2.19 is now expressed under these conditions and in terms of the quantized phase shift β_{Q} as:

$$\psi - \beta_{\mathrm{Q}} = 0. \tag{3.3}$$

To find the angle (θ_{actual}) in which the array factor will form a maximum, ψ is substituted with its definition:

$$kd \sin \theta_{\text{actual}} - \beta_{\text{Q}} = 0. \tag{3.4}$$

Substituting Equation 3.2 into 3.4, and rearranging to make θ_{actual} the subject of the equation, yields:

$$\theta_{\text{actual}} = \sin^{-1}\left(\frac{\beta_{\text{I}} + \beta_{\text{error}}}{kd}\right). \tag{3.5}$$

The intended scan angle (θ_{ideal}) due to an ideal progressive phase shift (β_{I}) can be expressed as:

$$\theta_{\text{ideal}} = \sin^{-1}\left(\frac{\beta_{\text{I}}}{kd}\right). \tag{3.6}$$

The scan error (θ_{error}) can now be expressed as a function of Equations 3.6 and 3.5 as:

$$\theta_{\text{error}} = \theta_{\text{ideal}} - \theta_{\text{actual}}, \tag{3.7}$$

$$\theta_{\text{error}} = \sin^{-1}\left(\frac{\beta_{\text{I}} + \beta_{\text{error}}}{kd}\right) - \sin^{-1}\left(\frac{\beta_{\text{I}}}{kd}\right). \tag{3.8}$$

These derivations were done with the assumption that β_{Q} will be applied as a progressive phase shift along the array such that the phase at element n is given as $n\beta_{\text{Q}}$, where n signifies the index of the element. In this way, β_{Q} is determined to be the value closest to β_{I} after which it is progressively set to each element in the array. This results in an element phase plot as shown in Figure 3.1.

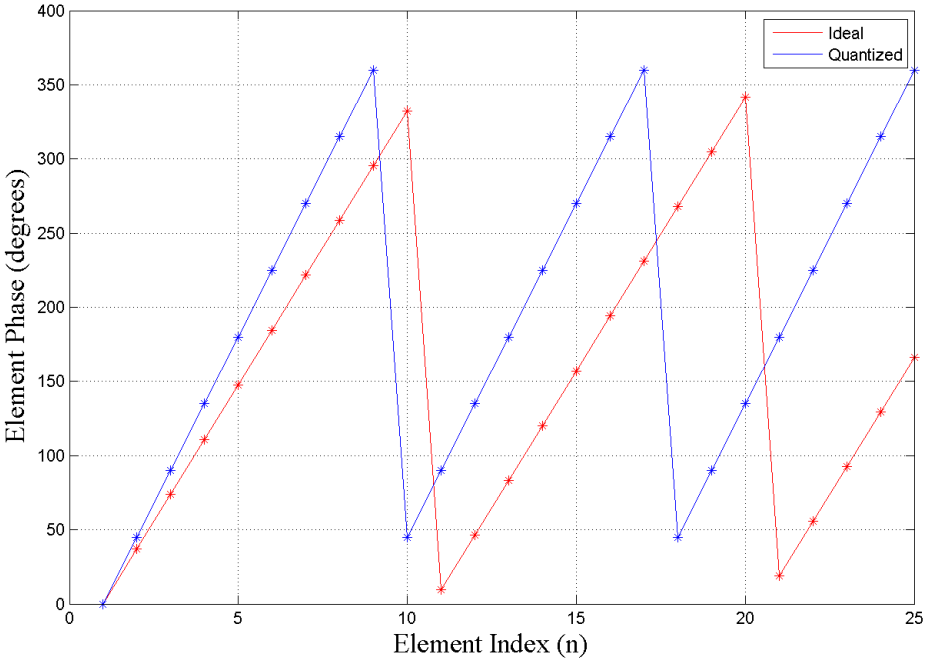

Figure 3.1: Wrapped element phase plot of an array scanned to 20° using a phase resolution of 45°

Inherent in this process is an increasing phase error as a function of n, which is evident in Figure 3.1.

To investigate this in more detail, Equation 2.16, which is the complex steering weight, is expressed as a function of β_{Q} ($\beta = \beta_{\mathrm{Q}}$) and uniform amplitude ($A_{\mathrm{n}} = 1$) for a linear array as:

$$w_{\mathrm{n}} = e^{-j\beta_{\mathrm{Q}}}. \tag{3.9}$$

This changes the linear array factor expression in Equation 2.6 to:

$$AF_{\mathrm{linear}} = \sum_{n=0}^{N-1} e^{j\left(n\psi - \beta_{\mathrm{Q}}\right)}. \tag{3.10}$$

Equation 3.10 is then expanded to include the phase error term (β_{error}) by substituting Equation 3.2:

$$AF_{\mathrm{linear}} = \sum_{n=0}^{N-1} e^{j(n\psi - \beta_{\mathrm{I}} + \beta_{\mathrm{error}})}, \tag{3.11}$$

from which it can be seen that the phase error at element n is given as $n\beta_{\mathrm{error}}$.

To illustrate, an element phase error plot is shown in Figure 3.2.

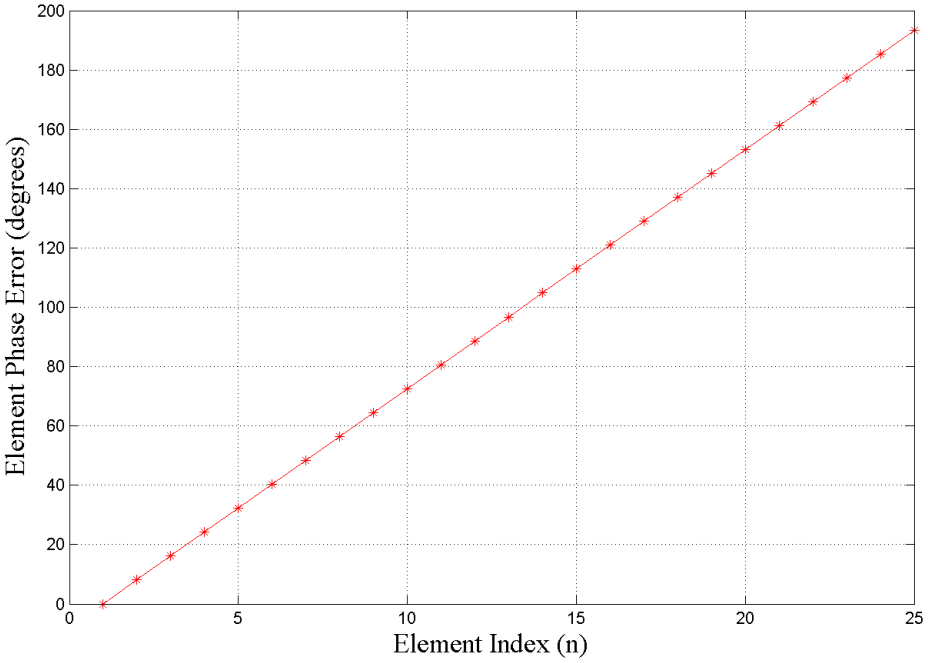

Figure 3.2: Phase error at element n of an array scanned to 20° using a phase resolution of 45°

It is evident that this type of implementation will result in inaccurate scan performance. With the inter element spacing restricted to be dense, the array is capable of steering to imaginary space as was discussed in Section 2.4. As a result, very little power will be received.

This can be avoided by limiting the arguments of both terms in Equation 3.8 to $|\arg| < 1$. The scan range in the visible region will therefore be limited by the values of k, d and β_{error}.

In the process to determine the maximum scan range, it is necessary to evaluate these parameters and the values for which the array will attempt to scan to imaginary space.

It is known that a maximum quantization error will occur whenever β_{I} is exactly between two quantization levels. The maximum phase error (β_{error}) can, therefore, be expressed as:

$$\beta_{\text{error(max)}} = \pm\frac{\beta_{\text{res}}}{2}, \tag{3.12}$$

where the phase resolution (β_{res}) is determined according to the total number of bits (B) available to the beamformer as:

$$\beta_{\text{res}} = \frac{2\pi}{2^B}. \tag{3.13}$$

This results in an expression for β_{I}, specific to this situation as:

$$\beta_{\mathrm{I}}^{'} = -\pi + \frac{(2b+1)\,\pi}{2^B},\ b = 0, 1, 2 \ldots 2^B - 1 \tag{3.14}$$

where b corresponds to the index of a quantized phase value.

Furthermore, Equation 3.8 can be reduced to three variables by relating the inter-element spacing d to a density ratio (R) which is defined as:

$$R = \frac{d_0}{d}, \tag{3.15}$$

where d_0 is the reference spacing. It has already been established that the study is limited to dense arrays. The reference spacing is, therefore, selected as $d_0 = \lambda/2$. The inter element spacing is then related to R as:

$$d = \frac{\lambda}{2R}. \tag{3.16}$$

When combining this with the wavenumber term (k) in Equation 3.8, the dependence on λ is removed all together:

$$kd = \frac{2\pi}{R}. \tag{3.17}$$

Frequency information is now implied by R. For example, when $R = 1$, the inter-element electrical length is $\lambda/2$. So for a fixed d, the frequency can be derived from the value of R.

By doing it this way, it is easier to study and visualise the array performance as a function of the electrical length between the elements. The array beamforming performance is therefore determined as a function of its operational frequency band by varying R. This is an important formulation that will be used throughout this thesis.

The k and d terms in Equation 3.8 is substituted with R as follows:

$$\theta_{\mathrm{error}} = \sin^{-1}\left(\frac{\left(2b - 2^B\right) R}{2^B}\right) - \sin^{-1}\left(\frac{\left(2b + 1 - 2^B\right) R}{2^B}\right). \tag{3.18}$$

The value of b for θ_{actual} is limited to the visible region as follows:

$$\left\lceil \frac{2^{B-1}\,(R-1)}{R} \right\rceil < b < \left\lfloor \frac{2^{B-1}\,(R+1)}{R} \right\rfloor. \tag{3.19}$$

The maximum scan range in the visible region can now be determined by the phase index values (b) as limited by specific values for R and B. A study is performed to determine the scan ranges as a function of the variables summarised in Table 3.1.

The calculated scan range results are shown in Figure 3.3. It can be seen that an increase in the density ratio results in a decrease in the scan range for

Variable	Range	Remark
Density ratio (R)	[1,4]	Implied electrical length variation of d: $\left[\frac{\lambda}{2}, \frac{\lambda}{8}\right]$
Bits available to beamformer (B)	[1,10]	Phase resolution variation of: $[180°, 0.35°]$

Table 3.1: Summary of the variables and their ranges that were used to determine the scan range

a constant number of bits. As a result, a large number of bits are required to maintain a high scan range across a wide density ratio range, or in other words, across a wide range in the operating frequency band of the array under consideration.

The results for the calculated maximum scan error is shown in Figure 3.4 for the same variables as described in Table 3.1. As expected, an increase in the number of bits results in a decrease in the maximum scan error. Additionally, the error increases as the density ratio increases. This goes on to show that a large number of bits are required to maintain a relatively constant maximum scan error across a wide density ratio range.

The reason for this can be explained by the fact that the quantized array is inherently limited in scan angle options because it can only apply progressive phase shifts as a function of its phase resolution. This is clear when expressing the phase term as:

$$\beta_{\mathrm{n}} = n\left(b\beta_{\mathrm{res}}\right), \tag{3.20}$$

where β_{n} is the phase at element n and $b\beta_{\mathrm{res}}$ is a b-multiple of the phase resolution.

This might not be a problem for a variable point to point communication system where the transmitters and receivers are in fixed positions; however, this method will be inadequate for dynamic applications such as radar, or more specifically in the light of this project, radio astronomy systems that require fine scan steps [1]. It is therefore necessary to investigate a more practical beamforming method. This will be done in the next Section.

3.3 Linear Array Phase Quantization Effects: Discrete Phase Control

As seen in Section 3.2, it is critical to have sufficient phase control when considering beamforming for radio astronomy. However, in reality, a beamformer will always have a limited phase resolution and it is therefore necessary to optimize the way in which these limited phase options are applied. This is

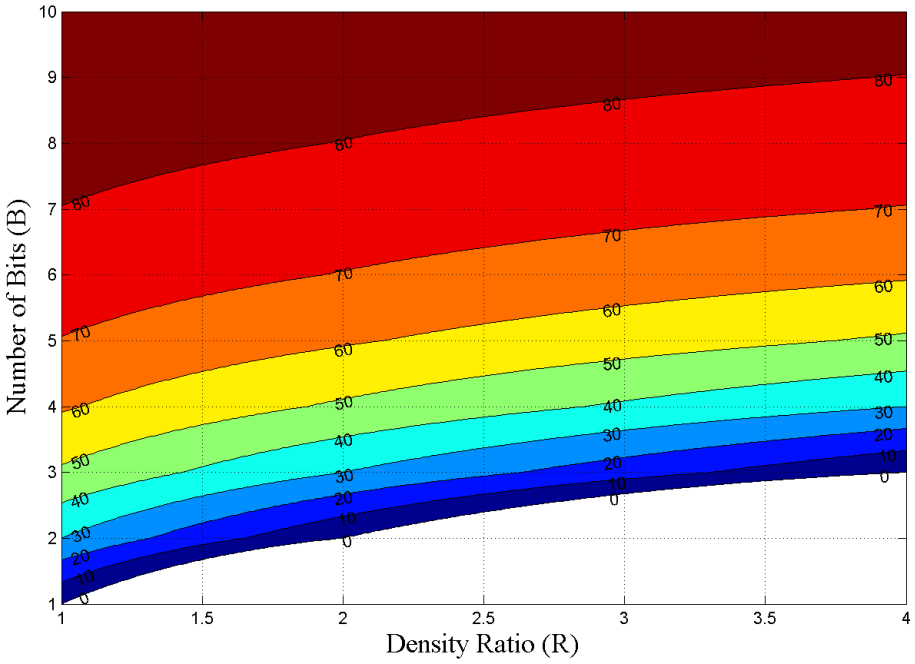

Figure 3.3: Maximum scan range in degrees as a function of the the density ratio and number of bits available to the beamformer.

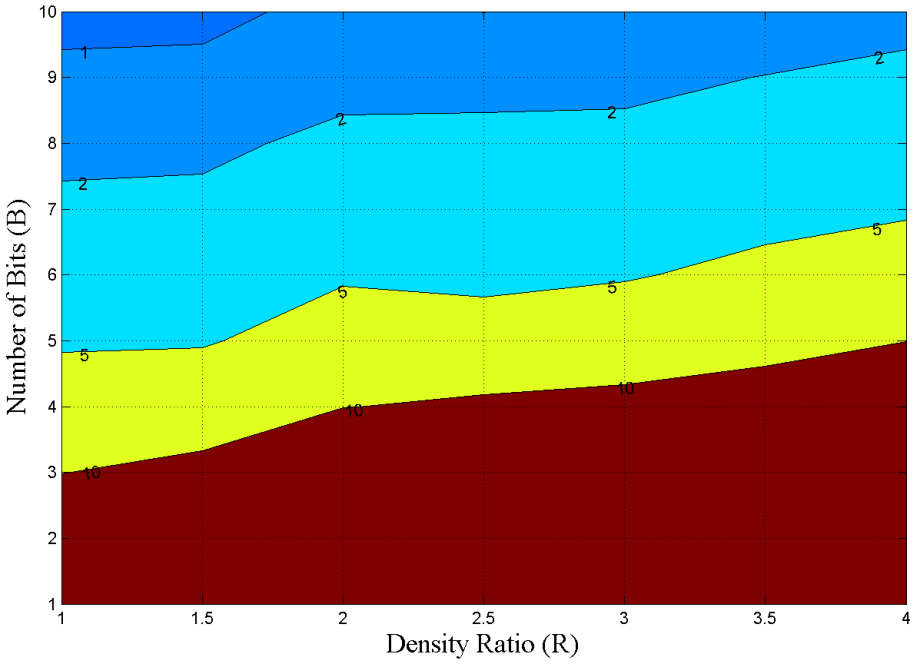

Figure 3.4: Maximum scan error in degrees as a function of the density ratio and number of bits available to the beamformer.

done by applying an optimal phase setting at each element. Optimal in this case is defined as the closest phase to the ideal phase setting at that element. This would seem an obvious choice, however, other phase shift algorithms exist that does not necessarily apply the closest to ideal phase shift at each element. An example is the *Delta-Sigma* implementation in [28] where phase shifts are optimally applied to provide good scan accuracy and lower the side lobe level at the same time.

This Section introduces discrete phase control at each element. As such, the quantized phase term β_Q is redefined as an element-specific quantized phase term (β_{Qn}).

The quantized phase at element n is calculated to be the closest available phase to the ideal phase. This is done by initially dividing the ideal phase term with the phase resolution and rounding to the nearest integer. The closest phase can then be determined as the product of this integer and the phase resolution. In mathematical terms, this can be described as:

$$\beta_{\mathrm{Qn}} = \left\lfloor \left(\frac{n\beta_{\mathrm{I}}}{\beta_{\mathrm{res}}} \right) + 0.5 \right\rfloor \beta_{\mathrm{res}}, \tag{3.21}$$

where n is the index of the element under consideration. The expression can further be simplified to:

$$\beta_{\mathrm{Qn}} = \left\{ \frac{n\beta_{\mathrm{I}}}{\beta_{\mathrm{res}}} \right\} \beta_{\mathrm{res}}, \tag{3.22}$$

where the curled braces indicate a rounding operator which rounds the fraction to the nearest integer.

An example element phase plot is shown in Figure 3.5 of an array on which this algorithm is applied. As expected, phase errors are still present; however, unlike using progressive quantized phase shifts as in the previous Section, these phase errors are limited to a maximum of $\beta_{\mathrm{res}}/2$. To illustrate this, a corresponding phase error plot is shown in Figure 3.6. Note that the phase errors are periodic. This will have a significant impact on the SLL as will be shown and discussed in Section 3.3.3.

3.3.1 Scan Accuracy

With a significant reduction in average phase error, a significant reduction in scan error is expected as well. However, by applying discrete phase control it is not possible to determine the scan error analytically and therefore it has to be determined numerically by simulation.

Similar to the previous Section, the performance will be determined as a function of the density ratio (R) and the number of bits (B) available to the beamformer.

For simulation purposes, it is necessary to discuss the beam pattern effects of the inter-element spacing. It is necessary that the half-power main lobe is

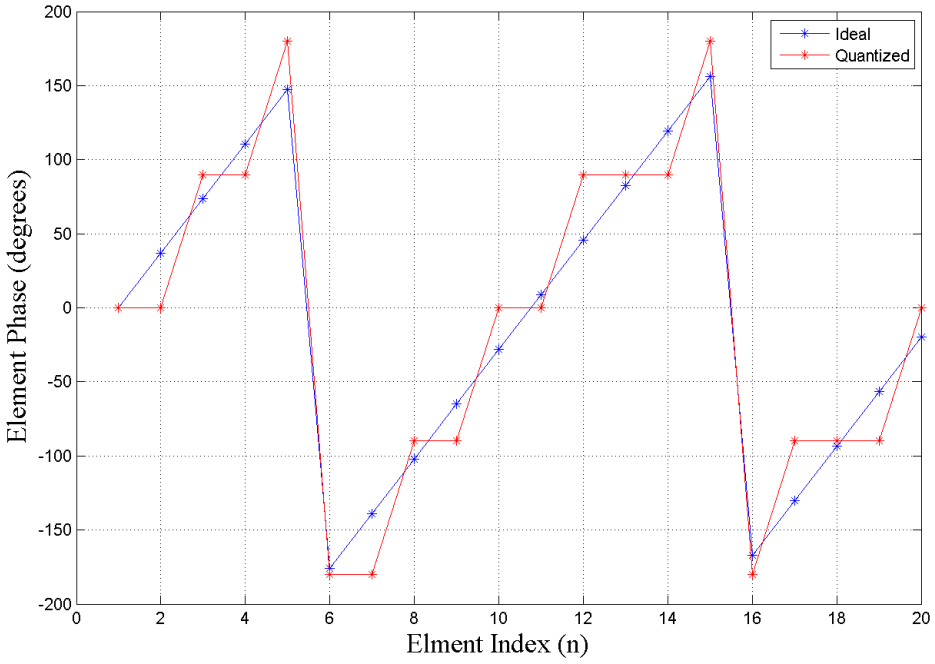

Figure 3.5: Phase at element n of an array scanned to 20° with a phase resolution of 45°

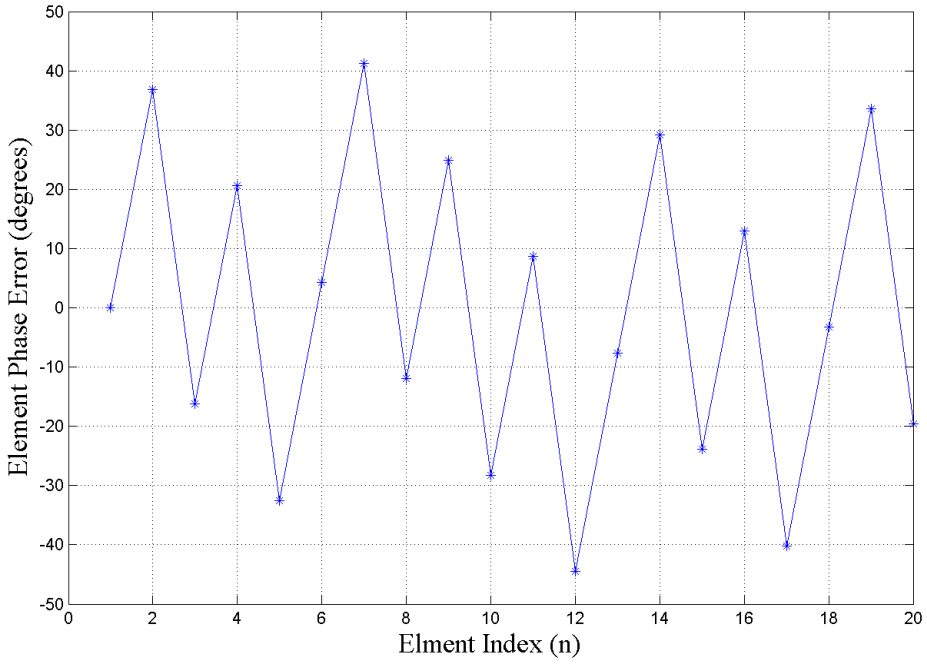

Figure 3.6: Phase error at element n of an array scanned to 20° with a phase resolution of 45°

always defined to the extent that both -3 dB points of the main lobe exist for any given scan angle. θ_0.

The half-power beamwidth (HPBW) of the array is therefore a critical beam property that needs to be considered because it changes as a function of the inter-element spacing. The HPBW of a regular linear broadside array was already is given in [26] as:

$$\text{HPBW} = 2\sin^{-1}\left(0.446\frac{\lambda}{Nd}\right). \tag{3.23}$$

With R defined as d_0/d where $d_0 = \lambda/2$, Equation 3.23 can be written as a function of R as:

$$\text{HPBW} = 2\sin^{-1}\left(0.446\frac{2R}{N}\right). \tag{3.24}$$

From this, it can be seen that an increase in N will lead to a decrease in the HPBW. Similarly, an increase in R will also lead to an increase in HPBW. Furthermore, when scanning off-broadside, the inter-element spacing as observed along the scan angle decreases as a function of $\cos\theta_0$ which also results in an increase in the HPBW.

For a scanning uniform linear broadside array, this effect can be taken into account when scanning by using the following HPBW expression given in [26] as:

$$\text{HPBW}_{\theta_0} = \cos^{-1}\left[\sin\theta_0 - 0.446\frac{2R}{N}\right] - \cos^{-1}\left[\sin\theta_0 + 0.446\frac{2R}{N}\right]. \tag{3.25}$$

To ensure that a well defined main lobe is maintained across the scan range, the scan range will be limited to the angle $\theta_{0\text{max}}$ where either of the half-power points of the main lobe ceases to exist within the visible region. That is, when either half power point in the main lobe moves beyond $-90°$ or $90°$.

To illustrate, the maximum scan angle $\theta_{0\text{max}}$ as a function of R for an array with $N = 100$ is shown in Figure 3.7.

In [31] a simulation was performed by the author to determine the scan accuracy as a function of density ratio and the total number of bits. In that specific case, the array length was kept constant while the number of elements was varied by changing the density ratio which simply implies that more elements are added to the array. This was based on the same methods used in [28]. However, this is not very practical because an array can not dynamically change its number of elements. The motivation for this method as explained in [28], is to retain the beam pattern of the array as the density ratio changes so that the beam pattern effects that are investigated can be identified more clearly.

The study in [31] is now adapted to that of a practical array, which implies that the array length and number of elements will be kept constant. The

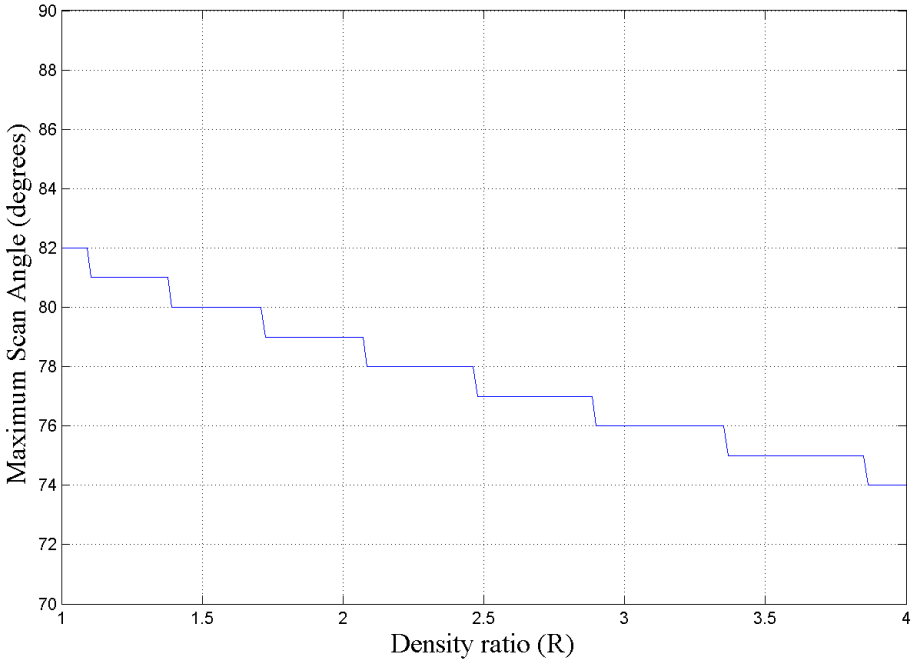

Figure 3.7: Maximum scan angle $\theta_{0\max}$ as a function of R

Variable	**Range/Value**	**Remark**
Element spacing (d)	0.09m	DDA inter-element spacing
Number of elements (N)	100	$L = 20\lambda$ at $f_0 = 1$GHz
Density ratio (R)	[1,4]	Implied d electrical length variation of: $\left[\frac{\lambda}{2}, \frac{\lambda}{16}\right]$
Scan range	$\theta_0 \in [0°, \theta_{0\max}]$	$\theta_{0\max}$ limited by existence of both main lobe -3dB points
Bits available to beamformer (B)	[1,7]	Phase resolution variation of: $[180°, 2.82°]$

Table 3.2: Scan accuracy for simulation variables

array length (L) is chosen as 20λ at a centre frequency f_0 of 1 GHz. The inter-element spacing (d) is based on that of a Dense Dipole Array tile prototype which is 0.09 m. The Dense Dipole Array is introduced in Chapter 4.

A study is performed to determine the scan accuracy statistics as a function of R and B. A summary of the simulation variables is provided in Table 3.2.

The maximum scan error results are shown in Figure 3.10. The corresponding off-broadside scan angle at which the maximum error occurs is shown in

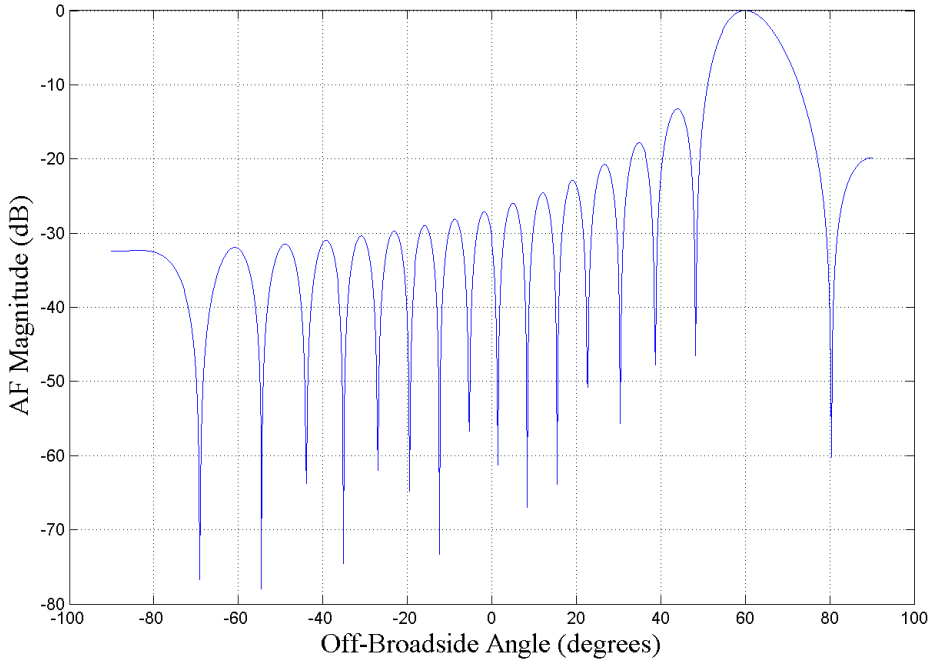

Figure 3.8: Asymmetric beamwidth increase of an array scanned to 60°

Figure 3.11. The mean scan error is shown in Figure 3.12.

As expected, the highest maximum and mean errors occur in the one-bit case. An increase in R results in an increase in the maximum and mean error. It is also noted that these maximum errors occur at scan angles beyond 60° where most are actually located beyond 80°. For the one- and two-bit cases, the maximum and mean errors almost double for the density ratio range. It is further noticed that the maximum errors are much higher than their respective means, which indicates that they occur for very specific scan angles.

The reason for the increasing scan error as a function of increasing R can be explained by the beamwidth and the effects of a grating lobe starting to move into the visible region at the edge of the scan range. It was shown that the beamwidth increase as a function of scan angle; however, the widening is not symmetrical around θ_0 because of the $\sin\theta$ dependence of the beam pattern.

A beamwidth increase as a function of R is, therefore, coupled with an asymmetric increase as a function of θ_0. An example is shown in Figure 3.8 where it can be seen that the main lobe is wider to the right than to the left of the maximum point. This becomes more apparent when scanning further from broadside.

When scanning close to the edge of the scan range a partial grating lobe becomes visible and adds constructively with the main lobe. At some stage, it starts to flatten the main lobe to such an extent that the maximum point begins to shift, albeit slightly. An example of a grating lobe interfering with

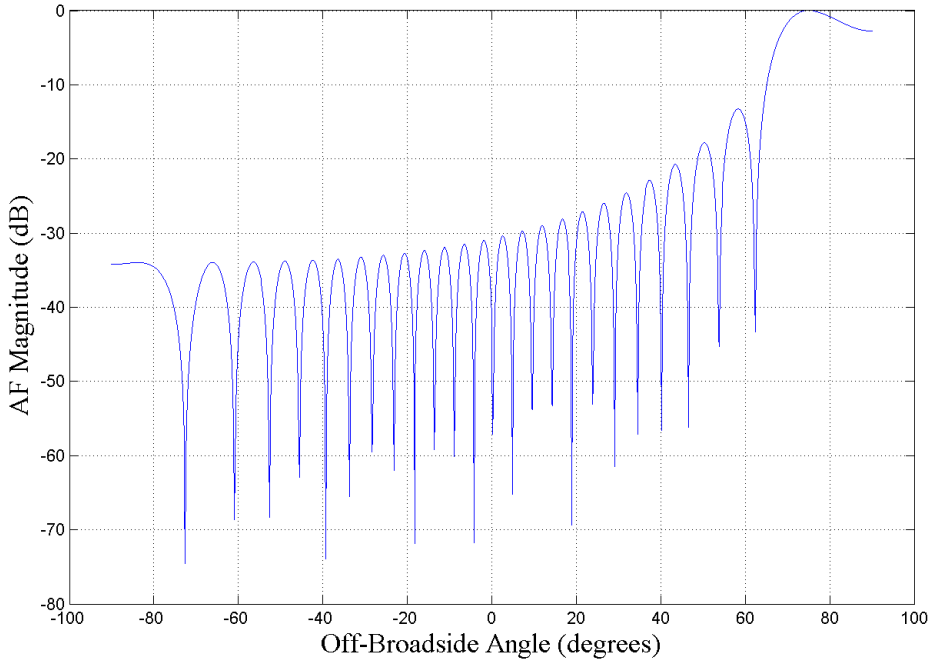

Figure 3.9: Main lobe deformation at edge of scan range

the main lobe is shown in Figure 3.9.

Therefore, any basic scan error observed in the region for which this occurs can be "amplified" when the maximum point of the quantized main beam starts shifting as a result of this effect. The flattening increases towards the edge of the scan range and therefore it is expected that this error "amplification" effect will be at a maximum at the edge of the scan range. This amplification effect will further be referred to as the *edge scanning effect*

This explanation can be confirmed by observing the angular positions at which the maximum error occurs as shown in Figure 3.11. There are some cases, however, where the maximum error does not necessarily occur at or close to the edge of the scan range. These are simply special cases where the errors are higher at this specific scan angle and density ratio than what is caused by the *edge scanning effect*. This happens when the basic scan errors at the edge of the scan range, if any, are low enough so that after amplification it does not reach a significant level. To clarify, a basic scan error is purely a result of phase errors as encountered across the whole scan range.

This effect will be more pronounced when the beam broadening effects as initially discussed are incorporated. This is because of the maximum-point-shift as a function of the *edge scanning effect* increases when the beam is flatter prior to the combination with a grating lobe. This is obvious when considering the fact that the main beam will now need less contribution from the grating lobe to flatten asymmetrically.

In summary, the *edge scanning effect* has a significant contribution to the scan error only when a large enough basic scan error is present in the region for which it is observed.

Discussion

This study provided significant insight into the behaviour of the scan accuracy as a function of certain array parameters. Although based on a constant array length with a constant number of elements, the behaviour, in general, should remain the same with a different number of elements.

The maximum scan errors were shown to occur at scan angles beyond 60° while most were seen to occur beyond 80°. This is a significant result in the sense that most arrays will be unable to scan to these angles and maintain practical performance. This is due to mutual coupling changing the impedance of the array as a function of scan angle. This will be observed in Chapter 4 when mutual coupling is incorporated in these performance models.

Furthermore, it was shown that the scan accuracy is relatively high, even for low bit-resolutions. This is significant because the implementation of a one-bit beamformer is a very attractive option for designers due to its simplicity. It will, however, be shown in the following Section that the beam pattern of a one-bit beamformer presents an inherent complication which could cancel out the simplicity trade-off.

3.3.2 Side Lobe Level

The effects of phase quantization is not limited to variations in scan accuracy. Side lobe level (SLL) is another aspect of the array that is influenced. For the purposes of the study in this Section, the beam pattern of an array with ideal phase control and quantized phase control are referred to as $f_{\mathrm{I}}(\theta)$ and $f_{\mathrm{Q}}(\theta)$ respectively. It should also be mentioned that all the studies conducted are normalized.

The side lobes of $f_{\mathrm{I}}(\theta)$ are a result of periodic constructive and destructive interference of individual elements in the array. Phase quantization can change this periodicity, resulting in SLL variations.

When quantization is performed according to Equation 3.22, phase errors are periodic and can, therefore, cause periodic constructive side lobe interference. This results in quantization lobes of which an example is shown in Figure 3.13 (indicated with an asterisk).

A quantization lobe can cause the array to receive power from unintended directions, which can result in directional ambiguity during astronomical observations. It is therefore important to determine the angular behaviour and amplitude extents of a quantization lobe as a function of the array parameters.

For a dense uniform linear array with isotropic elements, the normalized SLL will approach -13.3 dB when the number of elements is large [22]. With

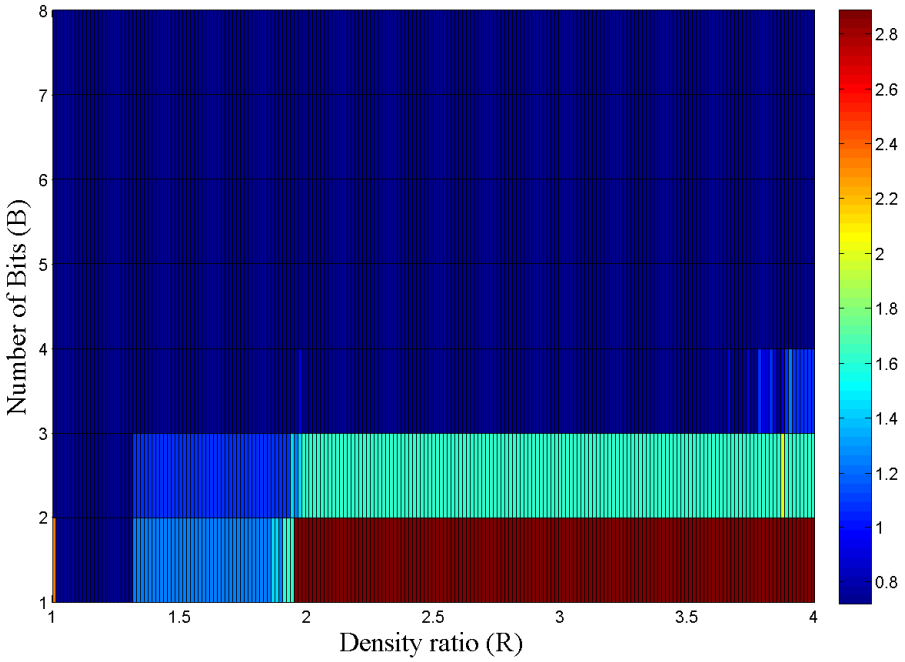

Figure 3.10: Maximum scan error in degrees as a function of the variables shown in Table 3.2

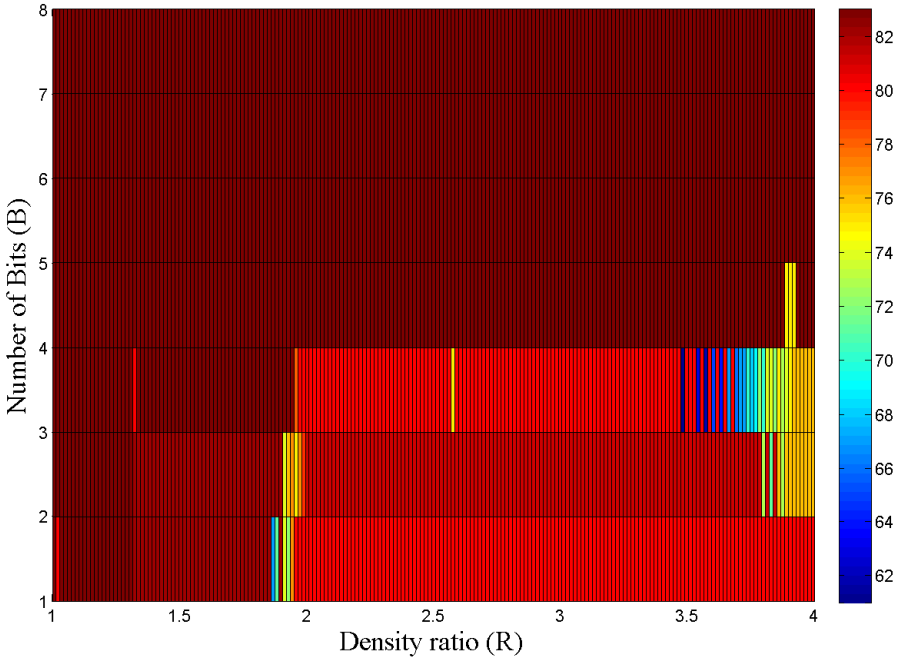

Figure 3.11: Maximum scan error off-broadside position in degrees as a function of the variables shown in Table 3.2

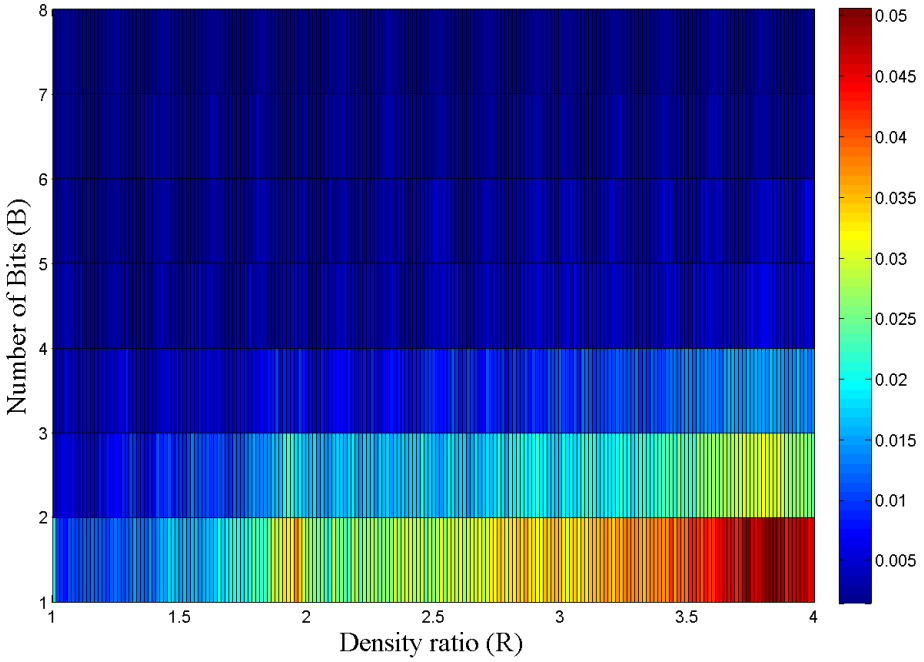

Figure 3.12: Mean scan error in degrees as a function of the variables shown in Table 3.2

the normalized side lobe level of a 20 element array given in [22] as -13 dB, it is safe to state that the normalized SLL of a 100 element array will be somewhere between -13 and -13.3 dB, as this is a 5-fold change in N.

The amplitude of a quantization lobe is a function of the array parameters and its amplitude extents are therefore unknown at this stage. To effectively identify a quantization lobe with a significant amplitude a reference is needed, which is chosen to be the first side lobe (FSL) of $f_{\mathrm{I}}(\theta)$. A quantization lobe is therefore said to have amplitude significance when it is higher than the FSL.

In the ideal case, the highest side lobe will be the first side lobe (FSL). By scanning across the visible region and identifying the highest side lobe relative to the main lobe, it is possible to identify a quantization lobe with relative amplitude significance and its angular position.

This study will be performed for the two- and three-bit cases. It will be shown that the one-bit case is entirely different to higher bit-cases and cannot be studied in a similar manner.

Quantization lobes are not the only result of phase errors. General pattern noise, which is defined as:

$$f_{\mathrm{noise}} = |f_{\mathrm{I}}(\theta) - f_{\mathrm{Q}}(\theta)|, \tag{3.26}$$

is also observed. This is a direct result of the incoherent phase combination of individual elements and as a result, breaks the periodicity in the side lobes.

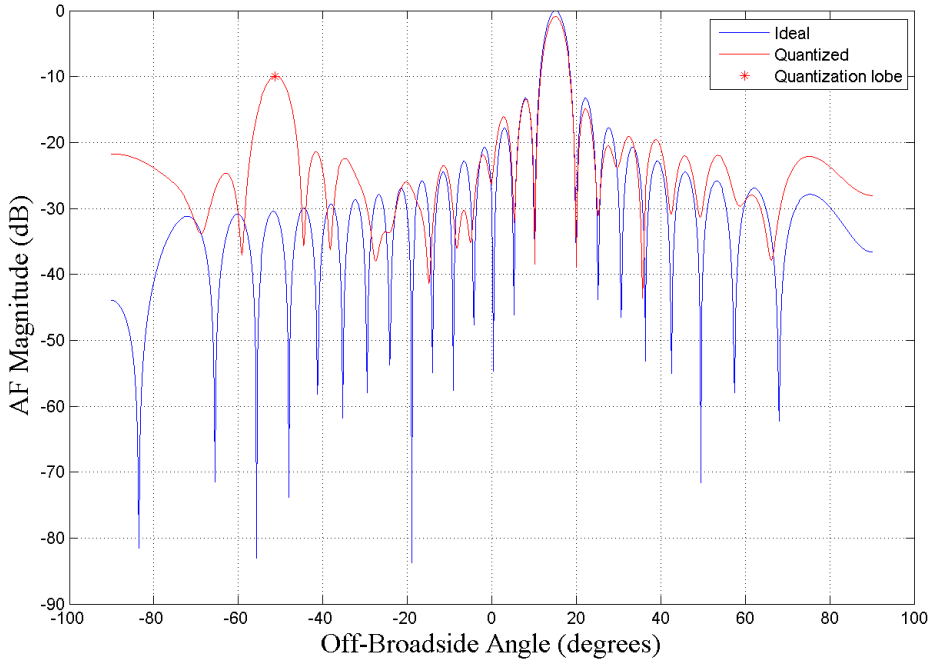

Figure 3.13: Array factor example of side lobe variations due to phase quantization

For a fixed value of B the distribution of this noise is dependent on the inter-element spacing as a function of wavelength. The noise amplitude range is directly related to the phase resolution. Pattern noise of this type will be referred to as secondary noise, while the noise contribution of a quantization lobe will be referred to as primary noise. This is because the pattern noise as defined in Equation 3.26 is generally dominated by quantization lobes. Additionally, the behaviour of each is mostly independent of each other.

With the first part of the study focusing on the amplitude extents of the side lobes to determine whether significant amplitudes exists under specific conditions, it is also necessary to determine the pattern noise distribution. This will be done by analysing the signal to quantization noise ratio (SQNR) for a set of array parameters.

3.3.2.1 Highest Side Lobe Level: Two-Bit Case

The results for the two-bit case are shown in Figures 3.14 and 3.15 where 3.14 shows the highest side lobe relative to the main lobe as a function of R and θ_0, and 3.15 shows its corresponding angular position.

The scan range for this part of the study was limited to 80° in order distinguish a quantization lobe from the grating lobe that appears at higher off broadside scan angles. This is a reasonable limitation since the scan range of

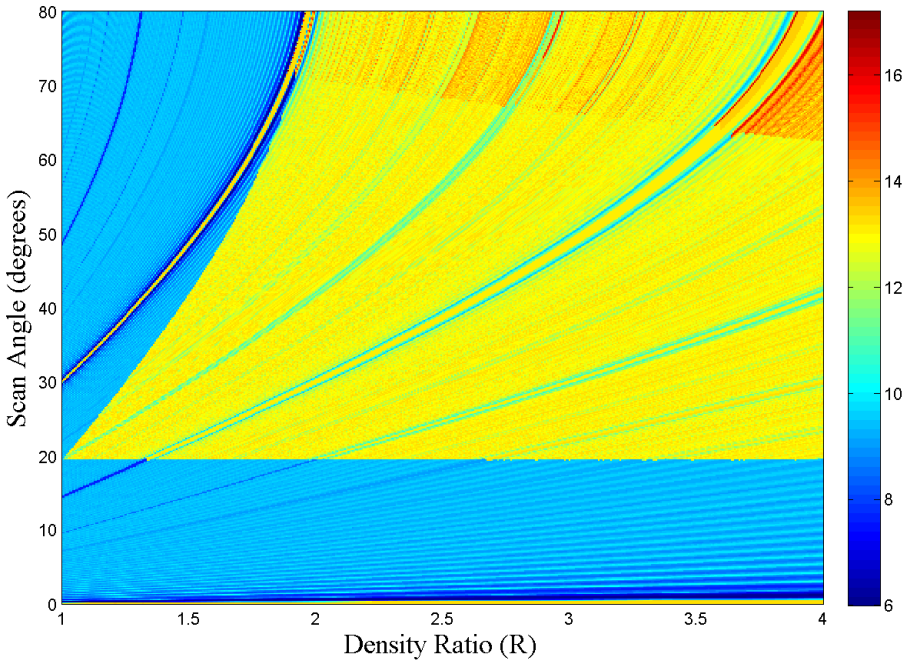

Figure 3.14: Normalized highest side lobe relative to main lobe in dB for the two-bit case

practical dense aperture arrays is limited by the beamwidth of the individual elements, which do not offer full hemispherical coverage.

The number of elements N in the array is fixed to 100 and therefore it is expected that the highest side lobe will be around -13 dB. With this said, a side lobe with significant amplitude is distinguishable in Figure 3.14 when considering the regions where the amplitude is higher than -13 dB.

For very specific cases, the amplitude reach as high as -6 dB. This result can be explained by referring to the corresponding position plot in Figure 3.15. Note that when scanning from 0° towards 20°, the highest side lobe is initially located close to the main lobe, indicating that it is the FSL. This is because a quantization lobe combines constructively with the FSL.

It is also noted that the quantization lobe has a close to constant position for any R and only changes as a function of θ_0 for the scan angle range defined as $\theta_0 \in (0°, 20°)$. In fact, the position is related to θ_0 in a quadratic manner. The quantization lobe eventually moves out of the visible region when scanning beyond 20°.

The apparent amplitude ripple for scan angles smaller than 20° is due to the quantization lobe combining with the side lobes as it moves across the visible region. The ripples become wider with an increase in R due to the beamwidth increasing concurrently.

A similar situation is encountered for scan angles smaller than 20° and

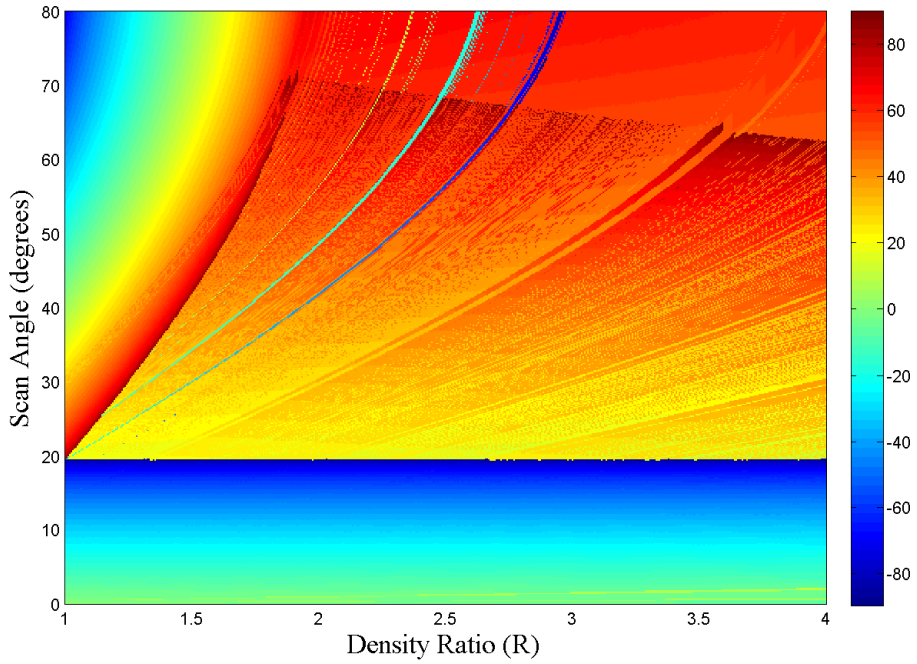

Figure 3.15: Highest side lobe position in degrees for the two-bit case

density ratio values smaller than 2. A quantization lobe appears in the visible region at $\theta = 90°$ and moves across the visible region towards $\theta = -90°$, again as a quadratic function of θ_0. At some point, depending on R and θ_0, the quantization lobe combines constructively with the first side lobe, resulting in a -6 dB amplitude. Notice that the quantization lobe disappears for a brief period (highest side lobe = -13.3 dB) and then reappears resulting in the symmetric blue-yellow-blue streak. This is because the quantization lobe first combines with the right FSL, moves into the main lobe, and then out the left side, combining with the left FSL. The same holds for the rest of the results ($\theta_0 > 20°$, $R > 2$), however, with quantization lobes now lower in amplitude, the constructive FSL interference results in amplitudes of only -10 dB.

Further, it is noted that there are specific situations where the highest amplitude lowers down to -16 dB. The reason for this can be explained by the right FSL moving out of the visible region when scanning beyond a certain angle, and destructive interference in the left FSL occurs simultaneously. This situation is also co-dependent on the beamwidth which is a function of R, further explaining why these situations occur earlier in the scan range with an increase in R.

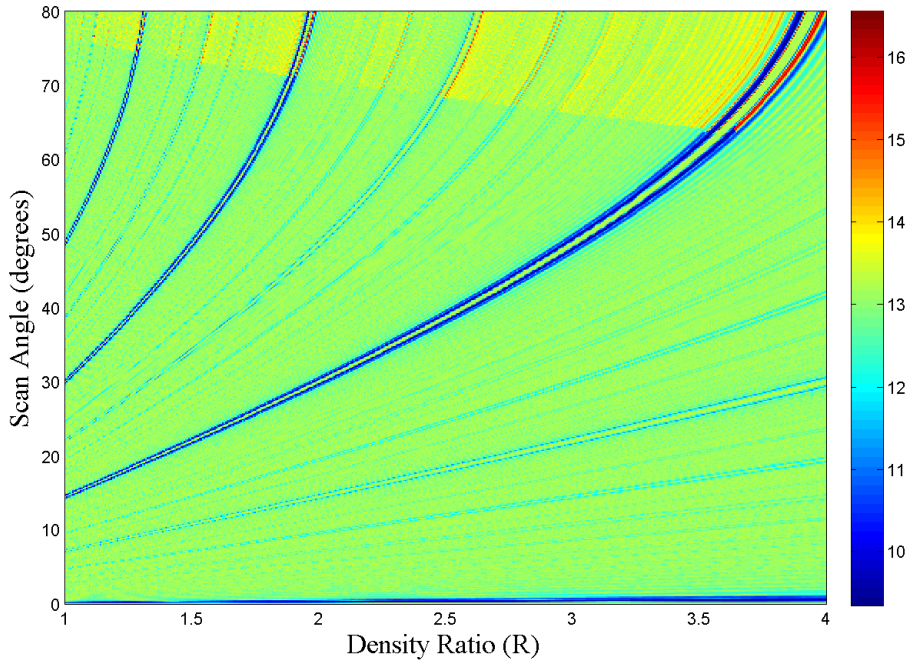

Figure 3.16: Normalized highest side lobe relative to main lobe in dB for the three-bit case

3.3.2.2 Highest Side Lobe Level: Three-Bit Case

The results for the three-bit case are shown in Figures 3.16 and 3.17 where 3.16 shows the highest side lobe relative to the main lobe as a function of R and θ_0, and 3.17 shows its corresponding angular position.

The scan range is again limited to $\theta_0 \in [0°, 80°]$, for the same reason as described earlier.

The first notable difference when compared to the two-bit case is that the average highest side lobe level is much closer to -13 dB. This is expected due to an increased phase resolution. There are, however, specific regions in the plot where the side lobe level reaches amplitudes of around -10 dB and -12 dB. This can be explained by quantization lobes moving in the visible region as a function of θ_0, and at certain angles combines constructively with the first side lobes. This is confirmed when referring to the corresponding angular position plot in Figure 3.17 where it is noted that the significant amplitudes are located close to the main lobe.

For scan angles larger than 60°, the highest side lobe amplitude can reach as low as -16 dB. This can again be explained by the fact that the right FSL moves out of the visible region when scanning towards 90°, and at the same time, for very specific situations, destructive interference occurs in the left FSL. This occurs earlier in the scan range as R is increased, due to the beamwidth

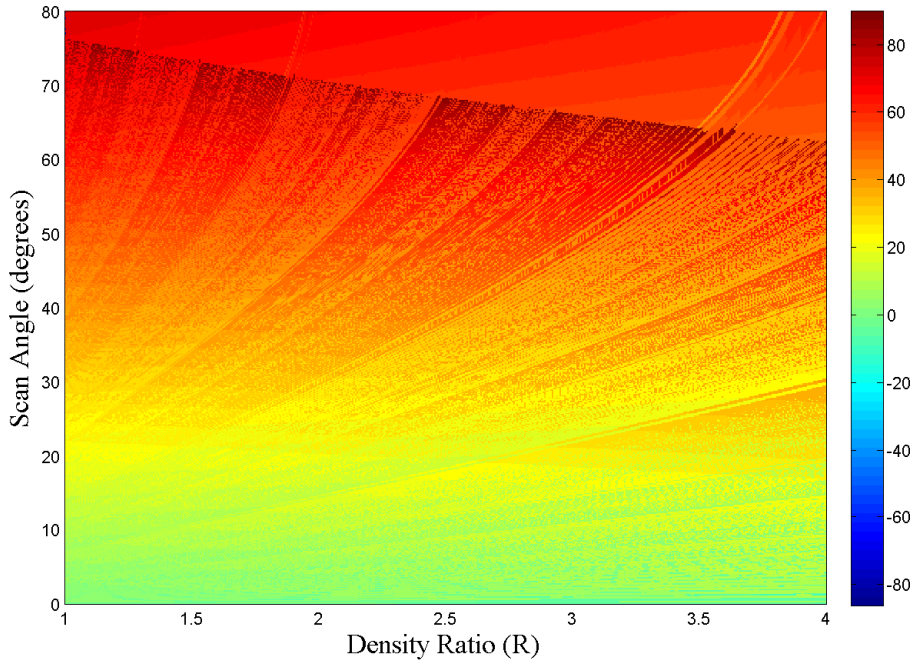

Figure 3.17: Highest side lobe position in degrees for the three-bit case

increasing.

3.3.2.3 Highest Side Lobe Level: One-Bit Case

With only two phase states available when performing one-bit phase quantization, the array is unable to differentiate between opposite azimuth angles [32]. As a result, a symmetric main lobe is formed in the $\phi + 180°$ plane. An example is shown in Figure 3.18.

All pattern noise is noted to be symmetrical as well. This effect complicates the application of this study and will therefore not be investigated. However, its noise distribution is subject to the same effects to those of higher bit-cases and will be studied in more detail in Section 3.4.2.

3.3.2.4 Main Lobe Amplitude Loss

With additional power now possibly directed into the side lobes as a result of phase quantization errors, an amplitude loss in the main lobe is observed. This can be quantified by expressing the loss as a fraction of the ideal amplitude:

$$\text{fractional loss} = \frac{max\left\{AF_{\text{I}}\right\} - max\left\{AF_{\text{q}}\right\}}{max\left\{AF_{\text{I}}\right\}}. \tag{3.27}$$

A simulation is performed to determine the fractional loss as a function of scan angle and the total number of bits. The number of elements is kept

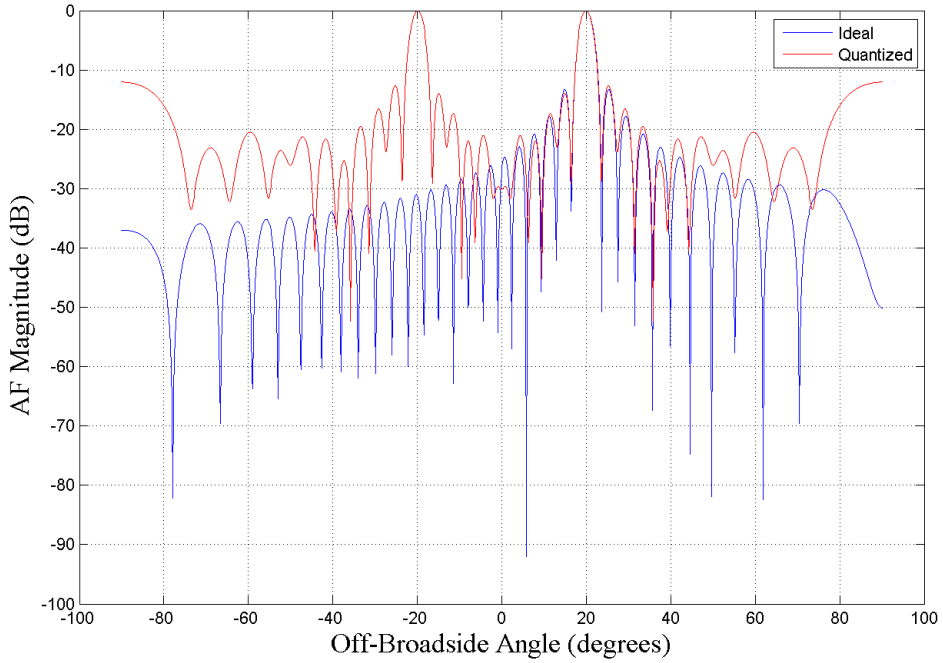

Figure 3.18: Array factor with one-bit phase quantization, scanned to $\theta_0 = 20°$

constant at 100 to ensure that the amount of available power in the array factor is kept constant.

The results are shown in Figures 3.19 and 3.20, where 3.19 shows the fractional loss in percentage, as a function of the number of bits B and scan angle θ_0, and 3.20 shows the mean with one standard deviation of the same data.

As expected, there is a significant decrease in the loss when increasing the number of bits. The significant loss for the one-bit case can be explained by the power being divided between the two main lobes.

It was shown that quantization lobes have significant amplitude presence in the two-bit case for the full scan range and most density values, which contributes significantly to the amount of pattern noise in the side lobes. The three-bit case has less quantization lobe effects.

The highest side lobe level studies confirmed that the quantization effects reduces significantly when increasing B from 2 to 3, however, it was not clear what the relationship is. These results answer this question by showing that the effects reduce in an exponential manner with an increase in B.

Discussion

This study provided insight into the SLL and pattern noise behaviour as a function the array parameters in focus.

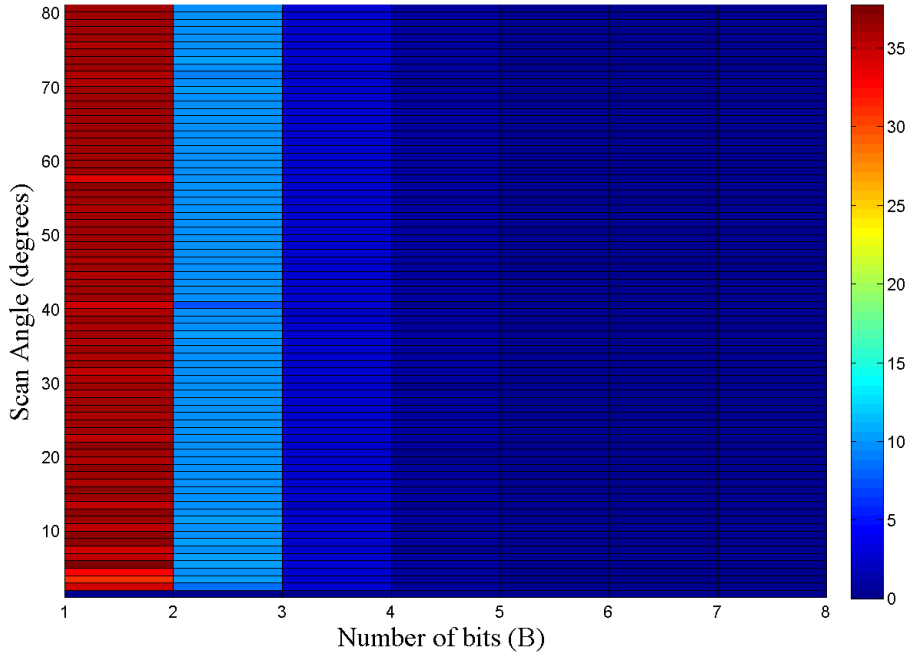

Figure 3.19: Percentage amplitude loss in main lobe versus scan angle θ_0 and number of bits B

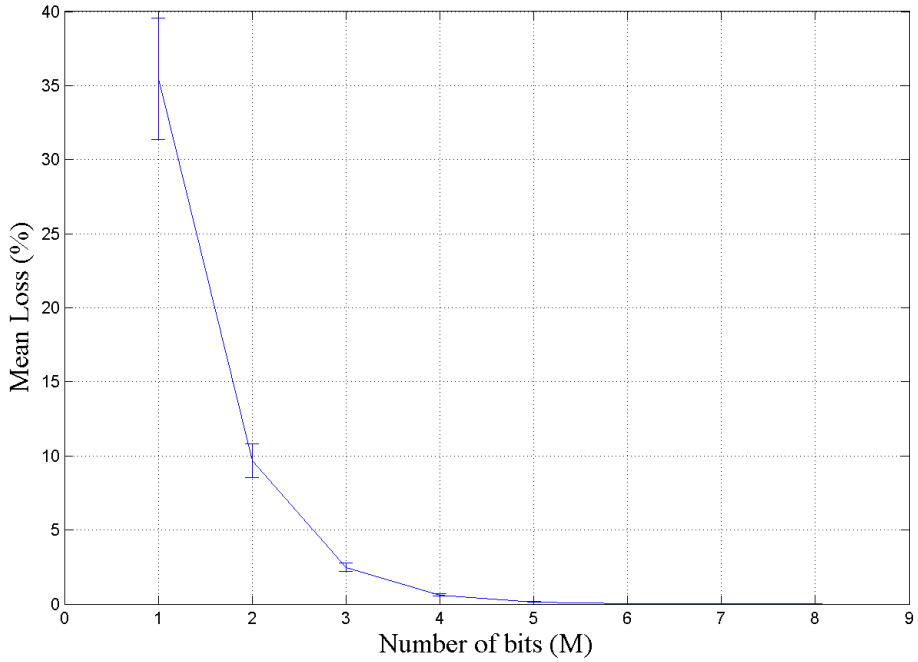

Figure 3.20: Mean amplitude percentage loss with standard deviation versus number of bits B

It should be noted that the SLL can be controlled to a certain extent by using tapered amplitude excitation as was discussed in Chapter 2. Furthermore, quantization lobes can be mitigated by applying random a phase offset at each element. When quantized, this effectively breaks the periodicity in the phase errors [33] which are responsible for quantization lobes. Another method is to spread out the quantization lobes by using an aperiodic or semi-random distribution of elements [32], similar to the methods used to counteract grating lobes in sparse arrays as discussed in Section 2.3.

The second main lobe that is formed in the one-bit case can be mitigated either by processing it using similar techniques that are used to process grating lobes in regular sparse arrays [25], or by using element cell rotation as described in [32].

3.3.3 Overall Beam Pattern Performance

The next step in determining the effects of quantization errors is to characterise the total pattern performance. A similar process to that in [28] will be followed whereby the pattern noise is characterised according to the signal to quantization noise ratio (SQNR), defined as:

$$SQNR = \frac{P_{\mathrm{I}}}{P_{\mathrm{error}}}, \tag{3.28}$$

where P_{I} is the amplitude of the main beam in the ideal power pattern ($|f_{\mathrm{I}}(\theta_0)|$), and P_{error} is the mean of the average pattern noise for all scan angles in the visible region defined as:

$$P_{\mathrm{error}} = \frac{\sum_{n=1}^{N} \overline{f_{\mathrm{noise}}(\theta)^2_{\theta_0=\theta_{\mathrm{n}}}}}{N}, \theta_n \in [-90, 90]. \tag{3.29}$$

With this definition, P_{error} is equivalent to the mean squared error (MSE) of the average pattern error ($f_{\mathrm{I}}(\theta)$) [28] when scanning iteratively through the visible region:

$$P_{\mathrm{error}} = \mathrm{MSE} = E\left[f_{\mathrm{noise}}(\theta)^2\right]. \tag{3.30}$$

Finally, Equation 3.28 is rewritten in terms of Equation 3.30 and the definition of P_{I} as:

$$\mathrm{SQNR} = \frac{|f_{\mathrm{I}}(\theta_0)|^2}{E\left[f_{\mathrm{noise}}(\theta)^2\right]}. \tag{3.31}$$

To determine the SQNR performance of an array, a simulation is performed where the SQNR is calculated for both a variable and a constant number of elements. The variable number of elements is determined according to a fixed array length chosen as 20λ, where the number of elements is determined

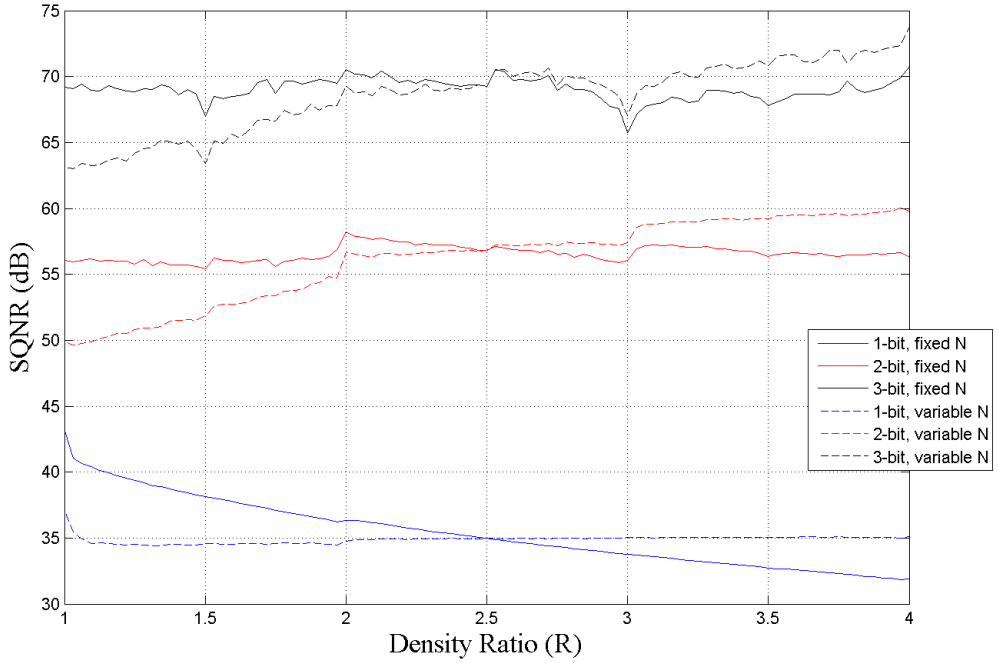

Figure 3.21: SQNR

according to L/d. With the density ratio defined as $R = d_0/d$ where $d_0 = \lambda/2$, the number of elements (N) can be related to the array length in terms of R as:

$$N = 40R; \tag{3.32}$$

By doing it this way, it can be shown how the SQNR varies as a function of the number of elements in a fixed array length. It should, however, be noted that an increase in density physically implies that more elements are added to the array and therefore the inter-element spacing decreases. This is only useful when considering a narrowband array where a decision needs to be made on the number of antennas that will be used in a fixed aperture size. It will, however, be mainly used to explain certain findings in the results.

The results are shown in Figure 3.21. As expected, the average SQNR increases significantly with an increase in the number of bits. This can be explained by the SLL studies where it was shown how the effects of quantization lobes reduce exponentially as a function of B and as a result also reduce the average pattern noise significantly.

To explain the SQNR results for the array with a variable number of elements, it is necessary to consider the beam properties of such an array. The beamwidth and directivity are determined by the aperture size and number of elements to first order [28]. Therefore, by maintaining a constant array length and only varying the number of elements, the beamwidth remains constant

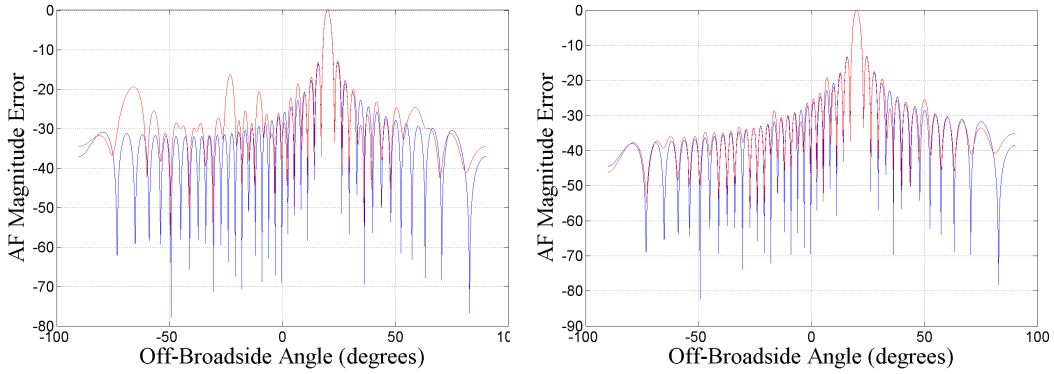

(a) (b)

Figure 3.22: Visualisation of pattern noise shaping effect for a fixed array length with a variable number of elements scanned to 20°, for $R = 1$ (a) and $R = 4$ (b)

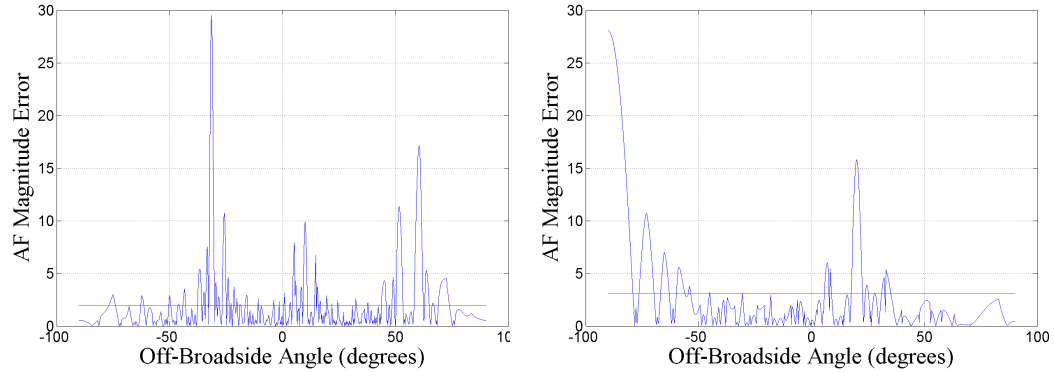

(a) (b)

Figure 3.23: Array factor magnitude error with mean indicated by the red horizontal line, for $R = 1$ (a) and $R = 4$ (b)

while only the amount of power in the pattern changes. By normalizing the array weights, the effects of power variations as a function of R are eliminated, resulting in the SQNR to be dependent only on the beam pattern.

The steady increase in SQNR with an increase in the density ratio for this array type is a result of the pattern noise distribution changing as a function of R. The pattern noise is "pushed", or "shaped", towards imaginary space as a result of an increase in density ratio. This is an effect that is directly related to the inter-element spacing and is therefore applicable to both array types under consideration in this study. An example of this effect for a variable number of elements array is shown in Figure 3.22.

The reason for this can be explained by the spatial equivalence of oversampling in the temporal domain. By sampling faster than the Nyquist criteria

in analogue to digital converters (ADC's), quantization errors are forced to appear at higher frequencies than the original signal [28]. The equivalence of this in the spatial domain is sub half-wavelength element spacing, effectively resulting in spatial oversampling. As a result, quantization errors are forced to imaginary space, therefore confirming the observation shown in Figure 3.22.

Quantization lobes are a result of periodic phase errors and are therefore independent of this effect; however, it's amplitude might vary slightly due to its combination with pattern noise. With this said, it is evident that although pattern noise might be shaped to imaginary space as a function of R, the overall noise might still be dominated by quantization lobes, resulting in a slow increase in SQNR as a function of R.

The SQNR for an array with a constant number of elements has very little increase as a function of R. In this type of array, an increase in R results in an increase in the beamwidth. Beam broadening is applicable to quantization lobes and pattern noise as well and, therefore, an apparent increase in the mean pattern error is observed which effectively decreases the SQNR.

An example of this observation is shown in Figure 3.23 which is an example plot of Equation 3.26 for an arbitrary scan angle. The mean pattern error is indicated by the red horizontal line. This observation is in balance with the noise "shaping" effects that occur with an increase in R. Therefore, no general increase in the SQNR is observed with an increase of R.

It is further noted that the one-bit case experiences no general increase in SQNR as a function of R. In fact, the SQNR for the array with a constant number of elements generally decreases. This can be explained by the dominant noise contribution of the second main lobe which increases as the beamwidth increases. The noise contribution of the second main lobe in the array with a variable number of elements stays constant as a function of R. Nevertheless, it remains a dominant source of pattern noise and therefore little to no improvement in the SQNR is observed as a function of R.

Also note that the average SQNR increases significantly when increasing B from 2 to 3, compared to the increase when increasing B from 1 to 2. This again confirms the exponential relationship between the pattern noise and B.

The two-bit SQNR experiences a significant increase in SQNR just before $R = 2$, after which it generally lowers until just after $R = 3$. This holds for both the variable and constant N arrays. In Figure 3.14 it is seen that a quantization lobe dominates most of the scan range for $R < 2$ and therefore the SQNR as well. For $R > 2$ quantization lobes generally no longer have significant amplitude levels and only causes significant amplitudes when combining with a FSL.

Discussion

It was shown that the average SQNR has a non-linear relationship with the number of bits, which goes on to confirm the results obtained in Section 3.3.2.4.

When comparing the average SQNR of the one- and two-bit cases, it is seen that the difference between the two is much lower when compared to the difference between the two- and three-bit cases. Due to the average SQNR of the two-bit case being closer to the one-bit case than the three-bit situation, goes on to show that the pattern noise contribution of quantization lobes are indeed significant in the two-bit case as was shown in Section 3.3.2.

3.4 Planar Array Phase Quantization Effects: Discrete Phase Control

In the previous Section, the effects of phase quantization were established for a linear array where a general understanding was obtained of the pattern noise distribution and its dependence on various array parameters. The analyses will now be extended to a planar array.

A regular uniform planar array as was introduced in Chapter 2, is simply a dimensional extension to a linear array. With a linear array consisting of N elements placed on the x-axis, a planar array is formed by placing another N such arrays on the y-axis, effectively forming a $N \times N$ planar array.

The planar array can be expressed as a product of the array factors of the arrays in the x and y directions as:

$$AF_{\text{planar}} = AF_{\text{x}} AF_{\text{y}}, \tag{3.33}$$

where AF_{x} and AF_{y} are defined in terms of quantized phases β_{Qxm} and β_{Qyn} as:

$$AF_{\text{x}} = \sum_{m=0}^{M-1} A_m e^{j\left(m\psi_{\text{x}} - \beta_{Qxm}\right)} \tag{3.34}$$

$$AF_{\text{y}} = \sum_{n=0}^{N-1} A_n e^{j\left(n\psi_{\text{y}} - \beta_{Qyn}\right)}. \tag{3.35}$$

The quantized phases are calculated according to Equation 3.22 as:

$$\beta_{\text{Qxm}} = \left\{ \frac{m\beta_{\text{Ix}}}{\beta_{\text{res}}} \right\} \beta_{\text{res}}, \tag{3.36}$$

$$\beta_{\text{Qyn}} = \left\{ \frac{n\beta_{\text{Iy}}}{\beta_{\text{res}}} \right\} \beta_{\text{res}}, \tag{3.37}$$

where β_{res} is determined according to Equation 3.13.

From this derivation it can be seen that the beam pattern $\text{F}(\theta, \phi)$ in the $\phi = 0°$ and $\phi = 90°$ planes, also called the principal planes, will simply be

the array factors $AF_{\mathrm{x}}(\theta,\phi)$ and $AF_{\mathrm{y}}(\theta,\phi)$ respectively. The pattern in the off-principal planes also called the inter-cardinal planes, will have low side lobes due to the pattern multiplication of the principal plane patterns [22].

Therefore, any pattern error that is a result of phase quantization will have maximum effects in the principal planes, while the pattern error in the inter-cardinal planes is expected to be lower due to the separate linear array factor multiplication. This can be seen when expressing Equation 3.33 in terms of the their individual errors $A\hat{F}_{\mathrm{x}}$ and $A\hat{F}_{\mathrm{y}}$ as:

$$AF_{\mathrm{planar}} = \left(AF_{\mathrm{x}} + A\hat{F}_{\mathrm{x}}\right)\left(AF_{\mathrm{y}} + A\hat{F}_{\mathrm{y}}\right). \tag{3.38}$$

Multiplying out results in:

$$AF_{\mathrm{planar}} = AF_{\mathrm{x}}AF_{\mathrm{y}} + AF_{\mathrm{x}}A\hat{F}_{\mathrm{y}} + AF_{\mathrm{y}}A\hat{F}_{\mathrm{x}} + A\hat{F}_{\mathrm{x}}A\hat{F}_{\mathrm{y}}. \tag{3.39}$$

The beamforming performance of the planar array will be investigated by performing similar studies to those of the linear array in Section 3.3. The performance metrics that will be evaluated are the scan accuracy and overall pattern noise.

The beam patterns of an array using ideal and quantized phases are defined as $f_{\mathrm{I}}(\theta,\phi)$ and $f_{\mathrm{Q}}(\theta,\phi)$ respectively. The pattern noise is then defined as:

$$f_{\mathrm{noise}}(\theta,\phi) = |f_{\mathrm{I}}(\theta,\phi) - f_{\mathrm{Q}}(\theta,\phi)|. \tag{3.40}$$

3.4.1 Pointing Accuracy

It is necessary to limit the scan angle θ_0 to the angle where any -3 dB point ceases to exist in the visible region, as was explained in Section 3.3.1. The half-power beamwidth of a planar array is defined in two separate planes. One is defined in the plane where $\phi = \phi_0$ and the other in the plane perpendicular to it. The half-power beamwidth of each plane is denoted Θ and Ψ respectively and can be calculated as follows [26]:

$$\Theta = \sqrt{\frac{1}{\cos^2\theta_0\left[\Theta_x^{-2}\cos^2\phi_0 + \Theta_y^{-2}\sin^2\phi_0\right]}}, \tag{3.41}$$

$$\Psi = \sqrt{\frac{1}{\Theta_x^{-2}\sin^2\phi_0 + \Theta_y^{-2}\cos^2\phi_0}}, \tag{3.42}$$

where Θ_x and Θ_y is the half-power beamwidths of broadside linear arrays with M and N elements respectively.

Equation 3.41 is used as an approximation for the purpose of limiting θ_0 so that a full half-power main beam is always defined.

The mean scan accuracy of a 20×20 planar array as a function of R and B is shown in Figure 3.24.

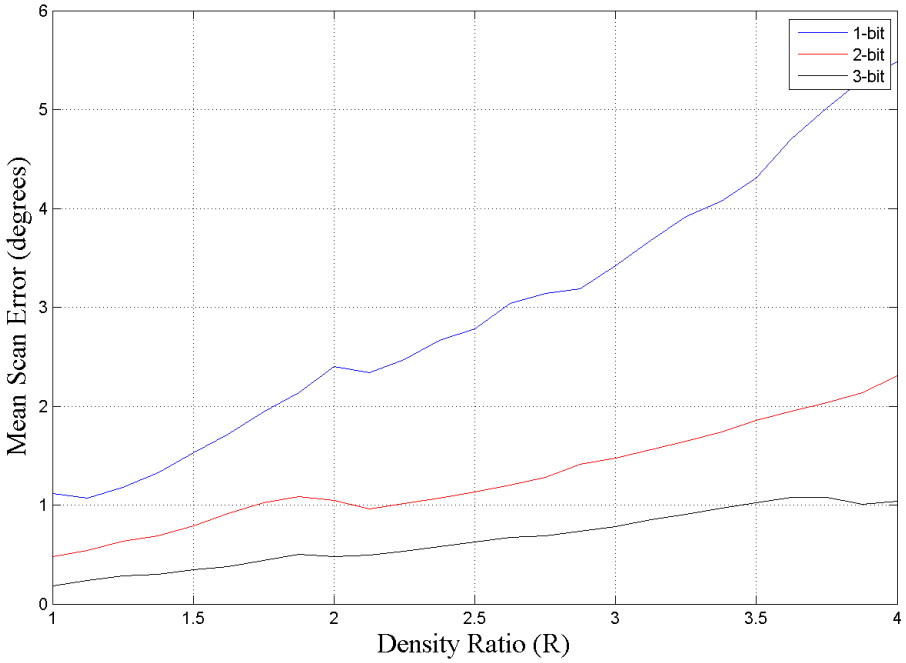

Figure 3.24: Mean scan error in degrees for a planar array, as a function R and B

The scan error at each scan angle was determined by calculating the dot product between the two vectors describing the maximum points, $\mathbf{r}_\mathrm{q}$ and $\mathbf{r}_\mathrm{i}$, of $f_\mathrm{Q}(\theta, \phi)$ and $f_\mathrm{I}(\theta, \phi)$ respectively:

$$\mathbf{r}_\mathrm{i} \cdot \mathbf{r}_\mathrm{q} = r^2 \left(\cos\theta_\mathrm{i} \cos\theta_\mathrm{q} + \sin\theta_\mathrm{i} \sin\theta_\mathrm{q} \cos\left(\phi_\mathrm{i} - \phi_\mathrm{q}\right)\right) = r^2 \cos\psi, \tag{3.43}$$

where ψ is the angle between the two vectors, defining the scan error.

The scan errors are now a function of both θ and ϕ and as a result it is expected that a higher mean scan error will be observed when compared to the scan accuracy of a linear array which is only a function of θ.

The *edge scanning effect* is present for the planar array as well, which explains the increase in mean scan error as function of density ratio. As explained above, the error is now a function of θ and ϕ which means that any error observed in either dimension will be amplified with the flattening of the main lobe.

3.4.2 Overall Beam Pattern Performance

To evaluate the beam pattern noise distribution, the SQNR of the array is investigated. The SQNR definition used for a linear array in Equation 3.31 is adapted for a planar array by adding the ϕ-dimension as follows:

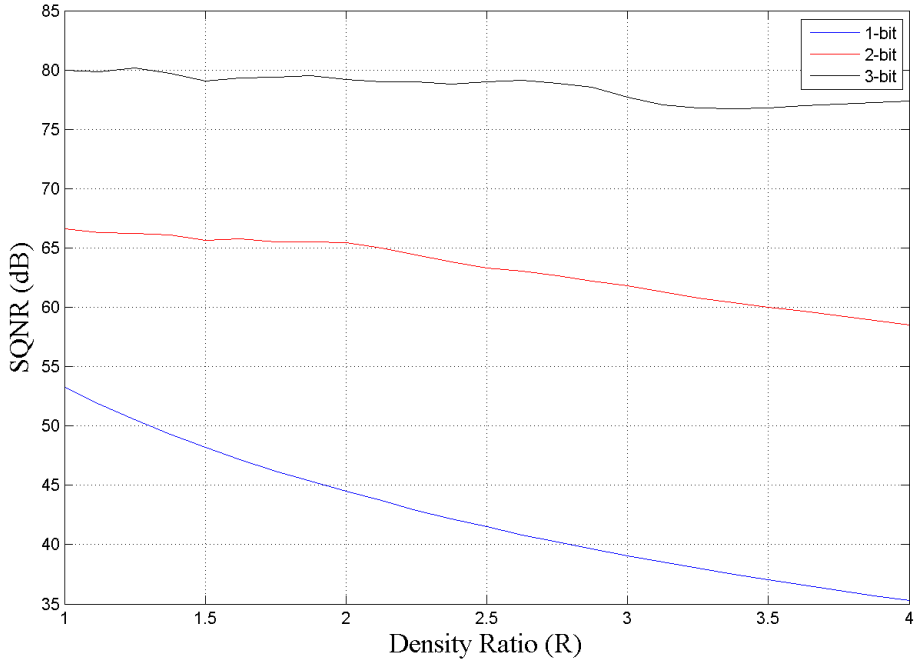

Figure 3.25: SQNR for a planar array as a function of R and B

$$\text{SQNR} = \frac{|f_{\text{I}}(\theta_0, \phi_0)|^2}{E\left[f_{\text{noise}}(\theta, \phi)^2\right]}, \tag{3.44}$$

where $|f_{\text{I}}(\theta_0, \phi_0)|$ for a N×N rectangular array is simply equal to N^2. The mean squared error term in the denominator is calculated for the full scan range in the visible region. The SQNR as a function of R and B is shown in Figure 3.25

In Section 3.3.3 it was observed that a linear array with a constant number of elements observes little to no increase in SQNR as a function of R. This was explained to be because of the beamwidth increasing as a function of R which also widens any observed beam pattern noise and effectively increase the mean error.

The beamwidth of a planar array was defined in Equations 3.41 and 3.42. From these it can be seen that for a N×N planar array, the beamwidths will scale quadratically with an increase in R. This is because the beamwidths of the separate broadside arrays defined in the x and y dimensions as Θ_x and Θ_y, are equal (now both defined as Θ_x), and therefore Equations 3.41 and 3.42 becomes:

$$\Theta = \frac{\Theta_{x^2}}{\sqrt{\cos^2\theta_0\left[\cos^2\phi_0 + \sin^2\phi_0\right]}}, \tag{3.45}$$

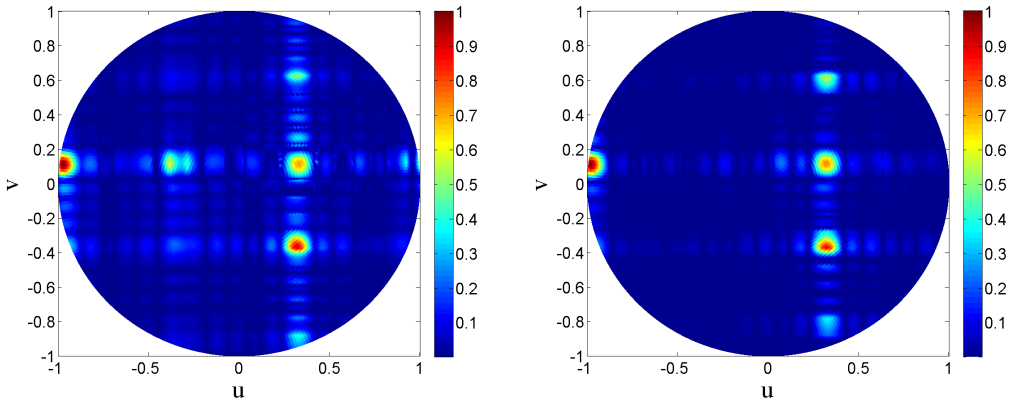

(a) (b)

Figure 3.26: Normalized error patterns of a variable number of elements planar array scanned to ($\theta_0 = 20°, \phi_0 = 20°$), for R=1 (a) and R=4 (b)

$$\Psi = \frac{\Theta_x^2}{\sqrt{\sin^2\phi_0 + \cos^2\phi_0}}. \tag{3.46}$$

Therefore, the area of any pattern noise will scale quadratically as R is increased.

To illustrate, the pattern error for a scanning planar array, as a function of θ and ϕ, is shown in Figure 3.26 for $R = 1$ and $R = 4$. In this specific example, the number of elements is determined according to $N = M = 20R$ to retain the beam pattern by eliminating the beam broadening effect as a function of R.

Noise is minimized with an increase in R; however, primary noise in the form of quantization lobes is still present as expected due to its singular dependence on scan angle. In an array with a constant number of elements, these lobes become wider with an increase in R, resulting in a higher noise contribution and effectively cancelling the SQNR gained from the "shaping" of secondary noise. This is further illustrated in Figure 3.27. Note that the array factor is a function of u,v space, calculated as follows:

$$u = \sin\theta\cos\phi \tag{3.47}$$

$$v = \sin\theta\sin\phi, \tag{3.48}$$

for $\theta \in (-90^{\circ}, 90°)$ and $\phi \in (0°, 180°)$.

This further explains why the SQNR generally decreases as a function of R. The one-bit case reduces at an increased rate compared to the two- and three-bit cases. This is because of the dominant noise contribution from the second main lobe which also broadens as a function of R.

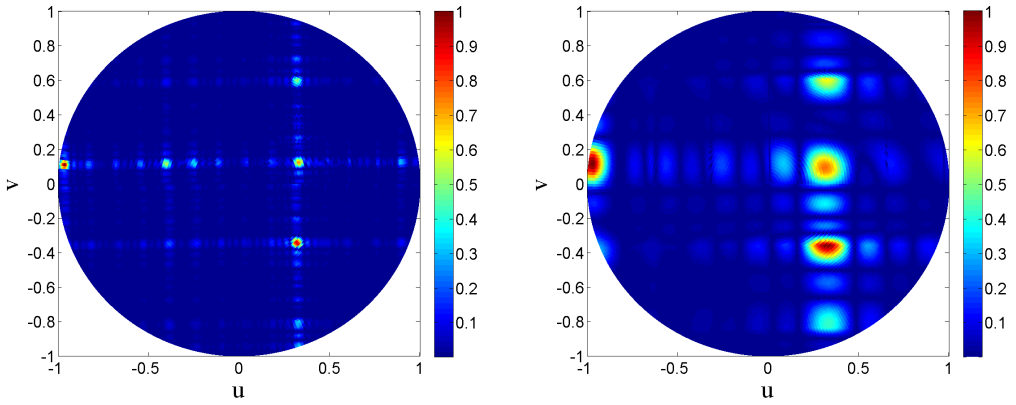

(a) (b)

Figure 3.27: Normalized error patterns of a constant number of elements planar array scanned to ($\theta_0 = 20°, \phi_0 = 20°$), for R=1 (a) and R=4 (b)

3.5 Conclusion

In this Chapter, the effects of phase quantization were established based on forced excitation mode. This was done by calculating beam patterns using the array factor. Important beamforming performance metrics were identified based on the general requirements of phased antenna arrays in radio astronomy.

The investigation started with a study on a simple beamforming model that was used to show the importance of proper phase control. In this beamforming model, the performance metrics were calculated analytically by initially deriving an inequality expression that limits the scan range in the visible region to real space. With this beamforming implementation, it was determined that the scan accuracy and scan range is extremely limited for low phase resolutions and that a very high phase resolution will be required to achieve any consistent practical performance.

The second beamforming model that was evaluated used discrete phase control whereby the quantized phase shift at each element is calculated to be the closest to the required ideal phase shift. This beamforming method required that the performance metrics be determined numerically by simulation. To determine the scan accuracy realistically, the scan range had to be limited to ensure that the main lobe is sufficiently defined for all the considered scan angles. The maximum scan errors in the scan range were determined after which it was shown that they occur at off-broadside scan angles mostly beyond 60°. The reason for this occurrence was discussed and supporting examples were shown. The scan limitations as a result of mutual coupling in practical arrays were used to explain the significance of these angular positions at which the maximum scan errors occur. It was further shown that the mean scan error is well below 1° for all phase resolutions under consideration, which went on to show that the maximum errors are for very specific scan angles.

The side lobe level performance was characterised by first determining the amplitude extents of quantization lobes as a function of density ratio, scan angle and phase resolution. This was done by identifying quantization lobes with relative amplitude significance in the scan range, as a function of the density ratio and the total number of bits. Amplitude significance was defined to be any amplitude higher than the FSL. This study provided significant insight into the overall behaviour of quantization lobes and its relationship with the array parameters. This further led to the identification of two different components that contribute the total beam pattern noise. These were classified as primary and secondary beam pattern noise contributions based on their relative contribution and their different dependency on the array parameters.

An overall beam pattern noise performance evaluation was conducted where the performance was quantified using the SQNR. The insight obtained in the quantization lobe study regarding primary and secondary beam pattern noise was used to explain the results. It was seen that the overall pattern noise decreases non-linearly with an increase in phase resolution. This also confirmed the main lobe amplitude loss study where it was observed that the loss percentage decreases exponentially as a function of bits.

These studies were extended to a planar array with the same discrete phase control. It was shown that the planar array factor could be expressed as the product of two linear array factors which gave insight into the expected beamforming performance. The results differed from those obtained in the linear array study, as was expected; however, the insight obtained in the linear array study was used to explain these results where it was applicable.

In summary, this Chapter provided a methodology by which the basic beamforming performance of an array can be determined using a forced excitation model. Chapter 4 will serve as a demonstration of a free excitation model implementation of these performance models.

Chapter 4

Quantized Beamforming: Free Excitation Analyses

4.1 Introduction

As part of this project, a Dense Dipole Array (DDA) was built with a couple of goals in mind. The first goal is to obtain measurements that can be used to complete a demonstration of the beamforming performance study methodology presented in this thesis. An investigation on the basic structural design of the DDA was additionally conducted to identify possible simplifications with the intention of simplifying the construction process.

The Chapter will start with a general background and design discussion of the DDA which will be followed by a description of the construction and measurement process that was involved. The measurements will then be compared to simulation results to confirm that the array works as intended. It will also be compared with results obtained on the first prototype to confirm consistency.

A description will be provided of the implementation of mutual coupling in the performance models derived in the previous Chapter. Scan accuracy and side lobe level results will be obtained and discussed. Certain observations will be explained, where applicable, by referring to the results obtained in Chapter 3.

4.2 Dense Dipole Array Background

The idea of using a dipole aperture for the purposes of radio astronomy was originally conceived in a 1994 technical report authored by J.E Noordam and J.E.E Voûte [34]. With a single dipole being inherently narrow-bandwidth, it was suggested in the report that multi-purpose switches be used to connect the dipoles so that the combined bandwidth can be increased by connecting them in either in an open-circuit, short-circuit, capacitance or inductance. Finding

suitable switches proved to be a challenge and therefore a different approach was required.

By using an equivalent circuit model of an infinite dipole array backed by a ground plane, which was originally developed by Munk [27]), it was shown that the infinite current sheet array introduced by Wheeler [35] can be achieved by compensating for the inductance caused by the ground plane by inserting capacitances between the tip of neighbouring dipole elements. Instead of placing physical capacitors between the tips, it was suggested by Gilmore [20] that careful placement of the elements can provide the necessary capacitance. Gilmore went on to design a Dual-Polarized Dense Dipole Array prototype which is an implementation of the concepts discussed above.

As described in [20], the initial design process was based on an infinite array. This made it possible to use the inherent mutual coupling as a way of impedance stabilisation to achieve a wide frequency bandwidth. The inductance caused by the ground plane and the inductance caused by the elements themselves are cancelled by the capacitance between the tips of neighbouring elements. A parameter study was performed to determine the best possible antenna dimensions and placement to achieve these effects optimally. This was done by observing the bandwidth in the active reflection coefficient as a function of these parameters.

Certain design challenges were encountered. It was found that problems in the optimisation strategy resulted in the bandwidth of a single polarised DDA being higher than that of a dual-polarized one. Another problem in the design of a connected dense antenna array is that common-mode current paths are created resulting in common-mode resonances. This was solved by designing a wide-band common-mode filter and placing it between each antenna and connector.

The antenna elements are connected together in pairs to form differential elements. This was done to reduce the number of required ports and therefore cost. A measurement challenge is introduced by this which will be discussed in Section 4.4.

4.3 Building a Second DDA Prototype

One of the motivations for using aperture array technology for SKA is the ease of mass production that can be achieved. It is, therefore, worthwhile to investigate ways in which the basic structure of the DDA prototype can be optimised. The basic structure of the DDA will be discussed first.

The dipoles of the DDA are printed onto 16 separate FR4 substrate tiles where each polarisation is located on a separate side. These tiles are then placed 75 cm above an aluminium ground plane with support provided by plastic rods, The ground plane also serves as the backbone of the structure. Further structural integrity is provided by joining the separate tiles using per-

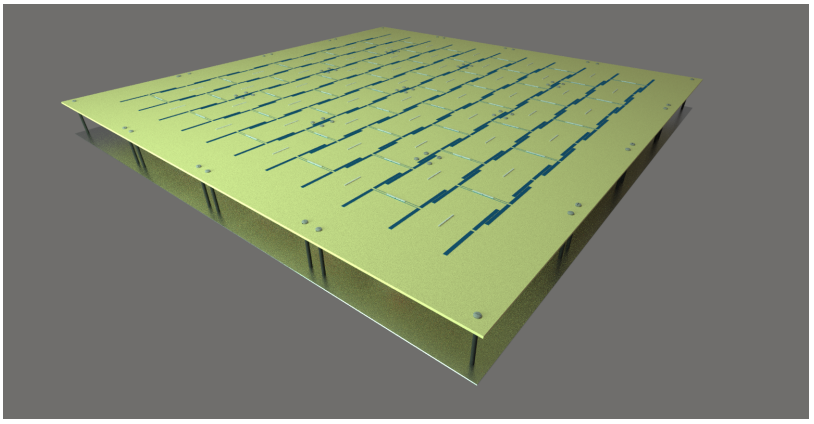

Figure 4.1: DDA top-view

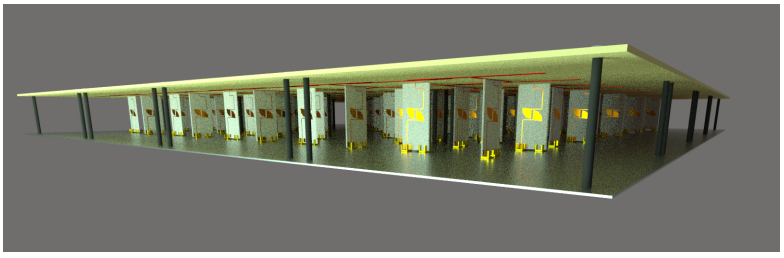

Figure 4.2: DDA side-view

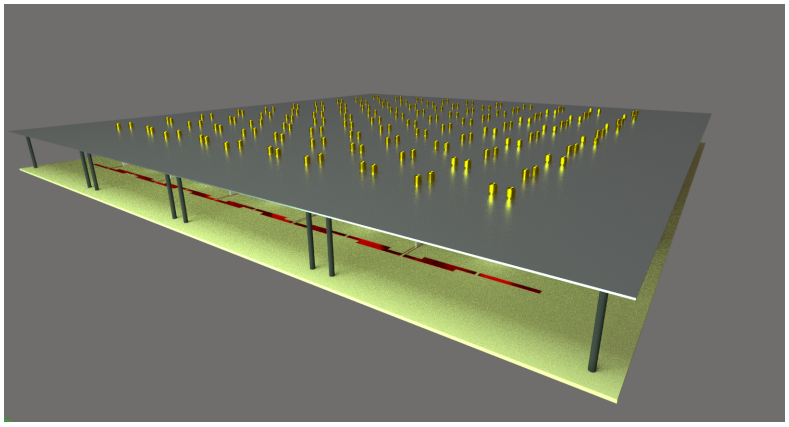

Figure 4.3: DDA bottom-view

spex plates at each collocated corner. The element feed boards containing the common-mode filter as described in the previous Section, are placed between the ground plane and the PCB tiles. The connectors, which are soldered to the feed boards, protrudes through drilled holes in the ground plane.

Computer rendered images of the DDA are shown in Figures 4.1, 4.2 and 4.3.

With the original PCB layout producing 16 unique tiles, it was found that

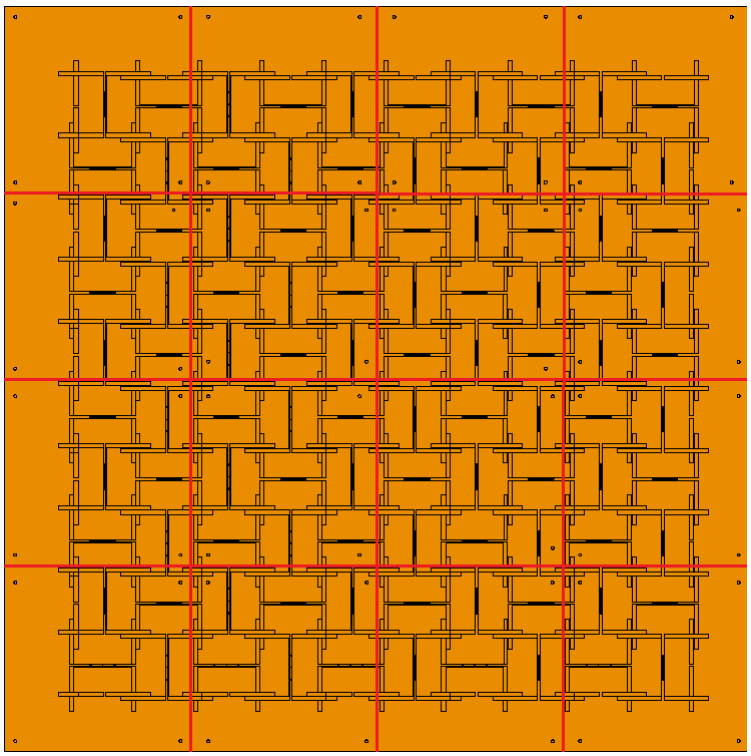

Figure 4.4: Old PCB layout per tile

by changing the layout slightly, this number can be reduced to 8 unique tiles. The original PCB layout per tile is shown in Figure 4.4, and the proposed improved layout is shown in Figure 4.5. Both polarisations are shown for clarity.

When joining the tiles, the discontinuities in the printed dipoles and their feed lines need to be soldered. This a fragile solution in the sense that any slight deformation in the structure can break these joints by tearing the printed tracks from the substrate. This can possibly be solved by using castellated joints at all the discontinuities. A computer rendered dipole castellated joint is shown in Figure 4.6. The implementation of this was found to be out of scope as the manufacturing and time costs exceeded the budget constraints for the project.

The second prototype was built with the implementation of the new PCB layout. The PCBs were manufactured by ASTRON in the Netherlands.

With the original array only having its central elements fed, the purpose of a second prototype was to have more elements connected in order to acquire a better representation of the actual array performance.

Ideally all the elements would be connected to be able to have a fully measured sample of the DDA coupling parameters, however, this again exceeded the budget constraints and therefore a compromise was necessary. It was decided to connect two full quarters in one polarisation as indicated in Figure 4.7.

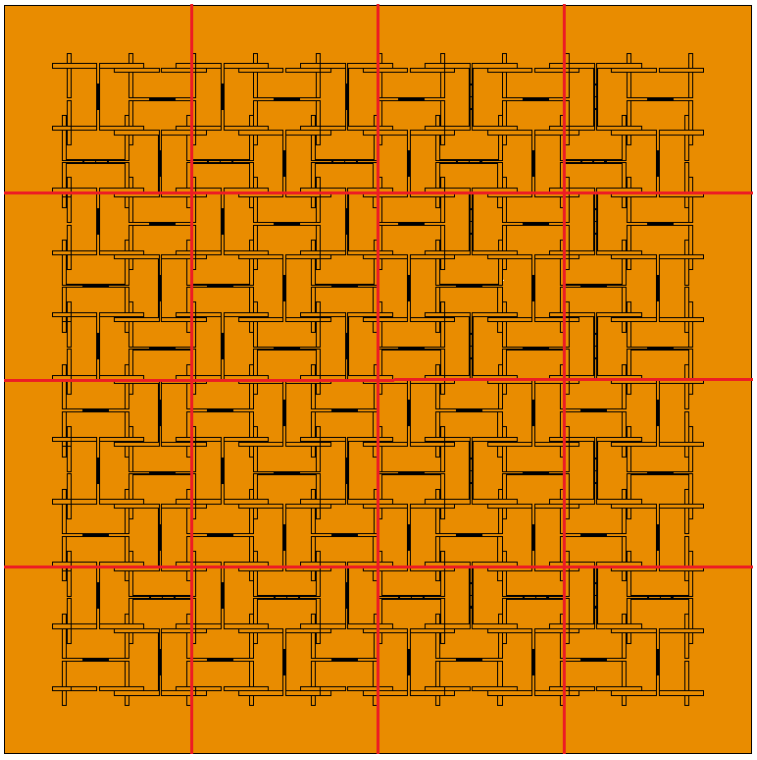

Figure 4.5: New PCB layout per tile

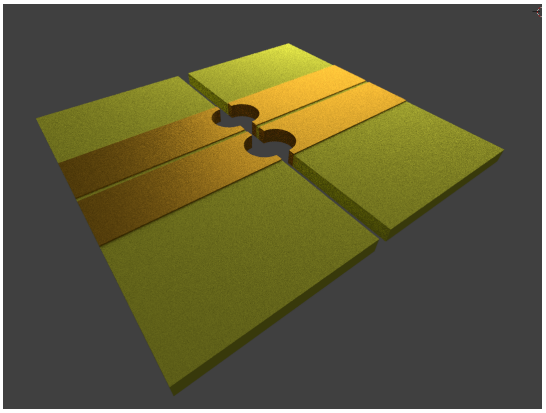

Figure 4.6: Dipole castellation joint

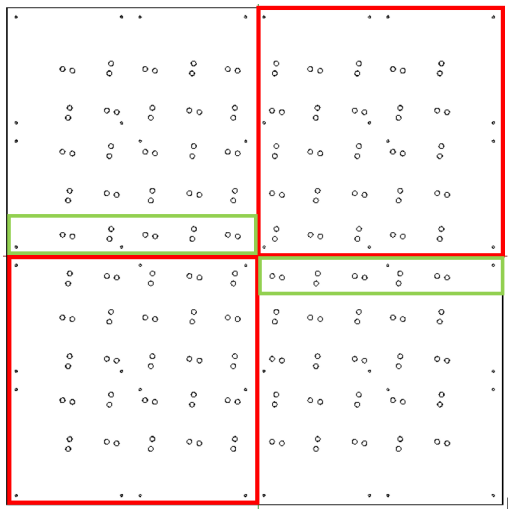

Figure 4.7: DDA second protype connected quarters

The Green boxes indicate additional ports that were connected for the purpose of gain pattern measurements which will be discussed in a later Section.

The ground plane is shown to visualise the number of ports that will be a result of this decision. The decision to connect only one polarisation was based on the results obtained by Gilmore where it was shown that there is good isolation between the two polarisations. The measurement procedure is discussed in the following Section.

4.4 Measurement Procedure

The antenna elements are connected in a differential manner. This presents a measurement challenge as the available measurement equipment do not provide the required functionality to measure these values. It is therefore required that the single-ended S-parameters be measured after which they will be converted to mixed-mode S-parameters manually. The measurement procedure that was used is based on the procedure described in [36].

With the decided two-quarter connection layout, including additional ports, 60 single ended ports have to be measured. The array now consists of more ports than what is available on the measurement equipment and therefore multiple measurements are made to fill the full 60×60 single ended S-parameter matrix. This is done by ensuring that each pair of single-ended ports is measured at least once. The unmeasured ports and antenna elements are terminated in matched loads.

The 60×60 single ended S-Matrix represents only half of the one polarisation under consideration. With symmetry confirmed by comparing single-ended measurements with their symmetrical partners, it was possible to fill the rest of the required single-ended S-Matrix values using a "copy-paste"

procedure.

The measurement plane is now shifted to exclude the SMA connectors. This is done by renormalizing from the characteristic impedance of the measurement equipment, which is 50Ω, to 75Ω, which corresponds to a differential characteristic impedance of 150Ω.

A two-port differential system is considered to demonstrate the method used to convert the single ended measurements to mixed mode parameters. Each differential port, denoted by m and n, consists of two single-ended ports denoted by p and q. The mixed-mode S-parameter matrix of the system is given as [20]:

$$\mathbf{S}_{\mathrm{MM}} = \begin{bmatrix} \mathbf{S}_{\mathrm{diff\ diff}} & \mathbf{S}_{\mathrm{diff\ comm}} \\ \mathbf{S}_{\mathrm{comm\ diff}} & \mathbf{S}_{\mathrm{comm\ comm}} \end{bmatrix} \tag{4.1}$$

where each element is a submatrix that can be calculated as:

$$S_{\mathrm{diff\ diff,\ mn}} = \frac{S_{\mathrm{pp,mn}} - S_{\mathrm{pq,mn}} - S_{\mathrm{qp,mn}} + S_{\mathrm{qq,\ mn}}}{2} \tag{4.2}$$

$$S_{\mathrm{diff\ comm,\ mn}} = \frac{S_{\mathrm{pp,mn}} + S_{\mathrm{pq,mn}} - S_{\mathrm{qp,mn}} - S_{\mathrm{qq,\ mn}}}{2} \tag{4.3}$$

$$S_{\mathrm{comm\ diff,\ mn}} = \frac{S_{\mathrm{pp,mn}} - S_{\mathrm{pq,mn}} + S_{\mathrm{qp,\ mn}} - S_{\mathrm{qq,\ mn}}}{2} \tag{4.4}$$

$$S_{\mathrm{comm\ comm,\ mn}} = \frac{S_{\mathrm{pp,mn}} - S_{\mathrm{pq,mn}} + S_{\mathrm{qp,mn}} - S_{\mathrm{qq,mn}}}{2}. \tag{4.5}$$

For the purpose of this study, only the differential mode will be considered. The common-mode characteristics of the DDA is discussed in detail by Gilmore in [20].

4.5 Measurement Results

In addition to the measurements, a finite array simulation was performed in FEKO using an infinite substrate and ground plane approximation. The FEKO CAD model is shown in Figure 4.8. The single-ended S-parameter results of the simulation are converted to mixed-mode S-parameters using the method described in Section 4.4.

The mixed-mode S-parameters of the measurements and simulation are then used to calculate the mixed mode active reflection coefficient Γ_{m} for a specific scan direction for each antenna element as follows:

$$\Gamma_{\mathrm{dd,m}}(\theta_0, \phi_0) = \sum_{n=1}^{N} S_{\mathrm{diff,diff,mn}} e^{-jk(x_n \sin\theta_0 \cos\phi_0 + y_n \sin\theta_0 \sin\phi_0)}. \tag{4.6}$$

The active reflection coefficient (Γ_{dd}) at broadside for a central and corner element in the array are shown in Figures 4.9 and 4.10 respectively.

It is seen that the results for a central element differ from the simulation result. This might be attributed to inaccuracies in the simulation as well as construction tolerances. The same can be said of the results for a corner element. It is, however, noted that there is a good correspondence in the $\Gamma < -5$ dB bandwidth between simulated and measured values. In addition to that, the results for the central element also corresponds well with those obtained by Gilmore [20]. The edge elements were not connected in the first prototype.

It is seen that a corner element, counter-intuitively, has more $\Gamma < -5$ dB bandwidth than a central element. In fact, it has a $\Gamma < -10$ dB bandwidth that is in accordance with the original specifications set out for MFAA. Investigating this observation is out of the scope of this project and will be allocated to future work.

The single ended gain patterns of a central element were measured. They were then converted to differential-mode patterns using the method described in [37]. For two single-ended ports, this method summarises to:

$$\vec{G_{\mathrm{dd}}} = \frac{1}{\sqrt{2}}\left[\vec{G}_1(\theta,\phi) - \vec{G}_2(\theta,\phi)\right], \tag{4.7}$$

where $\vec{G}_1(\theta,\phi)$ and $\vec{G}_2(\theta,\phi)$ represents the gain pattern vectors of each single-ended port that make up a differential port. Only the co-polar gain pattern is considered.

The normalized embedded element gain pattern (EEP) in the E- and H-planes at three frequency points are shown in Figures 4.11 and 4.12 respectively.

The differential mode gain pattern corresponds well with the results obtained by Gilmore, which goes on to confirm relative consistency between the two prototypes. Additionally, as said in [20], the flatness of these patterns are comparable with the patterns of other MFAA prototypes [20; 19].

4.6 Quantized Beamforming with Mutual Coupling

The performance models derived in Chapter 3 were purely based on isotropic elements with no mutual coupling and were therefore referred to as *forced excitation* models. This implied that direct voltage or current control is available at the terminals of the antennas. In reality, this is not the case and antenna elements in close proximity will experience mutual coupling as discussed in Section 2.4.5. Since the antenna spacing that is used in the performance mod-

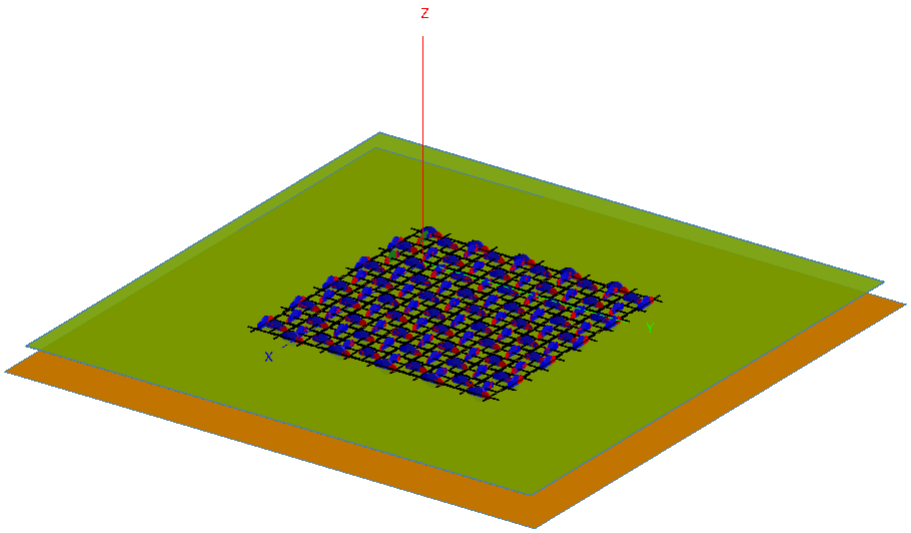

Figure 4.8: FEKO DDA simulation model

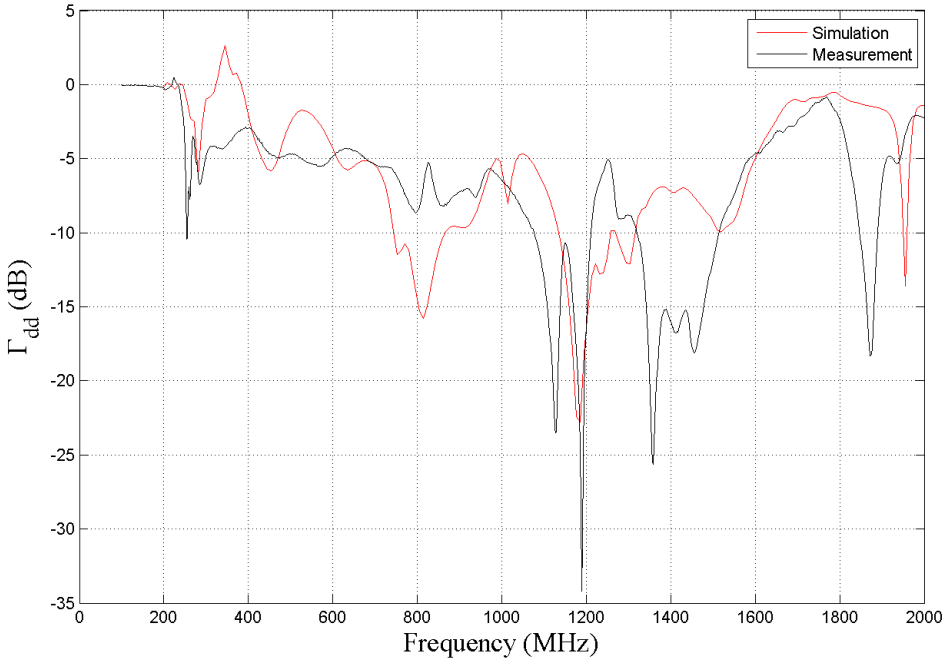

Figure 4.9: Active reflection coefficient at broadside for a central element in the array

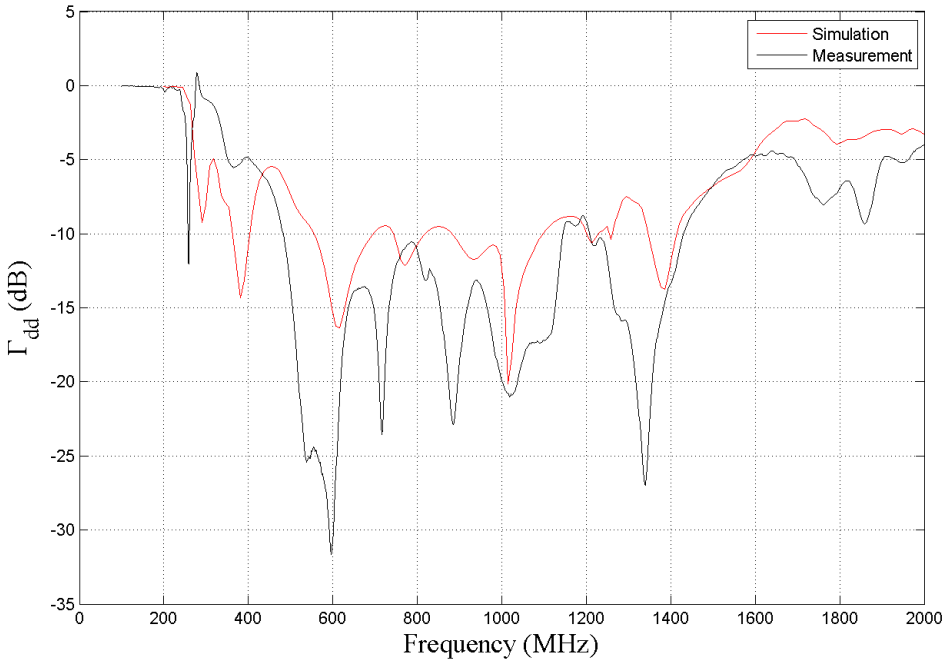

Figure 4.10: Active reflection coefficient at broadside for a corner element in the array

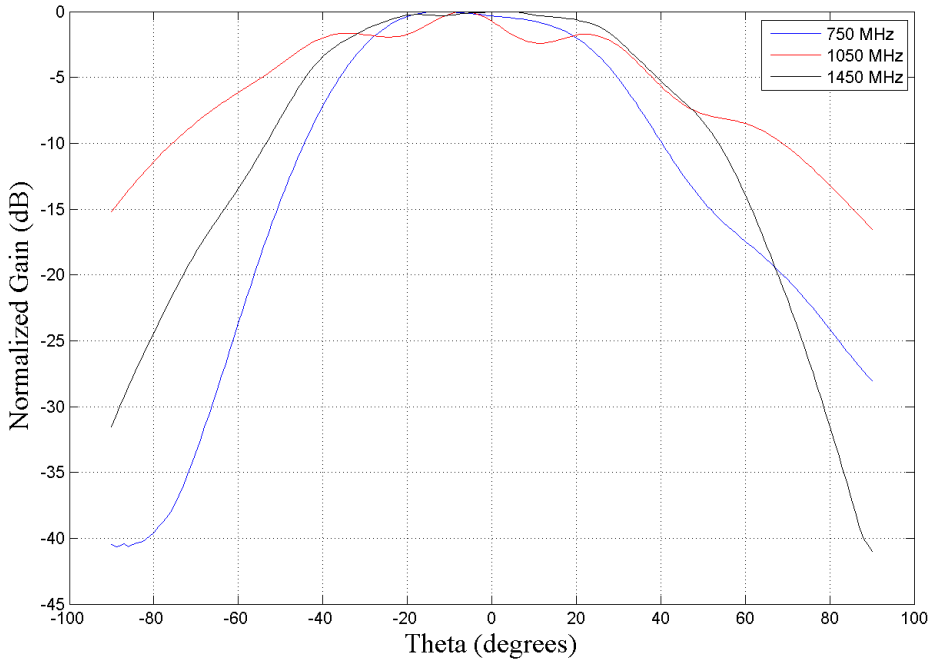

Figure 4.11: Normalized co-polar E-plane gain pattern for an embedded element

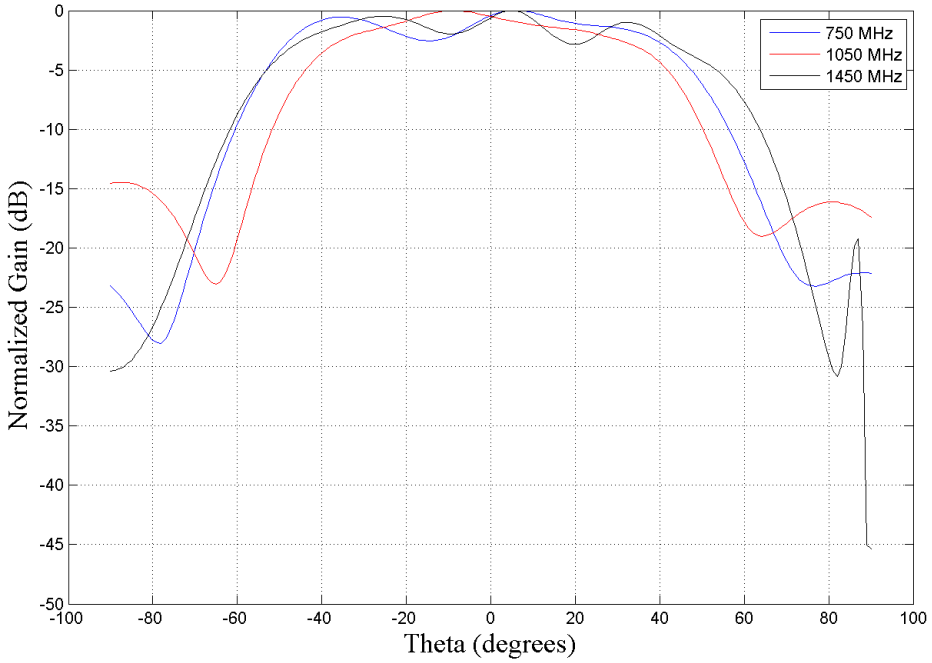

Figure 4.12: Normalized co-polar H-plane gain pattern for an embedded element

els is defined to be equal to or less than $\lambda/2$, strong mutual coupling effects are expected.

The performance models will now be based on a free excitation model where measurements from a DDA prototype tile will be used as a basis for the study. With this said, the study will be based on a planar array with a layout based on a DDA tile.

The measurements that are available are limited to a single tile. The extension of these parameters to a larger model and the limitations involved will be discussed first. This will be followed by the pointing accuracy and side lobe level performance results, and a discussion thereof.

4.6.1 Simulation Set-Up

Measuring the gain pattern of an embedded element pattern proved to be a challenge given the limitations of the measurement equipment and the physical size of the tile. The measurement equipment provides full spherical capabilities; however, this would require that the tile, in the mounted position as shown in Figure 4.13, would have to be fully rotated in the vertical plane. This was not possible and therefore it was decided to measure the patterns only in the E- and H-planes by rotating manually as required, as these would give sufficient detail about the beams in the principal planes of the array.

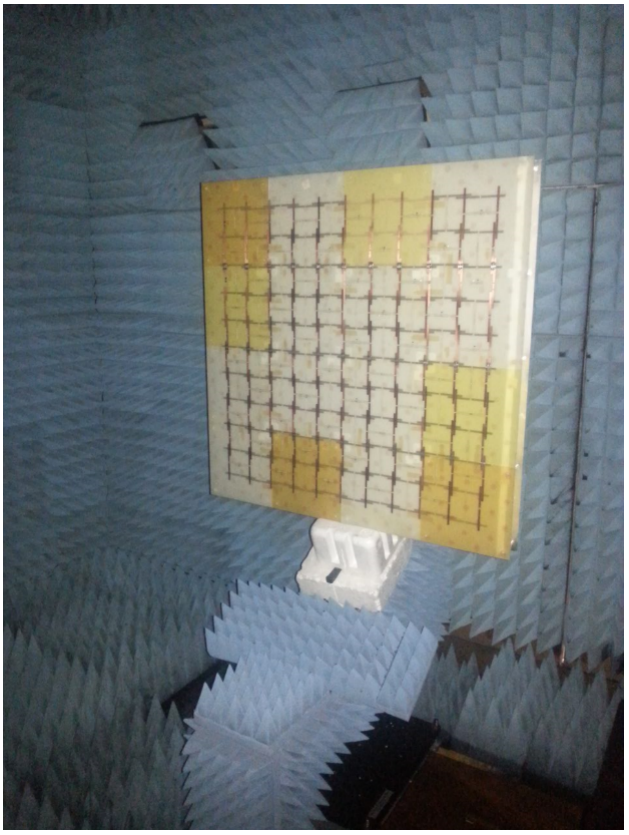

Figure 4.13: DDA mounted on pedestal in anechoic chamber

It was explained in Section 2.4.5 that mutual coupling can be accounted for in the total beam pattern by either using the active coupling coefficients and an isolated antenna element pattern or by using an EEP which on its own accounts for mutual coupling. The scanned array pattern can then be found by taking the product of the array factor and either of these.

Since both the embedded element pattern and the S-parameters were measured, either method can be implemented on tile level. However, for the purpose of the study, it was desired to have a larger array for a more realistic implementation. The measured S-parameters can be extended to a larger array by making certain assumptions about the edge-effects; however, this method could be prone to errors and no redundant error checking method is available.

A larger finite array can be simulated to confirm the S-parameter extension, but this would also require a great amount of simulation time. With simulation inaccuracies observed on tile level alone, it was decided not to implement this method.

It was also explained in Section 2.4.5 that a central EEP in an infinite array is a good average of the total pattern of the array. By investigating the coupling behaviour of a central element on a DDA tile, it can be shown that a central EEP is a good approximation of the EEP of a larger array.

Before the coupling of a central element is investigated, a description of the DDA tile orientation in space, and its layout is necessary. The DDA element layout in a single polarisation is shown in Figure 4.17, also indicating its orientation in space. The E-plane is located on the x-axis and the H-plane is located on the y-axis. Furthermore, the x-axis is in the $\phi = 0°$ plane and the y-axis is in the $\phi = 90°$ plane, which also relates the principal planes with the E- and H-planes.

The S-parameter coupling between a central element and its nearest neighbour is shown in Figure 4.14, followed by the S-parameter coupling to an edge element.

It is seen that the coupling from a central element to an edge element is mostly below -30 dB. This goes on to show that the most significant inter-element coupling of a central element is provided by its nearest neighbours and that when placed in a larger array, the active reflection coefficient should not be significantly affected. This also confirms the hypothesis that the embedded element pattern of a central element is a good representation of the average pattern of a larger array.

The beamwidth of the beam pattern decreases as the aperture size increases. For simulation purposes, this would require that the angular resolution is increased to ensure a well-defined beam pattern. The angular resolution of the pattern measurements is limited to 1°, which limits the maximum angular resolution of a simulation and therefore also the size of the aperture.

It was found that the largest planar array that can be used while maintaining sufficient angular resolution, is a 20×20 element array. This corresponds to 4 DDA tiles placed together to form a square aperture.

4.6.2 Pointing Accuracy Results

This Section investigates the scan accuracy of a planar array with mutual coupling. A 20×20 element planar array is used which is an extension of the DDA layout as shown in Figure 4.17.

The investigation will be performed in the principal planes of the array due to the limitations in the measurements as discussed in the previous Section. Scanning will therefore be limited to the $\phi = 0°$ and $\phi = 90°$ planes.

Scanning past the HPBW of an EEP results in serious beam deformation, such that the side lobes become higher than the main lobe. Scanning will, therefore, be limited to the HPBW of each EEP under consideration.

The EEP are shown for three frequency points in Figures 4.11 and 4.12, corresponding to the E- and H-plane patterns respectively. These are the gain patterns that will be used in the study.

The beams and their properties, such as equivalent density ratio and HPBW, are summarised in Table 4.1.

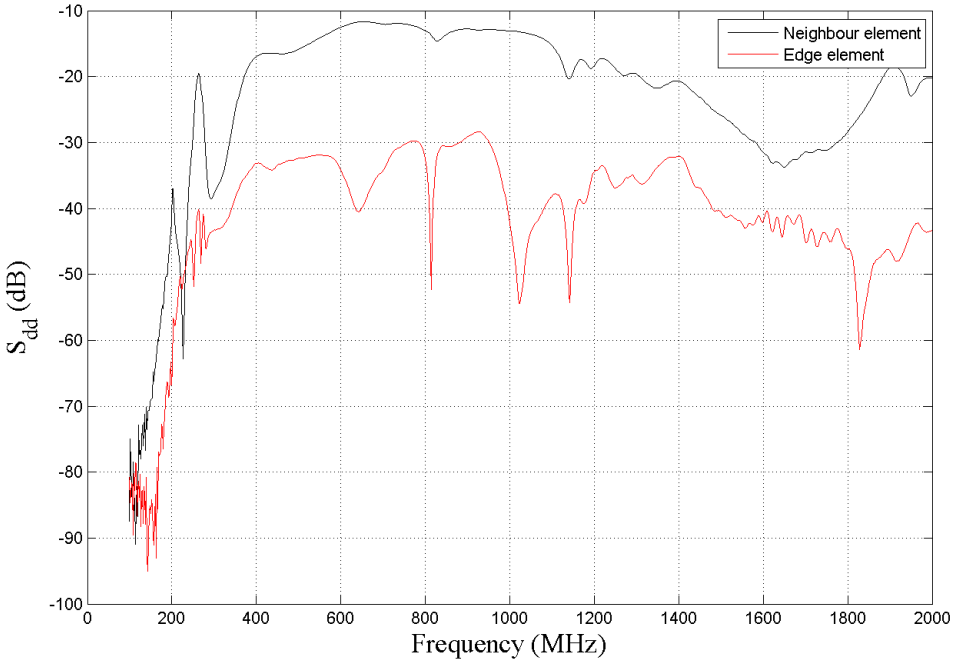

Figure 4.14: S-parameter coupling of a central element

Before the results are discussed, it should be mentioned that due to the fact that the angular resolution is limited to 1°, the scan error at any given scan angle (θ_0) is limited to values of $1n$, where n is an integer.

The mean scan error for the $\phi = 0°$ and $\phi = 90°$ planes, as a function of B and R, are shown in Figures 4.15 and 4.16 respectively.

The gain patterns are not uniform and it is expected that this will have an impact on the scan accuracy. Additionally, it is expected that the half-power edges of the EEP's will have the largest impact on the scan accuracy. This is because the main beam experiences a significant deformation at these points, effectively shifting the maximum point. It is also expected that this observation will increase as the beamwidth increases, and therefore an increase in mean error is observed with an increase in R, for all B values.

It is also noticed that scanning in both planes produces similar performance and behaviour. This is expected since, apart from their beamwidths, there is no significant difference in the beam patterns of both planes.

4.6.3 Discussion

It is explained that the EEP's will have a noticeable impact on the scan accuracy, however, with three distinct patterns involved, it is observed that an increase in bits nevertheless dominates the performance. This is a significant

Beam	Frequency (f)	Density Ratio (R)	HPBW (E/H-Plane)
1	750 MHz	2.2	E: 56°, H: 90°
2	1050 MHz	1.6	E: 76°, H: 72°
3	1450 MHz	1.15	E: 71°, H: 90°

Table 4.1: Property summary of measured EEP's

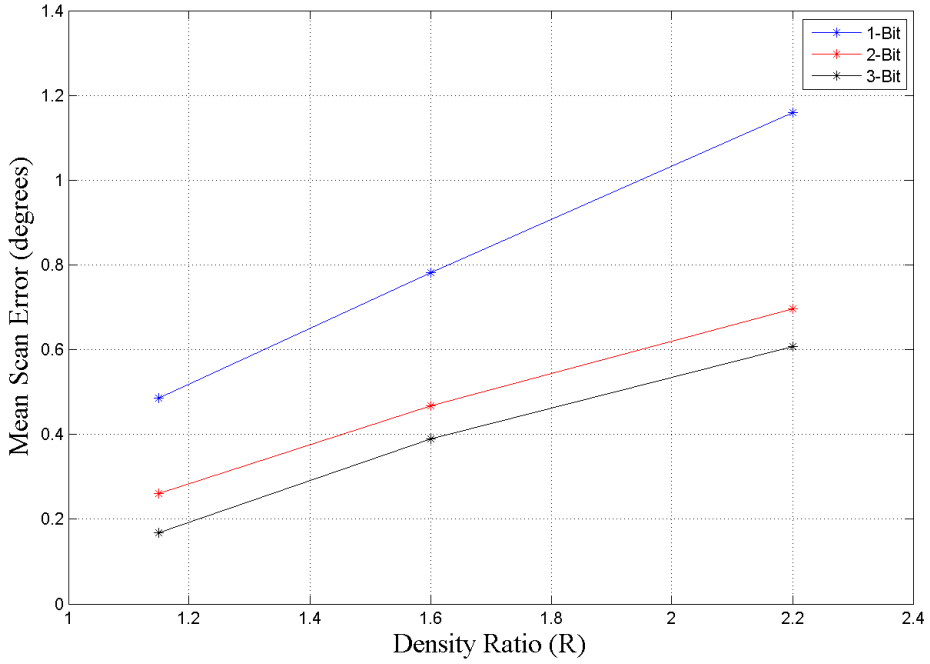

Figure 4.15: Mean scan error as a function of R and B, in the $\phi = 0°$ (E)plane

observation, because direct control is available on the number of bits, while no direct control is available over the EEP's.

Further, it is noticed that the mean error is relatively low and rarely exceeds 1°. An increase in aperture size and angular resolution of the simulation is expected to lower the mean error even further. This can be explained by the fact that a lower beamwidth will be able to "sample" the EEP with more accuracy, or less deformation.

4.6.4 Pattern Noise Results

This Section investigates the beam pattern noise due to phase quantization by performing the same method used in Section 3.4.2. The scan range is however now limited to the HPBW of each beam.

The SQNR as a function of R and B for the $\phi = 0°$ and $\phi = 90°$ planes

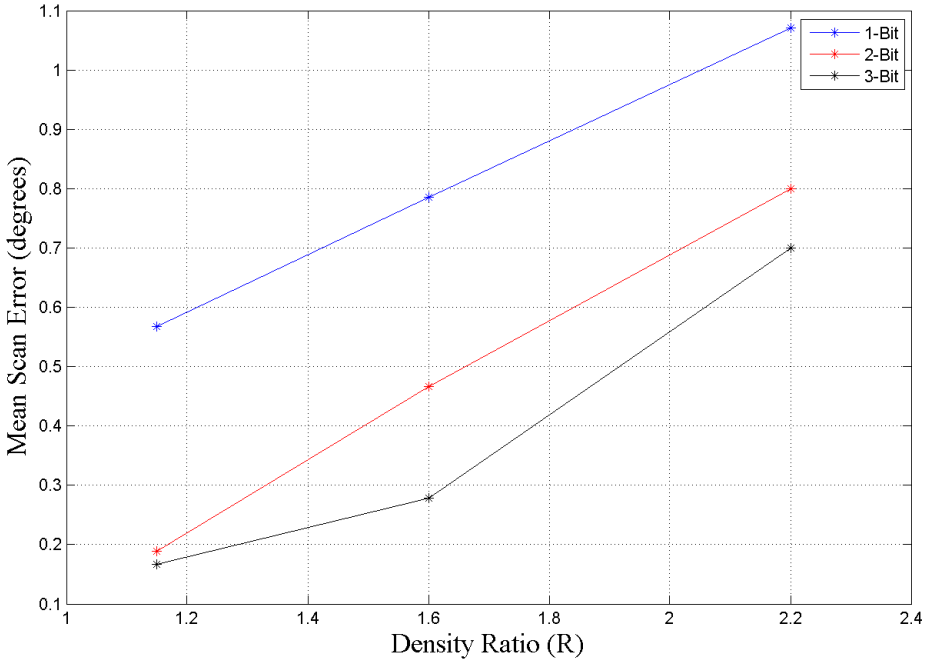

Figure 4.16: Mean scan error as a function of R and B, in the $\phi = 90°$ (H)plane

are shown in Figures 4.18 and 4.19 respectively.

It is expected that the behaviour of the SQNR as a function of R will differ between the two planes due to differences in the EEP's. Nevertheless, it is noticed that both planes produce similar ranges of SQNR values for each value of B.

The noise will be amplified relative to the main lobe when scanning towards the half-power edges of each pattern. This can be explained by the main lobe being attenuated as a function of the product between the array factor and the EEP, and at the same instance, the relative side lobe level is amplified, including any pattern noise. With the main lobe maximum attenuation being -3 dB and the side lobes being multiplied by as much as 0 dB, it is expected that these effects can be significant and result in a decrease in the SQNR, especially when coupled with beam broadening.

As was explained in Section 3.3.2, the pattern noise consists of primary and secondary noise. It was found that the angular position of first-order noise (quantization lobes), as shown in Figure 3.15 for the 2-bit case, is a function of θ_0. The number of elements used to generate those results was 100, which is 10 times more than what was used in the current study; however, first-order noise is a result of periodic phase errors and is independent on N. The results as shown in Figure 3.15 can, therefore, be applied to the current study as well.

When scanning towards 90° from broadside, it was observed that the angular position of a significant quantization lobe in the 2-bit case moves as a

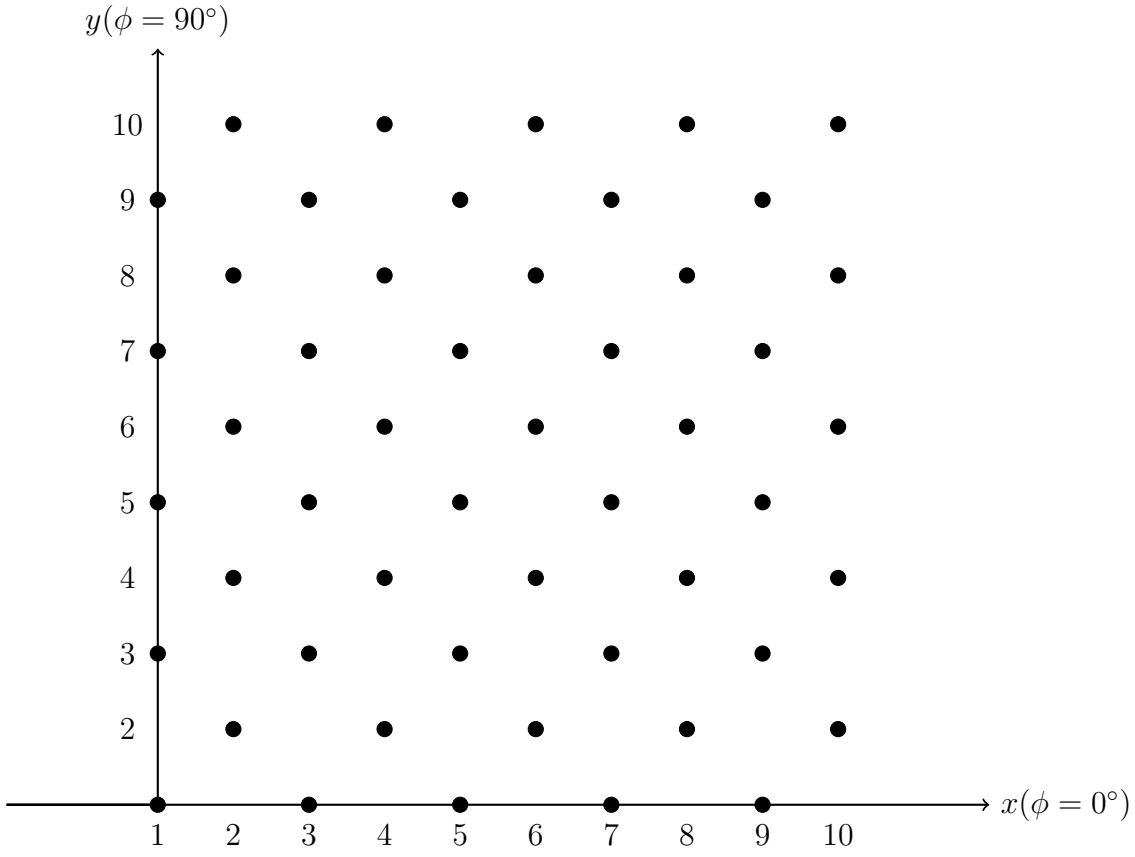

Figure 4.17: DDA-tile single polarisation antenna grid layout

quadratic function of θ_0. Further, it is seen that the significant quantization lobe has moved out of the visible region entirely when $\theta_0 = 20°$. This is significant because the EEP's are relatively flat between $-20° < \theta < 20°$, resulting in no significant effects on the relative level of quantization lobe.

For the density ratio value range of the current study (between 1.15 and 2.2), it is seen that the quantization lobe reappears when scanning beyond 20°, however at the same time it is seen that it will possible only reach significant space (defined as the angular extent of the EEP HPBW) for $R = 1.15$. For the other R values under consideration, the quantization lobe never re-enters the significant angular space.

Taking the scan range of the current study into account, and considering the above discussion on the angular behaviour of a significant quantization lobe, it can be explained why the SQNR increases between $R = 1.15$ and $R = 1.6$ in the $\phi = 90°$ (H)plane, while it is expected to remain either constant, or decrease due to beam broadening. At $R = 1.15$, the quantization lobe reaches significant space at the edge of the scan range, where at the same time the main lobe experiences attenuation, therefore resulting in a decreased SQNR. At $R = 1.6$, the quantization lobe never reaches significant space, so an increase

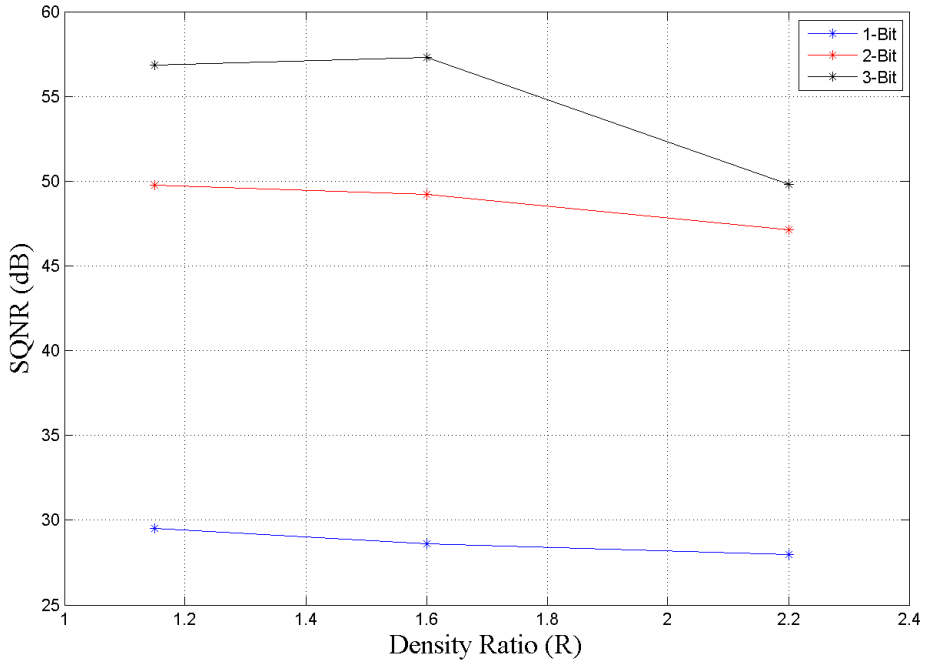

Figure 4.18: SQNR as a function of R and B, in the $\phi = 0°$ (E)plane

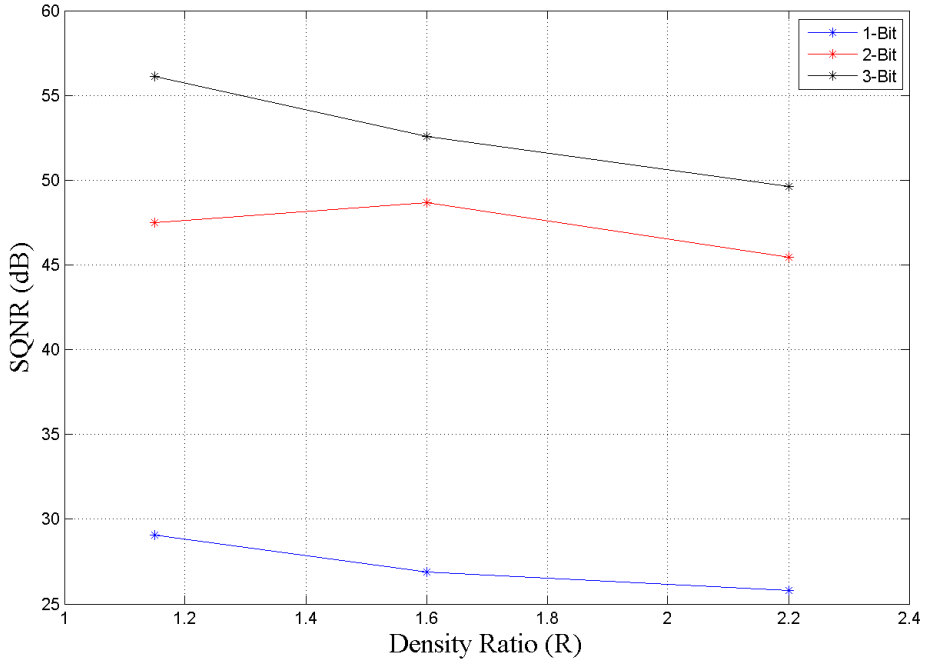

Figure 4.19: SQNR as a function of R and B, in the $\phi = 0°$ (H)plane

in SQNR is observed.

The same is not observed in the $\phi = 0°$ (E)plane. This is because the HPBW of the EEP in this plane and corresponding frequency limits the scan range more, which results in the quantization lobe never reaching significant space.

The 1-bit case has a significantly lower SQNR level compared to the 2- and 3-bit cases. This can once again be explained by the second symmetric main lobe which is a dominant source of pattern noise. With the EEP's being close to symmetrical around broadside, it is expected that it will be a dominant pattern noise source for the full scan range.

It should be mentioned that when considering the EEP's, it is seen that when scanning to broadside, the side lobes at the edges of the visible region is suppressed. However, being a desired effect, this contributes to pattern noise as well since the SQNR is calculated with the absolute error. It would make sense to be able to distinguish between positive and negative noise, however, after investigation, it was determined that the noise due to suppressed side lobes by the EEP have an insignificant contribution to the SQNR. A separate study would be required to characterise these situations, but this proved to be out of the scope of this project.

4.6.5 Discussion

The results obtained here cannot be directly compared to the results obtained in Section 3.3.2. This is because the simulation models are entirely different.

Since both models are based on average errors across their respective scan angle ranges, it can be concluded that the contribution of mutual coupling did not have a large impact on the SQNR performance as was initially expected. This can further be attributed to the relative flatness in the HPBW's of the EEP's.

4.7 Conclusion

This Chapter served as a demonstration of a full implementation of the methodology presented in this thesis, whereby the beamforming performance is evaluated using a free excitation model. This was done by using the pattern multiplication theorem which states that the total radiation pattern of an array can be calculated as the product of the array factor and the average active element pattern. The required active element pattern was acquired from a Dense Dipole Array (DDA) prototype tile.

The basic theory and design of the DDA were discussed along with a motivation for building a second DDA prototype. The construction process and certain lack of resources gave rise to implementation and measurement chal-

lenges that had to be overcome by making informed decisions based on previous research by Gilmore [20].

The measurements were presented and discussed. Further comparisons were made with simulations results to confirm the basic operation of the array.

The simulation model was chosen to be larger than the prototype tile. This was done because the beamwidth of an array with the same size as the prototype tile was too large and as a result, will provide very little scanning abilities. The size of the array used in the simulation was optimized to provide optimal scanning abilities while maintaining adequate angular resolution. It was also found that the EEP of a central element on the tile is a good approximation of an EEP in a larger array and can, therefore, be incorporated in a larger model.

Measurement of the EEP was limited to the E- and H-planes, however, these correspond to the two principal planes of the antenna which were decided to be sufficient for beamforming performance analyses. The EEP's were additionally measured at three frequency points. It was desired to have measurements at frequency points representing the lower, centre and upper-frequency points of the DDA operational frequency band, however, due to limitations in the measurement equipment, the lower frequency point was limited to 750 MHz. The final measured frequency points were 750 MHz, 1050 MHz and 1450 MHz.

The frequency points were converted to equivalent density ratio values so that the results can be compared, where applicable, to those obtained in Chapter 3.

The free excitation model results were analysed and discussed after which it was concluded that reasonable performance is observed when comparing, where applicable, with the forced excitation model results.

Chapter 5

Conclusion

5.1 Summary

During the execution of this project, an evaluation model by which the beamforming performance of an array can be determined was both developed and implemented. Furthermore, a focus was placed on low-phase resolution beamformers. The application field in focus of antenna arrays was set out to be dense arrays for the Mid-Frequency Aperture Array.

A case study was performed in Section 2.7 to motivate the reason for reducing beamforming hardware complexity. This was done by investigating the application of beamforming hardware in the Mid-Frequency Aperture (MFAA) of the Square Kilometre Array (SKA) and cost-savings that can be achieved in general, by reducing the phase resolution of the beamforming hardware.

It was explained in Section 2.3 that it is currently not clear whether dense or sparse arrays will be used in the MFAA. A discussion on the advantages and design challenges of each were provided to highlight why it is not a trivial decision to make. However, dense arrays were set out to be the configuration in focus for this thesis.

The underlying beamforming theory on which the models are based is provided and discussed in Chapter 2. A literature study was additionally performed on the practical implementation of beamforming in hardware and software, which are more commonly known as analogue and digital beamforming.

Two performance metrics were identified to evaluate the beamforming performance of a beamformer. These were the pointing accuracy of the main lobe, and the side lobe level. Multiple effects of phase quantization were observed in the side lobes and had to be studied accordingly. To effectively determine these effects as a function of frequency, the k and d terms in the array factor were combined and related to a density ratio which describes the inter-element spacing in electrical length. The phase resolution, representing the complexity of the beamformer was characterised in bits.

The total beamforming performance of an array is the product of the array

factor based beamforming performance and the active element pattern which accounts for mutual coupling. It was, therefore, important to demonstrate an implementation of the evaluation model that was developed in Chapter 3. This was done in Chapter 4 by using the embedded element pattern of a Dense Dipole Array tile prototype. Informed assumptions were made based on measured S-parameter data, to extend the size of the simulation model beyond the physical size of the DDA.

Limitations in the measurement equipment allowed the active element patterns to be measured only in the E- and H-planes. The planar simulations were subsequently limited to the principle-planes. Insight obtained from the studies in Chapter 3 was used to explain the results obtained in Chapter 4. This went on to show that it is worthwhile to investigate the beamforming performance of an array purely as a function of its configuration to understand the combined effects of mutual coupling.

In conclusion, this thesis provided a useful methodology by which the phase quantization effects in beamforming hardware can be investigated to determine the feasibility of using low phase resolution beamformers in an application with specific requirements. These models were based on small arrays compared to practical phased antenna arrays for radio astronomy such as EMBRACE or MFAA. However, these simulations can easily be extended to larger arrays. Therefore, in summary, this thesis served only as a demonstration of the methodology with which the beamforming performance of an array can be determined.

5.2 Contributions

Based on the work done in Chapters 2,3 and 4, the following contributions were made during the execution of this project:

1. The scan-limitations of a simple beamformer were established.
2. The scan range limits so as to ensure the full half-power main lobe is defined was investigated as a function of a set of array parameters.
3. The effects of phase quantization on the scan accuracy of a certain set of array parameters were investigated.
4. Relative amplitude loss in the main lobe due to heightened side lobe levels were investigated.
5. Beam pattern noise as a result of phase quantization was identified to consist of two components each showing separate behaviour as a function of the array parameters.
6. The amplitude extents and angular behaviour of a quantization lobe as a function of a certain set of array parameters were determined.

7. Overall pattern noise performance as a function of a certain set of array parameters was investigated.
8. Total array beamforming performance was investigated by adding mutual coupling to all the performance models.
9. A second DDA prototype tile was built.
10. Larger sample of S-parameters was measured than the first prototype by connecting more elements.
11. Determined that counter-intuitive edge effects are observed in the active reflection coefficients of edge elements.
12. Showed that a centre active element pattern might be representative of the average radiation pattern of the DDA tile and larger array.
13. DDA PCB layout was changed to ease mass manufacturing.
14. Castellation joints were investigated as a way of strengthening the dipole discontinuity joints.

5.3 Recommendations for Future Work

5.3.1 DDA Construction, Measurement and use in Practical Analyses

For the practical implementation in Chapter 4, a DDA prototype was built and measured. Only half of one polarisation was connected due to limited resources. Due to confirmed symmetry, it was possible to fill the rest of the S-parameter matrix.

Simulated S-parameters were obtained by simulating the DDA in FEKO using a finite array simulation. The measured and simulated S-parameters were used to calculate active reflection coefficients after which the bandwidth could be confirmed. The curves, however, did not match very well. This could be because of inaccuracies in the simulation, but it could also be due to lack of a full representative set of S-parameter measurements. In an attempt to explain the discrepancies in the simulated and measured S-parameters it is recommended that a fully connected tile in both polarisations are built and measured.

It is further speculated that radiation from the feed boards of the connected elements can couple with the dipoles and cause some of the discrepancies observed in the S-parameters. This can be confirmed by performing separate gain pattern simulations of the feed boards.

A simulation model larger than the actual DDA prototype tile was implemented. By referring to the relevant coupling in the array, it was explained

that the central active element pattern might be representative of the average array pattern of the tile and also a larger array. It is recommended that this assumption is confirmed by performing a finite array simulation of this size.

5.3.2 Random Phase Offset to reduce Quantization Lobes

As was discussed in Section 3.3, according to [33] it should be possible to lower quantization lobes by using a fixed random phase offset at each element prior to quantization. This will effectively eliminate the periodicity in the phase errors and as a result, reduce the amplitude of quantization lobes.

It is expected that this will negatively contribute to the scan accuracy. However, it could be worthwhile to investigate this type of implementation and the optimization viability of the random phase offset at each element to find an optimal trade-off point between the scan accuracy and quantization lobe amplitude level.

5.3.3 Amplitude Tapering

A general discussion of amplitude tapering was provided in Section 2.5. A spectral weighting technique was discussed where it was shown that the SLL can be reduced using sinusoidal weights, however, at the expense of an increasing beamwidth. This implementation can possibly be used to reduce secondary and primary noise as was investigated in Sections 3.3.3, 3.4.2 and 4.6.4 for a linear and planar array. An increase in beamwidth was shown to generally reduce beamforming performance so an optimal trade-off point might have to be determined.

Not discussed in Section 2.5 is the Dolph-Chebychev weighting technique which aims to optimise the beamwidth to SLL trade-off.

5.3.4 Zero-Error Scan Angles

It was generally assumed that the existence of phase errors are consistent for any scan angle. It is, however, possible that certain scan angles exist where zero phase error is observed. If multiple of these angles exist, it might be possible to identify them as a set. This set can then be pre-programmed in the beamformer and be used when perfect scan accuracies are required during observations.

Bibliography

[1] Benthem, P. and Kant, G.W.: EMBRACE: Results from an aperture array for radio astronomy. In: *2012 6th European Conference on Antennas and Propagation (EUCAP)*, pp. 629–633. IEEE, mar 2012. ISBN 978-1-4577-0920-3.
Available at: http://ieeexplore.ieee.org/document/6206634/

[2] Visser, K., Wal, E.V.D., Ruiter, M. and Kant, D.: A 400 MHz - 1600 MHz SiGe MMIC beam-former for the square kilometre array. In: *2008 European Microwave Integrated Circuit Conference, EuMIC 2008*, October, pp. 494–497. IEEE, oct 2008. ISBN 9782874870071.
Available at: http://ieeexplore.ieee.org/document/4772337/

[3] Gunst, A.A.W., Faulkner, A., Wijnholds, S., Jongerius, R., Torchinsky, S., Cappellen, W.V. and Gunst, A.: MID FREQUENCY APERTURE ARRAY ARCHITECTURAL DESIGN DOCUMENT. 2016.

[4] Jansky, K.: Electrical Disturbances Apparently of Extraterrestrial Origin. *Proceedings of the IRE*, vol. 21, no. 10, pp. 1387–1398, oct 1933. ISSN 0096-8390.
Available at: http://ieeexplore.ieee.org/document/1685232/

[5] Zakharenko, V., Yerin, S., Bubnov, I., Vasilieva, I. and Kravtsov, I.: Using of pulsar spectra catalogue at frequencies below 80 MHz for astronomical calibration of phased antenna arrays. In: *2016 II International Young Scientists Forum on Applied Physics and Engineering (YSF)*, pp. 210–213. IEEE, oct 2016. ISBN 978-1-4673-8841-2.
Available at: http://ieeexplore.ieee.org/document/7753839/

[6] Liu, J., Ma, J., Tian, J., Kang, Z. and White, P.: Pulsar navigation for interplanetary missions using CV model and ASUKF. *Aerospace Science and Technology*, vol. 22, no. 1, pp. 19–23, oct 2012. ISSN 12709638.
Available at: http://dx.doi.org/10.1016/j.ast.2011.04.010 http://linkinghub.elsevier.com/retrieve/pii/S1270963811000836

[7] van Moorsel, G.: The Very Large Array after the upgrade. In: *2014 XXXIth URSI General Assembly and Scientific Symposium (URSI GASS)*, pp. 1–3. IEEE, aug 2014. ISBN 978-1-4673-5225-3.
Available at: http://ieeexplore.ieee.org/document/6929995/

[8] Hills, R.E. and Beasley, A.J.: The Atacama Large Millimeter/submillimeter Array. 1, p. 70120N. aug 2008. ISBN 1424414385. arXiv:0904.3739v1.
Available at: http://proceedings.spiedigitallibrary.org/proceeding

[9] A.R. Thompson, J. M. Moran, G.W. Swenson Jr: *Interferometry and Synthesis in Radio Astronomy*. Second edi edn. John Wiley & Sons, Inc., 2004.

[10] Vermeulen, R.C. and van Haarlem, M.: The international LOFAR telescope (ILT). In: *2011 XXXth URSI General Assembly and Scientific Symposium*, pp. 1–1. IEEE, aug 2011. ISBN 978-1-4244-5117-3.
Available at: `http://ieeexplore.ieee.org/document/6051244/`

[11] Schaubert, D., van Ardenne, A., Cracye, C., Boryssonko, A. and Bij de Vaate, J.: The square kilometer array (ska) antenna. In: *IEEE International Symposium on Phased Array Systems and Technology, 2003.*, vol. 2003-Janua, pp. 351–358. IEEE, 2003. ISBN 0-7803-7827-X.
Available at: `http://ieeexplore.ieee.org/document/1257007/`

[12] Rawlings, S. and Schilizzi, R.: The Square Kilometre Array. , no. 291, pp. 1–26, may 2011. ISSN 11752025. `1105.5953`.
Available at: `http://arxiv.org/abs/1105.5953`

[13] Ardenne, B.A.V., Bregman, J.D., Cappellen, W.A.V., Kant, G.W., Geralt, J. and Vaate, B.D.: Extending the Field of View With Phased Array Techniques : Results of European. pp. 0–11, 2009.

[14] Davidson, D.B.: The SKA and the MeerKAT precursor; Extreme antenna engineering. In: *The 8th European Conference on Antennas and Propagation (EuCAP 2014)*, EuCAP, pp. 1216–1219. IEEE, apr 2014. ISBN 978-8-8907-0184-9.
Available at: `http://ieeexplore.ieee.org/document/6901994/`

[15] Chippendale, A. and Schinckel, A.: ASKAP: Progress towards 36 parabolic reflectors with phased array feeds. In: *2011 XXXth URSI General Assembly and Scientific Symposium*, October 2010, pp. 1–4. IEEE, aug 2011. ISBN 978-1-4244-5117-3.
Available at: `http://ieeexplore.ieee.org/document/6123713/`

[16] Bij de Vaate, J.G., Torchinsky, S.A., Faulkner, A.J., Zhang, Y., Gunst, A., Benthem, P., van Bemmel, I.M. and Kenfack, G.: SKA Mid Frequency Aperture arrays: Technology for the ultimate survey machine. In: *2014 XXXIth URSI General Assembly and Scientific Symposium (URSI GASS)*, pp. 1–4. IEEE, aug 2014. ISBN 978-1-4673-5225-3.
Available at: `http://ieeexplore.ieee.org/document/6929991/`

[17] Braun, R. and van Cappellen, W.: Aperture Arrays for the SKA: Dense or Sparse? p. 15, nov 2006. `0611160`.
Available at: `http://arxiv.org/abs/astro-ph/0611160`

[18] Array, S.K., Commission, T.E., Framework, S., Studies, S.K.A.D., Skads, A. and Ska, E.: Embrace Design and Development. *2008 IEEE Antennas and Propagation Society International Symposium*, pp. 2–5, jul 2008.
Available at: `http://ieeexplore.ieee.org/document/4619303/`

[19] Zhang, Y. and Brown, A.K.: Octagonal Ring Antenna for a Compact Dual-Polarized Aperture Array. *IEEE Transactions on Antennas and Propagation*, vol. 59, no. 10, pp. 3927–3932, oct 2011. ISSN 0018-926X.
Available at: `http://ieeexplore.ieee.org/document/5976417/`

[20] Gilmore, J.: *Design of a Dual-Polarized Dense Dipole Array for the SKA Mid-Frequency Aperture Array*. Ph.D. thesis, 2016.

[21] van Cappellen, W.: Preliminary MFAA Cost and Power Estimate. Tech. Rep., 2016.

[22] Stutzman, W.L. and Thiele, G.A.: *Antenna Theory and Design*. 2nd edn. John Wiley & Sons, Inc.

[23] Bird, T.S.: *Fundamentals of Aperture Antennas and Arrays*. 1st edn. John Wiley & Sons, Inc., 2016.

[24] Kildal, P.-s.: *Foundations of Antenna Engineering : A Unified Approach for Line-of-Sight and Multipath*. 2015. ISBN 9789163785153.

[25] de Vaate, J.G.B., Davidson, D. and Benthem, P.: Expanding the field of view: Design considerations for a sparse-regular FFT SKA radio telescope. In: *2017 11th European Conference on Antennas and Propagation (EUCAP)*, pp. 3829–3831. IEEE, mar 2017. ISBN 978-8-8907-0187-0.
Available at: `http://ieeexplore.ieee.org/document/7928226/`

[26] Balanis, C.: *Antenna Theory and Design*, vol. 28. 1982. ISBN 1118585739.

[27] Munk, B.A.: *Frequency Selective Surfaces*. John Wiley & Sons, Inc., Hoboken, NJ, USA, apr 2000. ISBN 9780471723776.
Available at: `http://doi.wiley.com/10.1002/0471723770`

[28] Krieger, J.D., Yeang, C.-p. and Wornell, G.W.: Dense Delta-Sigma Phased Arrays. *IEEE Transactions on Antennas and Propagation*, vol. 61, no. 4, pp. 1825–1837, apr 2013. ISSN 0018-926X.
Available at: `http://ieeexplore.ieee.org/document/6416005/`

[29] Faulkner, A.: Mid-Frequency Aperture Array Technology Description. Tech. Rep., 2016.

[30] Gilmore, J., Wilke, C.R. and Davidson, D.B.: Calculating the Maximum Quantization Scan Error in Dense Phased Arrays. In: *Antennas and Propagation (EUCAP), 2017 11th European Conference on*, 10, pp. 1–3. IEEE, mar 2017. ISBN 9788890701870.
Available at: `http://ieeexplore.ieee.org/document/7928566/`

[31] Wilke, C.R., Gilmore, J. and Davidson, D.B.: Reducing the maximum quantization scan error in dense phased arrays. In: *2017 International Conference on Electromagnetics in Advanced Applications (ICEAA)*, pp. 1268–1271. IEEE, sep 2017. ISBN 978-1-5090-4451-1.
Available at: `http://ieeexplore.ieee.org/document/8065503/`

[32] Vigano, M.C., del Rio, D.L., Bongard, F., Padilla, J. and Vaccaro, S.: One-bit phased array with wide scan and linear polarization control for mobile satellite applications. In: *2012 6th European Conference on Antennas and Propagation (EUCAP)*, vol. 945, pp. 1641–1644. IEEE, mar 2012. ISBN 978-1-4577-0920-3. Available at: `http://ieeexplore.ieee.org/document/6206346/`

[33] Cheston, T.C. and Frank, J.: Array Antennas. 1968.

[34] Noordam, J. and Voute, J.: Design Aspects of a Tile Telescope: A possible approach to a Square Kilometre Array Interferometer (SKAI). Tech. Rep., ASTRON, Dwingeloo, Netherlands, 1994.

[35] Wheeler, H.: Simple relations derived fom a phased-array antenna made of an infinite current sheet. *IEEE Transactions on Antennas and Propagation*, vol. 13, no. 4, pp. 506–514, jul 1965. ISSN 0096-1973.
Available at: `http://ieeexplore.ieee.org/document/1138456/`

[36] Arts, M., Maaskant, R., Acedo, E.D.L., Geralt, J. and Vaate, D.: Broadband Differentially Fed Tapered Slot Antenna Array for Radio Astronomy Applications. pp. 566–570.

[37] Meyer, P. and Prinsloo, D.S.: Generalized Multimode Scattering Parameter and Antenna Far-Field Conversions. *IEEE Transactions on Antennas and Propagation*, vol. 63, no. 11, pp. 4818–4826, nov 2015. ISSN 0018-926X.
Available at: `http://ieeexplore.ieee.org/document/7234872/`